THE ROLE OF SURFACE RECOMBINATION IN SINGLE EVENT PHENOMENA

By

Andrew Michael Tonigan

Dissertation

Submitted to the Faculty of the

Graduate School of Vanderbilt University

in partial fulfillment of the requirements

for the degree of

DOCTOR OF PHILOSOPHY

in

Interdisciplinary Materials Science

September 30th, 2020

Nashville, Tennessee

Approved:

Ronald D. Schrimpf, Ph.D.

Michael L. Alles, Ph.D.

Sokrates T. Pantelides, Ph.D.

Robert A. Reed, Ph.D.

D. Greg Walker, Ph.D.

© Copyright by Andrew Tonigan 2020

All Rights Reserved

DEDICATION

To my parents - who sparked my imagination and

encouraged my exploration in science, and all things.

ACKNOWLEDGEMENTS

I am thankful for the many individuals who contributed to the completion of this dissertation. Dr. Schrimpf has been an outstanding advisor and mentor, providing solid guidance and scientific wisdom throughout my graduate studies. Dr. Reed has offered consistent support, a touch of humor, and many productive discussions. Dr. Alles has helped ground my research efforts with practical considerations and his expertise has been valuable. It has been a delight to explore physics research alongside Dr. Pantelides, who brings a well-refined, inquisitive mind to every discussion. Dr. Walker has provided me with wonderful opportunities during my time at Vanderbilt and I appreciate his open door and sharp engineering instincts.

Many other professors and colleagues have been important to my development as a scholar and scientist. Dr. Fleetwood has provided spot-on scientific insight and guidance on numerous occasions. Dr. Zhang and Mike McCurdy are essential to the experimental work we perform and my projects have greatly benefitted from their kind and knowledgeable support. Dr. Ball and Dr. Sternberg have been helpful on many occasions and I've consistently enjoyed approaching and solving problems with their assistance. Dr. Weller has provided a keen insight into radiation-matter interactions that has helped develop my understanding; along with Dr. Warren and Dr. Sierawski who's pragmatic perspective helps gear research toward real-world contributions.

My fellow graduate students have made my time at Vanderbilt memorable. Kaitlyn and Landen Ryder have been great friends and helpful collaborators. Brandon Smith and Rachel Brewer have been a joy to work alongside. Discussions with Matthew Breeding have been invaluable, and quite enjoyable. I appreciate the engineering mindset, and humor, of Daniel Vibbert who has enriched a variety of discussions. The sharp minds and good work ethic of Maria Gorchichko, Mahmud Reaz, Casey Brock, Jake Benzing, Liuda Prozorovska, Matthew Gerboth,

and Kan Li have made spending time and working with them a pleasure; I've greatly appreciated my friends and colleagues at Vanderbilt.

I am grateful for the funding support from Sandia National Laboratories LDRD program and ASTM International's Graduate Fellowship. Dolores Black, Jeff Black, and James Trippe have provided me with great opportunities to pursue interesting research and I have enjoyed working with them very much. Gyorge Vizkelethy and Ed Bielejec provided instrumental support for completing the experimental portions of this dissertation; I am grateful to have benefited from their skill and expertise.

Finally, I would like to personally thank my fiancé Liz Natal, Esq. for her unequaled support, and careful review of this dissertation. My sister Jackie Faught and uncle Scott Tonigan have always supported me and their examples of good character continually motivate me to better myself – thank you.

TABLE OF CONTENTS

Page

DEDICATION iii

ACKNOWLEDGEMENTS iv

TABLE OF FIGURES viii

ACRONYMS xv

Chapter

INTRODUCTION 1

I.1 Dissertation organization 2

BACKGROUND 4

II.1 Radiation environments 5

II.2 Mechanisms of radiation energy deposition 18

II.2.1 Photon energy deposition 18

II.2.2 Particle energy deposition 19

II.3 Mechanisms of single-event charge collection 28

II.3.1 Thermalized carrier assumption 28

II.3.2 Junction charge collection 32

II.4 Total ionizing dose mechanisms 36

II.4.1 TID conditions for increasing surface recombination 38

II.5 Recombination physics 42

II.5.1 Surface recombination velocity measurements 47

RADIATION EFFECTS IN SOI 49

III.1 Leakage paths 50

III.2 Generation leakage current 51

III.3 Floating body effects **52**

III.4 Capacitive influence **54**

III.5 Radiation-hardened SOI **56**

III.5.1 BUSFET features 56

III.5.2 BUSFET optimization 58

MODELING SINGLE-EVENTS AND SURFACE RECOMBINATION 61

IV.1 Generation leakage current in SNL SOI **62**

IV.2 Single-events in SNL SOI **64**

IV.3 Impact of surface recombination on charge collection **68**

MICROBEAM ANALYSIS OF SURFACE RECOMBINATION 75

V.1 Enhanced surface recombination velocity **80**

V.2 Impact of surface recombination on charge collection measurements **83**

THE SURFACE RECOMBINATION EFFECT 86

VI.1 Technology trends **89**

CONCLUSIONS 93

REFERENCES 94

LIST OF FIGURES

Figure Page

1. Timeline of developments in physics, electronics and radiation effects.................................4

2. High energy galactic cosmic ray energy spectrum for a variety of elements [3] (left). On the right is the low energy spectrum for several light elements, only recently attainable by the Voyager spacecraft [4]. 5

3. Parker Solar Probe measurements of the Solar Energetic Particle environment [7]. 6

4. Top: GEO particle flux spectra generated by CRÈME 2009 are shown for different solar conditions, solar maximum and solar minimum. Bottom: Worst day condition with and without 100 mils of aluminum shielding. 7

5. Top: Cosmic ray shower is depicted. Bottom: Terrestrial flux spectrum of muon, neutrons and protons at sea level..8

6. Primary particle composition of the Van Allen Belts. The AP-8 omnidirection flux of protons with an energy above 10 MeV (top) and AE-8 omnidirection flux of electrons above 1 MeV (bottom)...9

7. Solar flare captured by the Solar and Heliospheric Observatory, SOHO (left). SEPs impinge upon SOHO's focal plane array, producing radiation effects in many of CCD pixels (right). 10

8. A single ionizing particle passes by a N^+P junction creating electron-hole pairs that are collected by drift and diffusion. The collected charge profile shows a peak from drift collection and then sustained collection from diffusion [28]. 13

9. LET spectrum within 100 mils of aluminum shielding in GEO during a period of minimum solar activity (flux spectra representing 28 elements shown inset). 16

10. Increasing sensitivity of electronics to energy deposited during a single event with continual Moore's Law scaling [37]. 17

11. Energy and target material dependence of photon interactions. At low photon energies, the photoelectric effect is dominant. 19

12. Particle-matter interactions. The top panels illustrate three types of particle interactions that result in energy deposition. Example track structures produced by a Monte Carlo radiation transport tool, MRED, are shown in the bottom panels. 20

13. LET vs. particle energy for different ions. 23

14. Energy deposition distribution in sensitive volumes of different thickness. Statistical variability in energy deposition, straggle, is more evident across small volumes. 24

15. LET as a function depth as a 35-MeV oxygen ion penetrates into silicon. On the right axis is the LET converted to charge generated per μm. The shaded region illustrates the variation in LET that can occur across a 250 nm volume (e.g., ion straggle) 25

16. The average energy, and range, of secondary electrons is proportional to the incident ion energy. Despite having the same LET, 5 GeV iron has a considerably larger track radius then 5 MeV carbon. 26

17. Energy deposition events in a central 1 μm^3 sensitive volume plotted as function of the incident ion x and y location. If the device is sensitive to low energy deposition events, the secondary electrons produced by ion strikes outside of the sensitive volume can result in an SEE occurring. Events that do not deposit energy in the sensitive volume are plotted as light gray dots. 27

18. Physical regimes traversed during carrier relaxation. 28

19. Electron and hole thermalization after ion strike. In the top figures a dense column of energetic electron-hole pairs crosses an n^+p junction. The average energy of carriers in the device returns to equilibrium after 2 ps (middle). In k-space, the initial high energy carriers (0 ps) occupy positions in the band structure far from the conduction and valence band minima until they are thermalized (2 ps). 30

20. Thermalized radius assumption. A Gaussian distribution of electron-hole pairs with a radial standard deviation of 50 nm adequately captures track structure and carrier relaxation effects for modeling subsequent drift and diffusion processes. On the right, an example Gaussian temporal and spatial charge distribution is shown as commonly implemented in finite-element modeling of SEE. 31

21. Single-event charge collection in an n^+p junction. The electron and hole carrier concentrations are illustrated extending outward from the conduction and valence band, respectively. The rate of recombination as function of position is plotted below. During the ion strike, the energy band resembles that of a conductive wire with an electric field reaching into the both end regions. 33

22. Potential distribution during strike of hard-biased diode (top) and a diode coupled into a circuit (bottom). The voltage at the n^+ contact drops in the circuit-coupled diode during the transient. 34

23. Single-event transient in CMOS inverter. Top: Illustration of with the off-state nmos and on-state pmos. Bottom: Single-event charge collection can temporarily make the off-state nmos conductive and connects Vss (ground) to the inverter output. 35

24. Top: Energy band illustration of total ionizing dose effects [59]. Bottom: Formation dynamics of interface traps [61]. Positively charged proton transport to the semiconductor/insulator interface is crucial in the formation of interface traps. 37

25. MOS energy band diagram in accumulation (top) and inversion (bottom). The occupation, and charge state, of trap levels depend on the local electrostatic potential. 38

26. The effect of electric field on recombining electron-hole pairs in SiO_2 from various ionizing radiation sources. At higher electric field strength, carriers separate more rapidly and will recombine less [58]. 39

27. The effect of dose rate on interface trap formation. At dose rates less than 10 rad(SiO_2)/s interface trap density is maximized [68]. 40

28. Key carrier recombination processes for SEE. 43

29. Relative surface recombination velocity as a function of interface state energy for different hole/electron capture ratios. The most effective recombination level can shift toward the conduction band or valence band depending on whether the electron or hole capture cross-section is greater. 46

30. Small and large signal AC conductance techniques for investigating interface defects [82]. In small signal measurements, individual defects can be probed; while in large signal measurements the effect of all defects is assessed simultaneously. The large signal technique is useful for measuring the total SRV. 48

31. Partially- and fully-depleted SOI technologies. The perimeter of the electrically sensitive semiconductor region is a buried oxide layer (below) and shallow trench isolation (on the sides). Red signifies n-type doping, while blue is p-type..49

32. TID-induced leakage paths in SOI technology...50

33. Trapped charge in the BOX creates a back channel for electrons between source and drain. Off-state leakage current in an SOI device increases with trapped charge density. 51

34. Off-state generation leakage current in an SOI device. Interface generation current is produced along the buried oxide surface under the drain-body junction. 52

35. Parasitic bipolar enhancement in SOI. Holes introduced in the body region forward-bias the source-body (emitter-base) junction turning on the bipolar element. The electrostatic potential (left) and hole concentration (right) are shown going from source to drain for different conditions: equilibrium, during ion strike, and 85 ps after the strike. The inset illustrates the corresponding drain transient. 53

36. Capacitor charge collection via displacement current (induced charge) during ion strikes [97]. The induced charge is a function of depletion region size (e.g., doping and applied bias). ...54

37. Charge induced as a function of strike location across a capacitor during microbeam testing [98]. The amount of charge increases with reverse bias/depletion region width (top). Effective passivation near the edges results in a larger depletion region and higher charge collection. Further annealing is used to increase passivation and charge collection across device..........55

38. BUSFET device structure with shallow source and body contact. 56

39. Left: Back-channel leakage in SOI with a shallow or deep source. Right: Leakage in Sandia's BUSFET design [99]. 57

40. Charge collection from a single event in a normal SOI MOSFET compared to the BUSFET structure. The BUSFET experiences significantly less parasitic bipolar enhancement. 58

41. Top: Experimental SEE cross-section measurements on Sandia's CMOS7 performed at the Texas A&M cyclotron. The extended body and shallow drain device design offers improved SEE tolerance. Bottom: Model predictions for error cross-section from direct ionization from high LET ions. 59

42. Generation leakage current along buried oxide interface in Sandia SOI. 62

43. Generation leakage current with different drain voltages. SRV of 10^6 cm/s 63

44. Single-event ion strike in SNL SOI device channel. 64

45. Single-event transient current (top) and collected charge (bottom) in source, drain, and body contacts for a strike location in the channel. 65

46. Peak drain current as a function of ion strike location for an LET of 7 MeV-cm^2 per mg with +3.0 V applied to the drain. Peak current is greatest when the ion strikes the drain side of the channel. 66

47. Single-event charge collection in source, drain, and body contacts as a function of ion strike location for an ion with LET = 7 MeV-cm^2 per mg with +3.0 V applied to the drain. 67

48. Finite-element modeling of interface effects. On the top, a simulated ion strike generates excess carriers (electron concentration visualized). On the top, a bottom view show the rate of surface recombination occurring along the STI and BOX. 68

49. Impact of surface recombination on drain charge collection for a high LET ion strike in the channel. As SRV increases (corresponding to a more defect-laden interface) the charge collected during a single event in this SOI technology decreases. 69

50. Impact of surface recombination on drain charge collection for a moderate LET ion strike in the channel. 70

51. Integral charge recombined along oxide surfaces as a function of time. The amount of charge lost to surface recombination increases with ion LET. 70

52. Integral charge recombined along oxide surfaces as a function of time and recombination mechanism. 71

53. Spatial charge collection distributions from finite-element simulations with no surface recombination and a high SRV. 72

54. Spatial distribution of charge lost to surface recombination along all isolation interfaces (top) and just along the STI (bottom). 73

55. Spatial distribution of charge lost to surface recombination along all isolation interfaces for an ion LET of 50 MeV-cm^2 per mg. 74

56. Microbeam test setup. DUT is mounted in endstation (left), chip is wire bonded in package (right). 75

57. LET as a function of depth for microbeam ion, 35-MeV oxygen. The beam penetrates through 10 μm of overlayer material before reaching the active device. The Z of the overlayer material is similar to that of silicon. 76

58. Comparison of experimental drain current transient with modeled transient for a strike location in the channel. 77

59. Charge collection in drain and body contacts. 78

60. Ion beam induced charge collection map of PDSOI device. On the top, charge collection is measured at the drain with a +3 V bias. In the bottom, charge collection is measured in body with a –3 V bias. 79

61. Gamma-irradiation experimental setup at the SNL GIF. 80

62. Experimental high-speed device packaging with substrate contact. An electric field is created across the isolation oxide during irradiation with an applied substrate bias. 81

63. Top: Transfer characteristics pre- and post TID. Increased OFF-state leakage current occurs following TID and corresponds to interface generation from isolation interfaces observed in modeling results. Bottom: Linear I(V) and gate current do not exhibit prominent TID effects or back-channel conduction. 82

64. Spatial charge collection distributions for IBICC measurements with the drain biased to +3.0V before and after gamma-irradiation. 83

65. TRIBICC charge collection distribution for PDSOI device pre- and post-TID. (Inset) The mean of the charge collection distribution exhibits an abrupt drop after TID but is stable with accumulated ion fluence. 84

66. The mean charge collection vs. time before and after irradiation. 85

67. Measured vs. simulated charge collection as a function of surface recombination. 86

68. Spatial charge collection distributions for a.) IBICC measurements before and after gamma-irradiation b.) finite-element simulations with low surface recombination, corresponding to pre-rad, and high surface recombination (10^6 cm/s) corresponding to post-rad interface conditions. 87

69. Surface recombination velocities measured for Si/SiO_2 interfaces and bare silicon surfaces. 88

70. The impact of surface recombination on drain transients and charge collection for a 10 MeV-cm^2 per mg channel strike in a 90 nm PDSOI device. 89

71. The impact of surface recombination on drain transients and charge collection for a 10 MeV-cm^2 per mg channel strike in a 45 nm FDSOI device. 90

72. The impact of surface recombination on inverter output voltage transients with technology scaling. 92

ACRONYMS

BCA	Binary collision approximation
BOX	Buried oxide
CMOS	Complementary metal-oxide-semiconductor
CRÉME	Cosmic Ray Effects on MicroElectronics
DUT	Device-under-test
FEM	Finite-element method
FDSOI	Fully-depleted silicon-on-insulator
GCR	Galactic cosmic ray
GEO	Geostationary Orbit
GIF	Gamma Irradiation Facility
IBICC	Ion beam-induced charge collection
IBL	Ion Beam Lab
LET	Linear energy transfer
LEO	Low Earth orbit
MRED	Monte Carlo Radiative Energy Deposition
PBE	Parasitic bipolar enhancement
PDSOI	Partially-depleted silicon-on-insulator
SEE	Single event effect
SEP	Solar energetic particle
SET	Single event transient
SEU	Single event upset
SNL	Sandia National Laboratory

SOI	Silicon-on-insulator
SRAM	Static random access memory
SRH	Shockley-Read-Hall
SRV	Surface recombination velocity
STI	Shallow trench isolation
TCAD	Technology Computer-Aided Design
TRIBICC	Time-resolved ion beam-induced charge collection
TID	Total ionizing dose
UTBB	Ultra-thin body and box

CHAPTER I

INTRODUCTION

The use of electronic systems greatly enhances our collective ability to understand and explore. Electronic systems do so by storing and processing complex information with greater precision and speed than is otherwise possible. Therefore, we place an ever-increasing amount of responsibility in electronics to handle our information without error. A particularly harsh environment, where the use of electronic systems is indispensable, is one that contains significant amounts of ionizing radiation. Such environments are encountered in interplanetary space, satellite orbits, avionics, medical treatments, high energy physics research and military conflict. Temporary and/or permanent radiation-induced changes to material and interface properties can degrade the performance of electronic systems and bring into question their reliability. Design choices and fabrication techniques can have a serious impact on radiation-reliability and physics-based modeling is needed to optimize reliability and performance before pursuing expensive manufacturing and testing. Once reliability testing commences, mechanistic models are needed to develop a complete, and actionable, understanding of the observed failure modes.

The radiation-reliability concern this dissertation is focused on is soft errors. Soft errors are temporary memory state changes produced in digital circuits by individual particle radiation during single-events. The development of radiation-reliability models that describe single event effects (SEE) requires accurately identifying and capturing relevant physical mechanisms [1]. In modern and emerging nanoscale technologies (especially silicon-on-insulator (SOI) technology and 3D architectures), an immense density of insulating interfaces serves to complicate physical mechanisms; meanwhile dense integration concurrently drives the use of devices that are especially sensitive to SEE. This dissertation demonstrates modeling methods, confirmed with

experimental measurements, for assessing the role of a particular physical mechanism, surface recombination, in the phenomena of SEE. Surface recombination plays an active role in the behavior of electronics whenever non-equilibrium conditions occur along a semiconductor/insulator interface. During a single-event, ionizing particle radiation passes through sensitive electronic volumes generating excess charge carriers that introduce non-equilibrium conditions. In modern devices, these sensitive volumes are surrounded by isolation oxides that the excess carriers interact with during single-events. This dissertation contains the first experimental evidence that surface recombination along isolation interfaces can play a significant role in the single-event response of an SOI technology. The results of this work are compared with other surface recombination measurements and provide an extension to our understanding of surface recombination along the Si/SiO_2 interface. Furthermore, the analysis is extended across several scaled technologies, illustrating the continued importance for understanding this effect. If isolation interfaces have a surface recombination velocity (SRV) of 10^3 cm/s or greater within 1 μm of a sensitive volume this mechanism should be considered in physics-based modeling. For values greater than 10^5 cm/s, accurate modeling of single event phenomenon cannot neglect surface recombination without significantly over-predicting charge collection from single-events.

I.1 Dissertation organization

Radiation effects on electronics is an interdisciplinary field of research that has its roots in 20th century breakthroughs in electronics and physics. Chapter II summarizes the important historical developments that motivate the study of radiation effects on electronics and introduces critical physical mechanisms. Special attention is given to charge generation and collection

processes to acquaint the reader with relevant single event phenomena and substantiate modeling assumptions before covering the physics of surface recombination. Chapter III provides description of radiation effects particular to SOI technologies. Chapter IV presents simulation results for charge collection that incorporate surface recombination in Sandia National Laboratories (SNL) SOI technology. The validated model is used to demonstrate how single-event charge collection is impacted by surface recombination. Chapter V presents an experimental microbeam analysis of single-event charge collection in the SNL technology. Gamma irradiation is used to manipulate surface recombination *in-situ* to illustrate the impact surface recombination can have on single event phenomena. Chapter VI builds upon the results of Chapter IV and V to describe the role of surface recombination in single event phenomena. A comparison of surface recombination velocities along other insulating interfaces is presented as well as models of surface recombination for other scaled technologies. Chapter VII highlights the important conclusions of this dissertation.

CHAPTER II

BACKGROUND

20th century advances in physics enabled the rapid development of electronics to use in post-World War II space and military endeavors. Electronics enabled the computation and instrumentation revolutions that followed. As our capabilities have advanced, our proclivity to place electronic systems in environments which contain significant quantities of radiation has increased. In fact, our understanding of radiation environments largely comes from observations made by pioneering instrumentation. This chapter introduces several watershed moments in the study of radiation effects on electronics (see Fig. 1) and continues on to describe the mechanisms by which radiation interferes with the normal operation of electronic devices. The intention of this section is to give the reader an understanding of the physical environments where single event phenomena are a concern and a baseline understanding of the physical mechanisms that lead to the

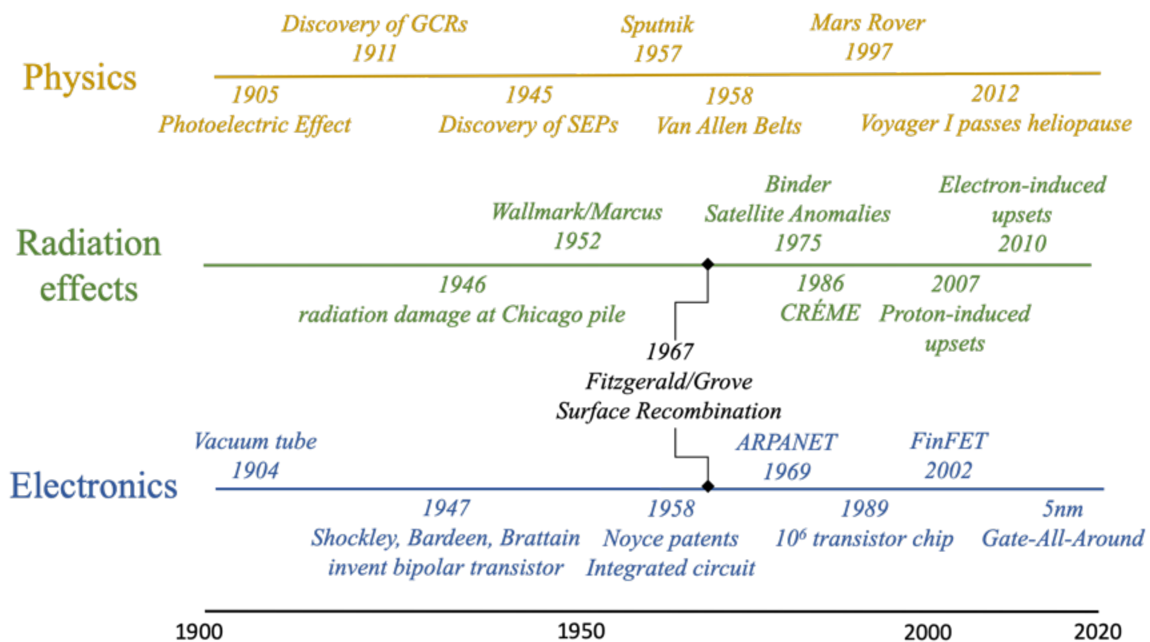

Fig. 1. Timeline of developments in physics, electronics and radiation effects.

occurrence of single event phenomena, especially single event transients and upsets. This chapter

ends by discussing the physics of accumulated ionizing dose effects (Total Ionizing Dose, TID) and surface recombination in preparation for Chapter's III, IV, and V which describe the role of surface recombination in single event phenomena.

II.1 Radiation environments

In a series of balloon ascents in 1911-1912 Victor Hess discovered the presence of energetic particles penetrating into Earth's atmosphere (he received the Nobel prize for this discovery in 1936) [2]. It was determined that the particles he measured originated from outside our solar system and they were termed galactic cosmic rays (GCRs). Primarily accelerated in the wake of supernovae, Fig. 2 depicts the flux of several constituent elements of the galactic cosmic ray spectrum, with the high energy part of the spectrum shown in the left panel [3]. On the right are low energy GCRs which were first measured in 2012 by the Voyager I spacecraft as it reached

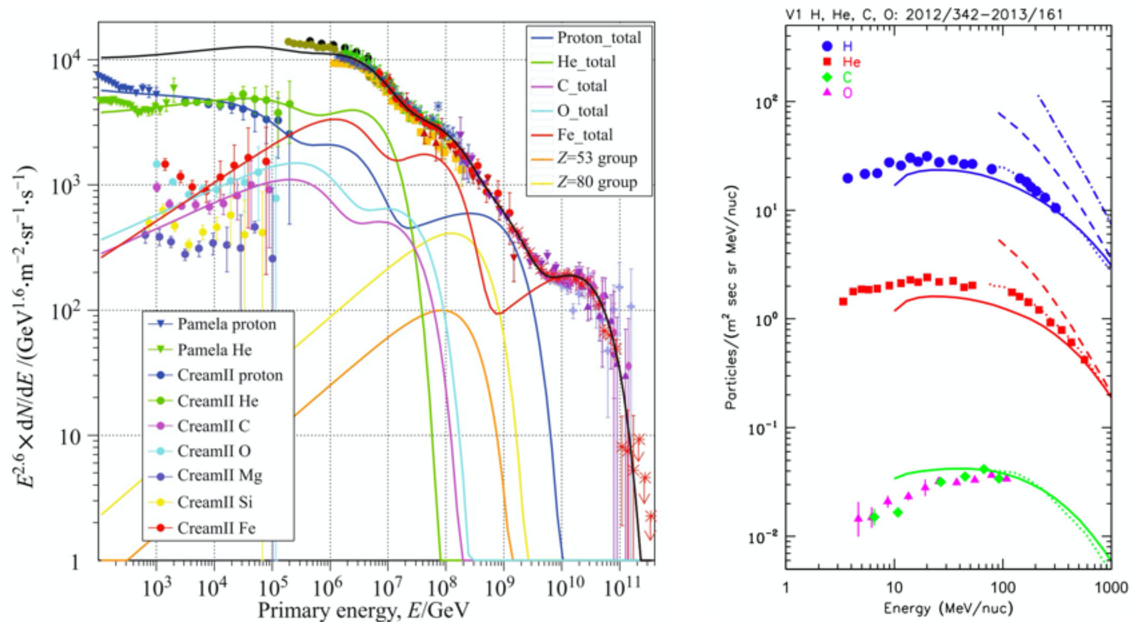

Fig. 2. High energy galactic cosmic ray energy spectrum for a variety of elements [3] (left). On the right is the low energy spectrum for several light elements, only recently attainable by the Voyager spacecraft [4].

an outer portion of our sun’s heliosphere [4]. The GCR spectrum features light and heavy elements over a wide range of energies with hydrogen, helium, oxygen, and iron being particularly abundant.

In addition to GCRs, the activity of our sun produces solar energetic particles (SEPs). First reported by Forbush in 1945 [5], SEPs emanate from the sun during solar flares and coronal mass ejections [6]. Fig. 3 contains new solar activity data taken from the Parker solar probe (PSP) mission [7]. The trajectory of the probe is plotted with the measured low energy particle flux (< 200 keV) charted on the inside of the track and the high energy particle flux on the outside (1-2 MeV). The measured particle flux is primarily composed of protons and can be seen to vary significantly throughout the PSP orbit. While solar flares and coronal mass ejections can occur at random times, a cycle of rising and waning solar activity repeats over approximately 11 years [8].

The energy spectra and flux of GCRs is modulated by solar activity and attenuated by shielding it may pass through. In Fig. 4 several flux-energy spectra are shown for geosynchronous

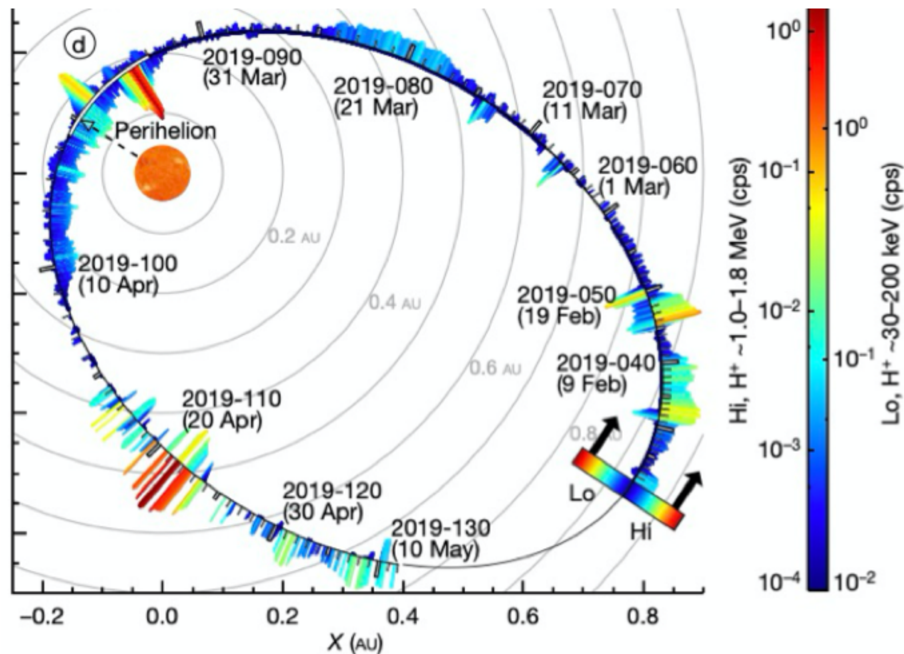

Fig. 3. Parker Solar Probe measurements of the solar energetic particle environment [7].

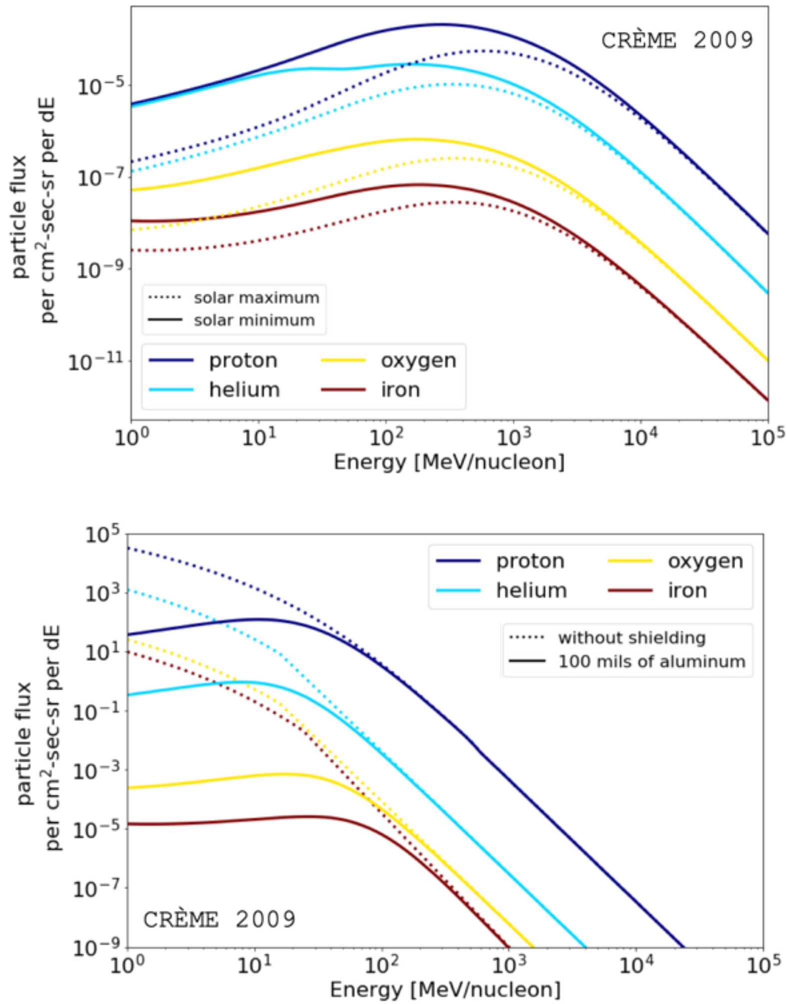

Fig. 4. Top: GEO particle flux spectra generated by CRÈME 2009 are shown for different solar conditions, solar maximum and solar minimum. Bottom: Worst day condition with and without 100 mils of aluminum shielding.

orbit (GEO). At solar maximum the particle flux in GEO is lower than at solar minimum, especially at lower particle energies. However, on the worst day for solar activity the particle flux increases dramatically. Shielding is used to reduce the particle flux that can reach sensitive electronics. In the bottom of Fig. 4, the efficacy of shielding is shown to be greatest with low energy, high Z particles. Measuring and developing models of these environments is an extensive effort. The Cosmic Ray Effects on MicroElectronics (CRÈME) simulation suite, originally developed by the Naval Research Lab [9], [10], is a useful resource for modeling radiation environments [11].

GCRs and SEPs collide with the electrons and nuclei of molecules in Earth's atmosphere, producing cosmic ray showers. A cosmic ray shower is a chain reaction resulting in the production many secondary particles including alphas, protons, neutrons, muons, and pions. A peak in the ionization intensity of cosmic ray secondaries occurs at an elevation known as the Regener-Pfotzer maximum [12]. A cosmic ray shower is illustrated in the top of Fig. 5 and the flux of muons,

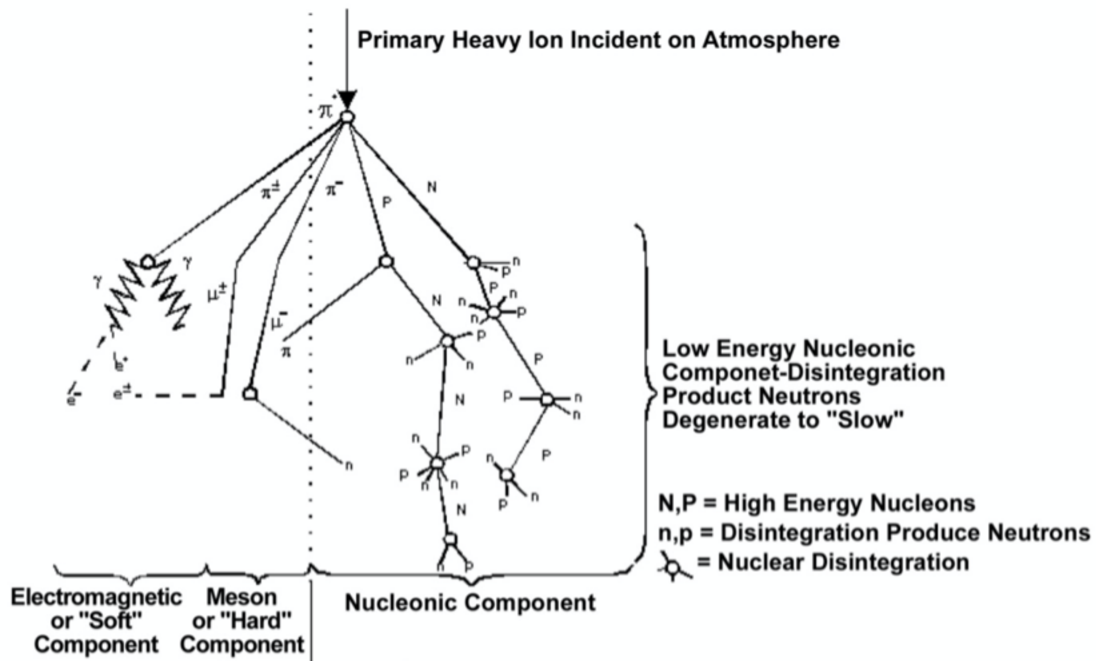

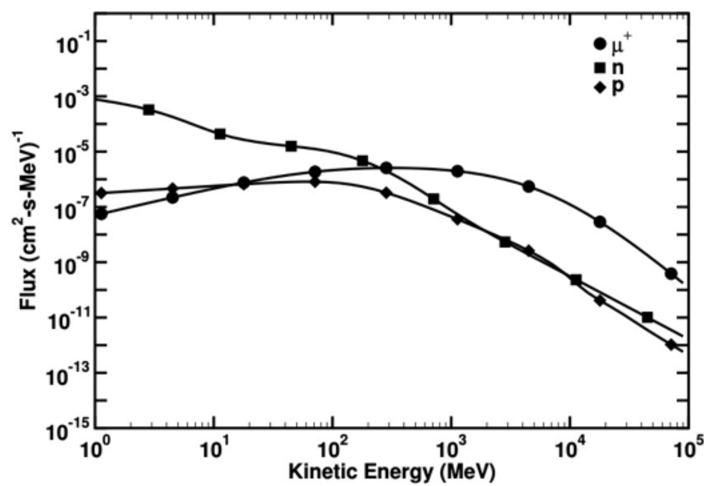

Fig. 5. Top: Cosmic ray shower is depicted. Bottom: Terrestrial flux spectrum of muon (μ), neutrons (n), and protons (p) at sea level.

neutrons, and protons at sea level can be found at the bottom. The terrestrial radiation environment varies with elevation and solar activity. SEP events can result in very high ground level enhancements (GLEs) of the particle flux [13].

The interaction of GCRs and SEPs with Earth's magnetic fields generates another important particle radiation environment. Discovered in 1958, the Van Allen Belts consist primarily of protons and electrons oscillating along Earth's magnetic field lines (shown in Fig. 6). The particle flux within these belts and the slot region between them is subject to change with

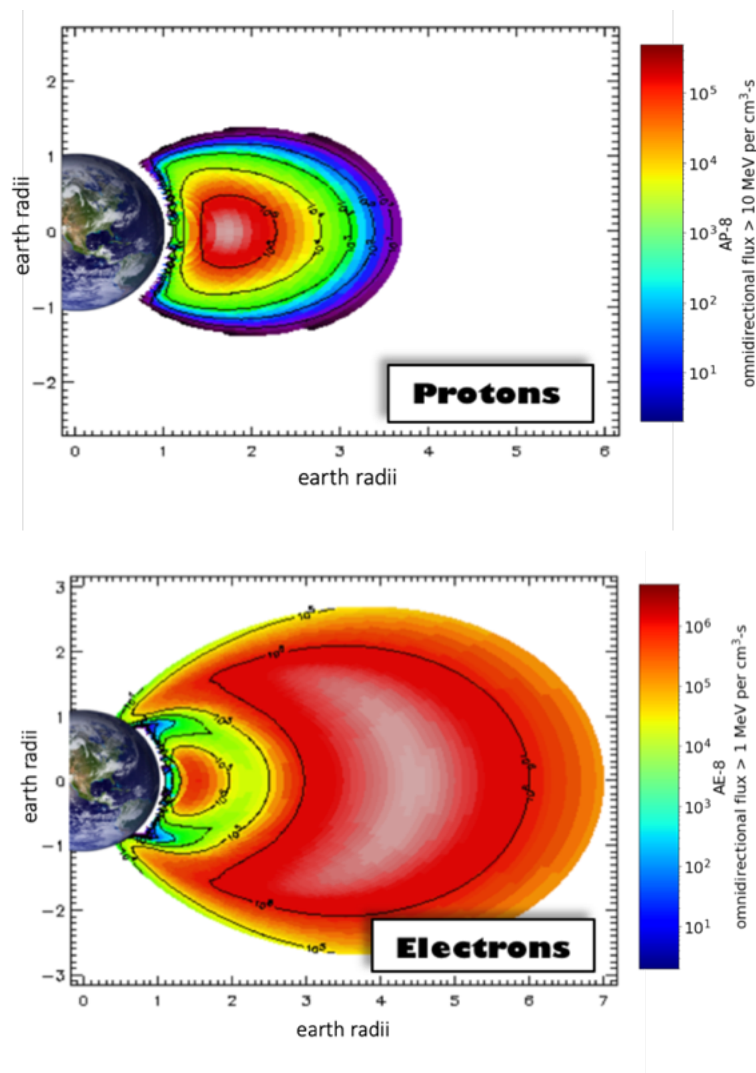

Fig. 6. Primary particle composition of the Van Allen Belts. Top: AP-8 omnidirection flux of protons with an energy above 10 MeV. Bottom: AE-8 omnidirection flux of electrons above 1 MeV.

cosmic ray fluctuations and solar activity. The AP-8 (proton) and AE-8 (electron) models are shown in Fig. 6. Low Earth orbit (LEO) occurs at less than 1/2 Earth radii and experiences a high flux of trapped protons and electrons, while GEO is at greater than 5 Earth radii, out of the reach of trapped protons but at increased exposure to GCRs and SEPs.

For a planet to form surrounding trapped radiation belts, the planet's magnetic dipole moment must be strong enough to capture SEPs and GCR particles before they enter that planet's atmosphere. Jupiter's large and strong magnetic field manifests a famously harsh trapped radiation environment [14].

Each of the naturally occuring radiation sources presented, GCRs, cosmic ray showers, SEPs, and trapped radiation belts present reliablilty concerns for electronics operated within them. For example, NASA's Solar and Heliospheric Observatory satelitte (SOHO) has been used to capture images of corona mass ejections (CMEs) with it's charge-coupled device (CCD) imaging array and on multiple occasions it has taken a direct hit by SEPs, despite possessing significant shielding. In Fig. 7 a CME is captured by a fully functional imaging array on the left, while a

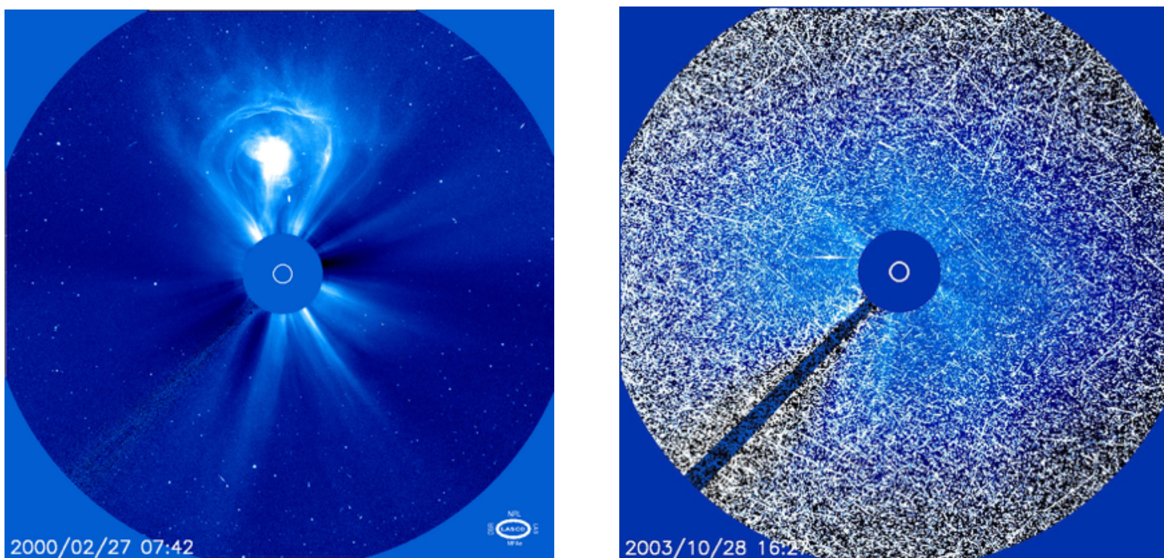

Fig. 7. Left: Solar flare captured by the Solar and Heliospheric Observatory, SOHO. Right: SEPs impinge upon SOHO's focal plane array, producing radiation effects in many of CCD pixels.

“snowstorm” of SEP radiation effects are observed in the imager on the right that disrupt instrument functionality. The immense cost of satellite and spacecraft technologies make the design of high-reliability electronics essential.

Barth [8] and Xapsos [15] have provided thorough reviews of the natural radiation environments of concern for radiation effects on electronics. Table I provides a summary of different particles and their maximum energies. Although shielding can be effective at reducing the flux of trapped protons and electrons, high energy SEPs and GCRs are very penetrating, making the required shielding thickness impractical and the design for SEE critical.

TABLE I
MAXIMUM ENERGIES OF PARTICLES

Particle Type	Maximum Energy
Trapped Electrons	10s of MeV
Trapped Protons & Heavy Ions	100s of MeV
Solar Protons	GeV
Solar Heavy Ions	GeV
Galactic Cosmic Rays	TeV

In addition to the aforementioned extraterrestrial sources, the natural radioactive decay of materials on Earth can be an important source of radiation to consider, such as the emission of alpha particles by boron-10 [16]. Furthermore, man-made sources of radiation can introduce significant radiation effects in electronics. Important man-made sources include the machines and radioactive sources used in medical imaging and treatments, high-energy physics experiments, nuclear power plants, and military activities.

Early radiation-reliability concerns centered around the creation of atomic defects, known as displacement damage, by protons and neutrons in nuclear reactor materials [17] and bipolar junction transistors [18]. Immediately after the development of metal-oxide-semiconductor field effect transistors (MOSFETs), the study of radiation-induced charge trapping in gate oxides began [19]–[21]. For many decades the growing use of metal-oxide-semiconductor (MOS) devices with Moore's Law scaling made total ionizing dose (TID) the predominant concern. In the last couple decades, SEE has become the major radiation-reliability issue for electronics. In 1962 Wallmark and Marcus predicted that circuit scaling would inevitably lead to an intolerable sensitivity to SEE [22] and in 1975 the first SEE anomalies produced by GCRs were published from Binder [23]. Several years later, in 1978, May and Woods observed that alpha particles produced in radioactive decay were producing soft errors in dynamic memories [24]. Motivated by these early observations, the study of SEE has been given significant experimental [25] and modeling [26], [27] attention. A phenomenological description of each class of radiation effects is below:

Single event effects

Occurs when individual ionizing particle radiation creates electron-hole pairs in semiconducting materials through electronic stopping processes. This is a transient radiation effect because it occurs over a short period of time. Further description in Chapter II.2 and II.3.

Total ionizing dose

Occurs when ionizing radiation creates electron-hole pairs in insulating materials through electronic stopping and photoelectric absorption that result in cumulative effects over time. Further description in Chapter II.4.

Displacement damage

Occurs when lattice atoms are knocked out of crystalline lattice locations by particle radiation via nuclear stopping processes and subsequently form stable defect sites and/or clusters of disordered atomic arrangement. Defect sites accumulate with radiation dose and act as recombination centers that lead to Shockley-Read-Hall recombination and decrease in carrier lifetime or these defects can scatter mobile carriers, decreasing their mobility.

In preparation for the next sections, we will provide a succinct overview of the physics associated with SEE to orient the reader prior to detailed discussion in the following sections. Three distinct physical processes occur during a single event and are illustrated in Fig. 8 [28]. In the first process, particle radiation (e.g., a charged ion, proton, etc.), with a specific energy and direction, passes through the material and loses energy via ionization. A dense column of ionized electrons and holes is created along the ion track, seen in Fig. 8a. If there is not an electric field present from an intersected or nearby junction, diffusion and recombination of the charge carriers is all that will occur. The second process, drift charge collection, will occur if an electrical junction

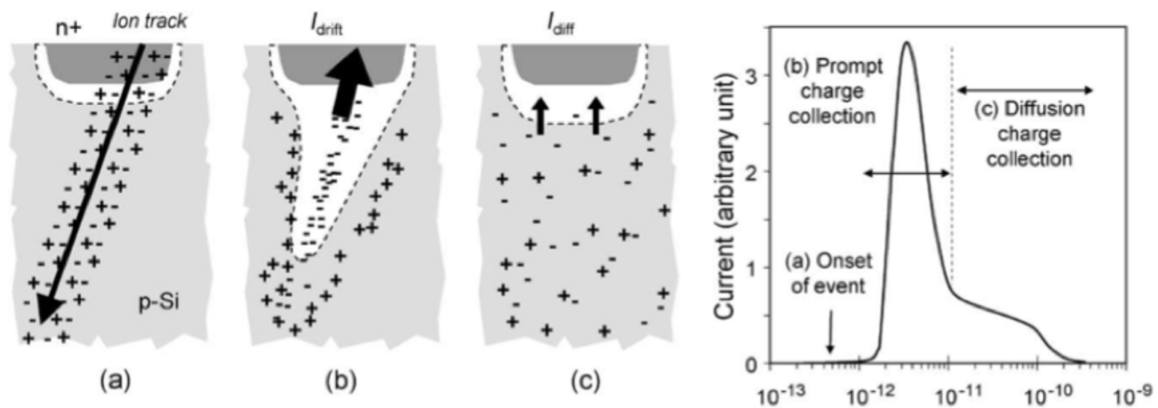

Fig. 8. A single ionizing particle passes by a N^+P junction creating electron-hole pairs that are collected by drift and diffusion. The collected charge profile shows a peak from drift collection and then sustained collection from diffusion [28].

is struck directly or is in sufficiently close proximity. The potential gradient of the junction (electric field) will be redistributed according to the conductivity of the ion track [29], visualized in Fig. 8b. This redistribution of the potential enables charge to be collected through drift beyond the original electric field region and a peak in current is observed (prompt charge collection). Electron-hole pairs separate during drift in an electric field, which reduces the amount of recombination that occurs. During the third process, illustrated in Fig. 8c, the remaining excess charge carriers are collected by diffusion until equilibrium conditions are re-established.

The rate of energy loss, $\mathrm{dE/dx}$, for specific ions and energies is used to approximate the amount of charge that will be generated while passing through a sensitive volume. The charge generated along a linear path based on ion energy loss is shown in Eq. 1 and 2. Units of linear energy transfer, LET, are commonly used to calculate the charge generated, Q_{gen}, along a path length, ℓ, in a specific material with density, ρ, and electron-hole pair creation energy, E_{ehp}.

$$\mathrm{LET} = -\frac{1}{\rho}\frac{\mathrm{dE}}{\mathrm{dx}} \left[\frac{MeV \cdot cm^2}{mg}\right] \tag{1}$$

$$\mathrm{Q_{gen}} = \frac{\mathrm{LET} \cdot \rho \cdot \ell}{\mathrm{E_{ehp}}} \tag{2}$$

Energy is converted to charge under the assumption that, on average, it takes 3.6 eV of deposited energy to create 1 electron-hole pair in silicon (or 22.5 MeV = 1 pC in silicon). This assumption is discussed further in Section II.2. Simulations and experiments can be used to determine how much of the charge will be collected at critical circuit nodes based on where it is deposited [30], [31]. Using the energy-to-charge conversion factor for silicon, the amount of

charge that is collected at a node, Q_{col}, is the energy deposition, E_{dep}, in a particular region, i, multiplied by the region-specific charge collection efficiency, α_i, summed for all sensitive regions, N, as shown in Eq. 3.

$$Q_{col,i} = \frac{1\ \mathrm{pC}}{22.5\ \mathrm{MeV}} \sum_{i=1}^{N} \alpha_i E_{dep,i} \tag{3}$$

The collected charge can then be compared to a critical charge parameter known to result in a propagating voltage transient or the upset of a memory element (respectively termed a single event transient, SET, or a single event upset, SEU). In SEE modeling, current pulses representative of different amounts of charge deposition can serve as an input parameter in a circuit or system simulation to evaluate its effects [32]–[36].

The threat an environment possesses for producing SEE is governed by the flux of particles with sufficient LET to create effects after penetrating in sensitive electronic volumes. The particle environments of greatest concern are:

- trapped ion belts,
- solar energetic particles,
- GCRs, and
- secondary products of high energy particle interactions, including neutron secondaries.

For a given particle-flux composition of an environment, an integral LET spectrum can be determined. In Fig. 9 the energy spectrum of particle fluxes for a GEO orbit is converted into an

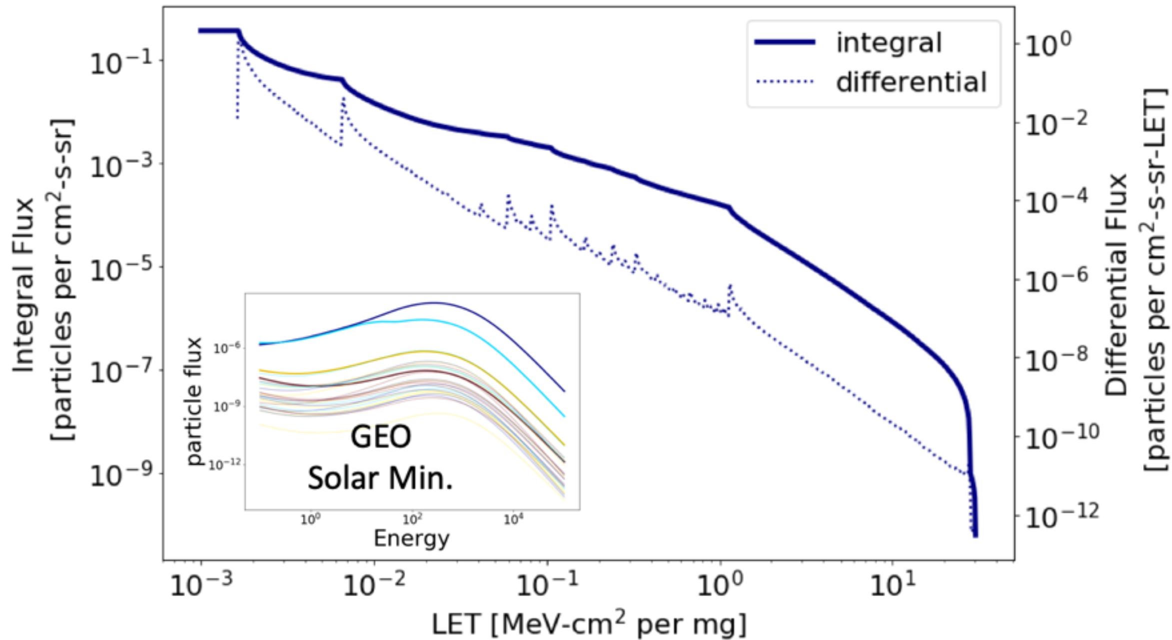

Fig. 9. LET spectrum within 100 mils of aluminum shielding in GEO during a period of minimum solar activity (flux spectra representing 28 elements shown inset).

integral and differential LET spectrum. An integral LET spectrum allows an engineer to quickly identify the flux of particles with sufficient LET to be a concern. For example, the flux of particles that exceed an LET threshold of 10^{-1} MeV-cm^2 per mg is 10^{-3} per cm^2-sec-steradian in a GEO orbit during solar minimum.

An SEE reliability estimate can be made by comparing the LET spectrum, the dimensions and sensitivity of individual devices, and the sensitivity of circuits. While understanding the mechanisms that govern the sensitivity of individual devices is the focus of this dissertation, a general trend of increasing sensitivity is predicted with Moore's Law Scaling. As can be seen in Fig. 10, the energy deposition required to introduce an effect decreases with technology scaling; therefore, the flux and variety, of SEE-inducing particles will tend to increase [37].

Recent works by Sierawski [31], [38] King [39], [40], and Trippe [41], [42] have studied how lightly ionizing protons, secondary electrons, and muons are increasingly important for SEE.

Mitigation techniques for SEE, including temporal and spatial redundancy and error detection and correction (EDAC) are frequently employed, but optimizing their implementation and identifying persistent vulnerabilities requires simulation and testing. In the next sections, a physical understanding of single-event charge generation and collection is developed to fortify the assumptions that will be used when quantitatively modeling SEE in Chapter IV.

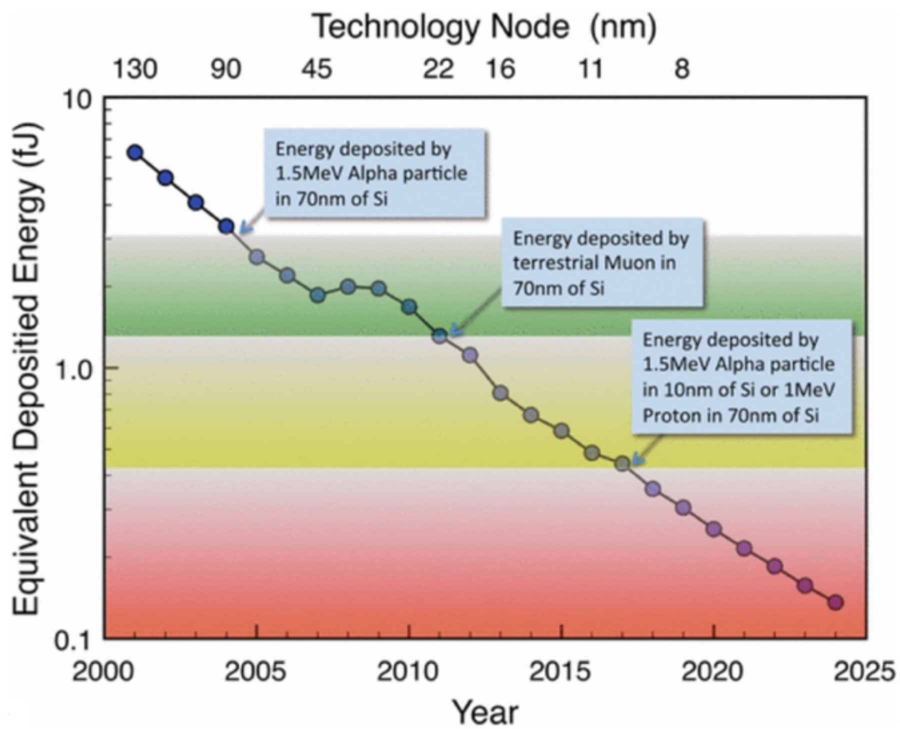

Fig. 10. Increasing sensitivity of electronics to energy deposited during a single event with continual Moore's Law scaling [37].

II.2 Mechanisms of radiation energy deposition

The first process to consider when studying radiation effects in electronic devices is the initial transfer of energy between the radiation and the materials that comprise the electronic device. Photons and particle radiation transfer energy to nuclei and electrons in distinct ways as they pass through materials. The experimental results in this dissertation are the result of direct ionization by particle radiation; however, a general understanding of radiation-matter interactions is useful and provided in this section.

II.2.1 Photon energy deposition

Photons can transfer energy to materials via the photoelectric effect, Rayleigh scattering, Compton scattering, positron-electron pair production, and photo-nuclear reactions. In Fig. 11 the dominant process as a function of photon energy and the atomic number ("Z") of the target material is shown. At low energies, the photoelectric effect dominates, where photons are absorbed in the process of exciting a valence electron into the conduction band, leaving behind a hole. For single photon photoelectric absorption, the incident photon must possess energy greater than the target material's bandgap energy and in indirect gap materials, such as silicon, additional phonon interaction is required to conserve momentum. In silicon, the photoelectric effect is dominant until an energy of 80 keV (hard x-ray).

Above 80 keV, Compton scattering becomes the most likely energy transfer process. Compton scattering is where the incident photon ionizes an atom, producing an electron (while transferring some portion of its energy to that electron). In Compton scattering the original photon is not absorbed in the interaction. The scattered photon continues along with reduced energy, a scattered angle, and can potentially ionize further atoms. The Compton-scattered electron may also

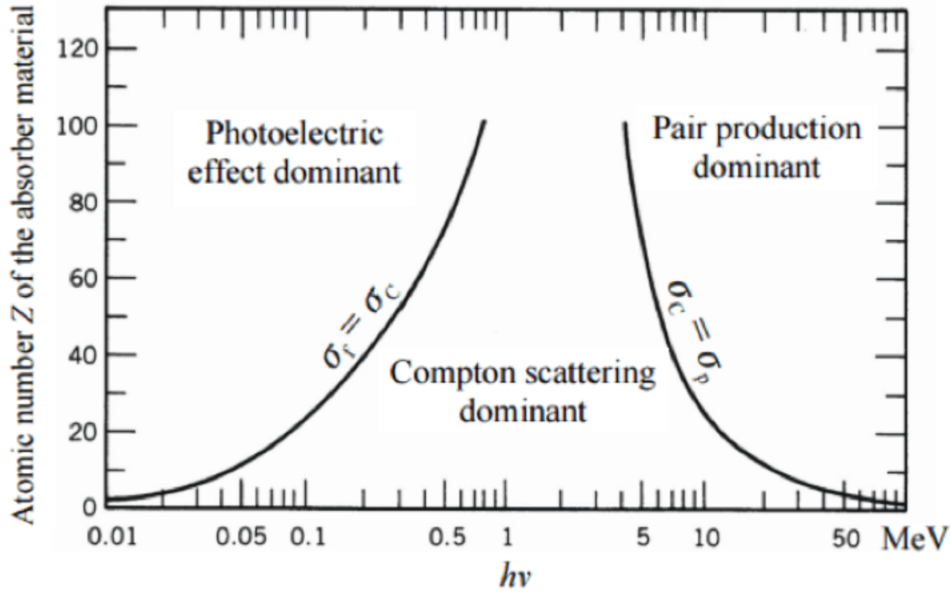

Fig. 11. Energy and target material dependence of photon interactions. At low photon energies, the photoelectric effect is dominant.

ionize additional electron hole pairs. In silicon with photons possessing 10 MeV or greater, the most likely interaction becomes electron-positron pair production. Photoelectric absorption, or optical absorption, produced by low energy photons with ultra-fast lasers can be used to probe the sensitivity of electronic circuits to charge deposition [43]; however, non-linear optical processes, reflections and diffraction by complex material structures makes interpreting and relating results for SEE an involved process [44], [45].

II.2.2 Particle energy deposition

When particle radiation (e.g., an energetic ion, neutron, or subatomic particle) passes through a material it can transfer energy through ionizing and non-ionizing interactions. Three primary interactions are illustrated in Fig. 12. On the top is a cartoon illustration of each interaction and on the bottom are example particle tracks produced using the Monte Carlo Radiative Energy Deposition, MRED, radiation transport tool [46]. MRED is built on GEANT4 particle physics libraries [47], as well as several others, that use the binary collision approximation (BCA) and

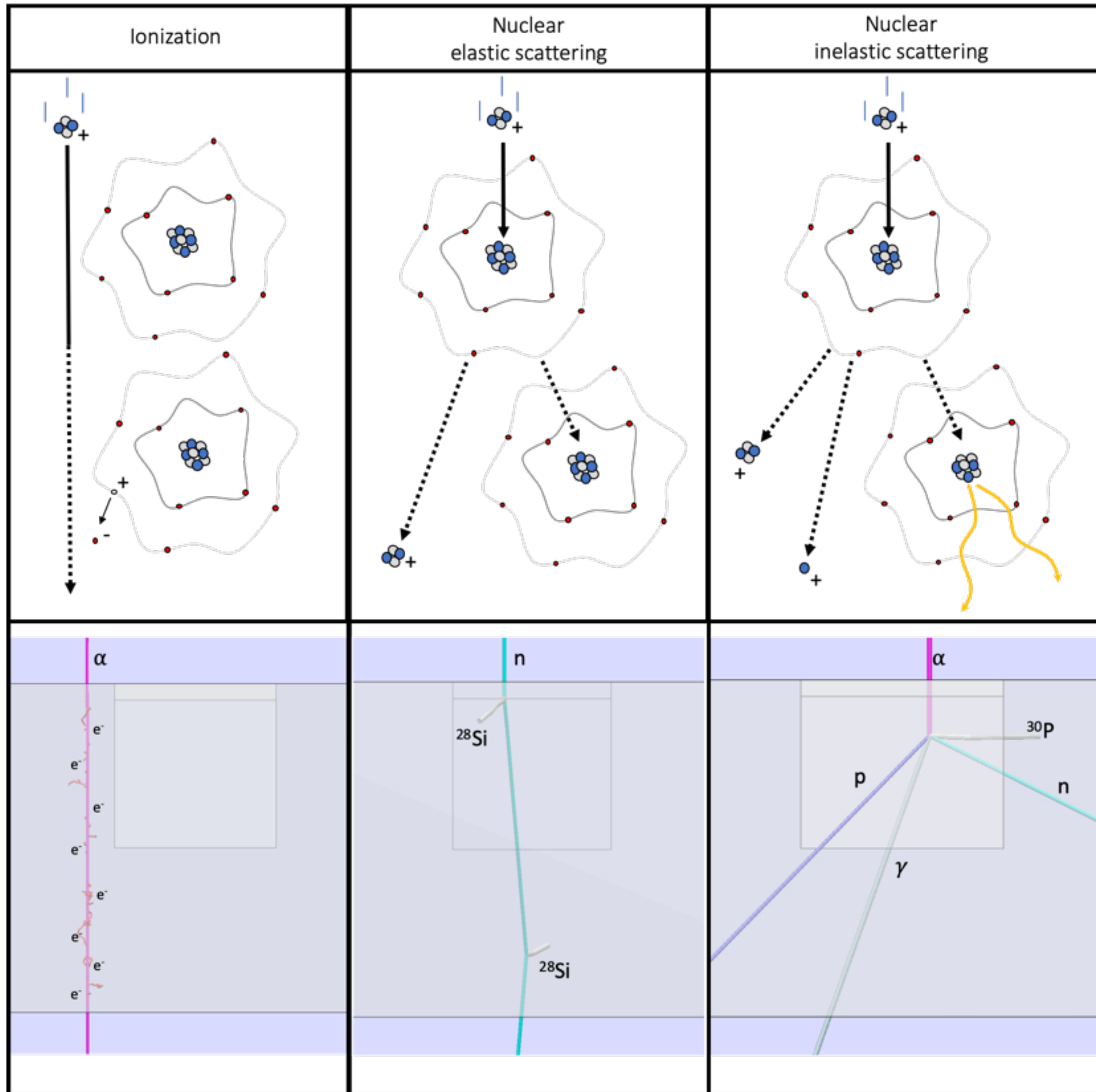

Fig. 12. Particle-matter interactions. The top panels illustrate three types of particle interactions that result in energy deposition. Example track structures produced by a Monte Carlo radiation transport tool, MRED, are shown in the bottom panels.

Monte Carlo methods to sample radiation-matter interactions and calculate corresponding particle tracks. Ionization is depicted on the left in Fig. 12. Ionization occurs when an ion passes near an atom in the target material and transfers energy through Coulombic forces to its electrons, allowing them to delocalize from that particular atom producing conduction band electron/valance band hole pairs. This process occurs readily with many electron-hole pairs being produced along the ion

track. The middle process in Fig. 12 is elastic nuclear scattering, where an ion scatters off the nucleus in an elastic nuclear collision, transferring some of its energy to the nucleus. In order for the ion to collide with the nucleus it must overcome the repulsive force between the positive charge of the ion and the positive charge of the nucleus (e.g., the Coulomb barrier). Eq. 4 is the amount of energy required by an ion to overcome the Coulomb barrier. The Coulomb barrier is a relationship between the atomic number, Z, and atomic mass number, A, of the incident ion and target atom (denoted by subscript 1 and 2, respectively).

$$U_{coul} = 1.03 \times \frac{A_1 + A_2}{A_2} \times \frac{Z_1 Z_2}{A_1^{\frac{1}{3}} + A_2^{\frac{1}{3}}} \quad (4)$$

The Coulomb barrier for protons in silicon is approximately 4 MeV. Un-charged neutrons do not feel the Coulombic repulsion from the nucleus and participate in elastic nuclear scattering at low energy. If enough energy is transferred to the nucleus by either an ion or neutron it will leave its normal position in the material (i.e., displacement damage). The energy of the recoil atom, E_{recoil}, with mass m can be calculated using eq. 5 based on the incident ion energy, $E_{incident}$, angle $\boldsymbol{\theta}$ and mass M.

$$E_{recoil} = \frac{4mM}{(m + M)^2} E_{incident} \cos^2\theta \quad (5)$$

In a crystalline material, elastic scattering results in the creation of Frenkel pairs (vacancies and interstitials). However, if not enough energy is transferred to the nucleus to displace it, it will dissipate energy with atomic oscillations (e.g., phonons). When considering the importance of this

interaction to SEE, notice that both the primary ion and recoil nucleus have the potential to create further electron-hole pairs via ionization.

During an inelastic nuclear interaction, shown in the right of Fig. 12, energy is transferred from the ion to the nucleus and additional energy is liberated during nuclear relaxation processes. Inelastic processes include scattering, where the incident ion remains, or nuclear reactions, where the reacting particles undergo nuclear transmutation. An example inelastic interaction is below:

$$ {}_{0}^{1}n + {}_{14}^{28}Si \rightarrow {}_{12}^{25}Mg + {}_{2}^{4}He \qquad (6) $$

In this reaction a neutron impinges on a silicon atom resulting in the disintegration of the silicon atom into a magnesium and an alpha particle. Total energy is conserved; including the nuclear binding energy that may be liberated or consumed by the reaction. Although this work is primarily concerned with the direct ionization of ions interacting Coulombically, ionization from the secondary products of nuclear elastic and inelastic interactions are important to consider in SEE [48], [49].

The formulation of analytical expressions for energy loss by an ion as it passes through a material began with Niels Bohr and have been adapted to include more detailed physics. Hans Bethe [50] and Felix Bloch [51] developed an expression that describes mean energy loss for charged-heavy particles at moderate energies [52] ($0.1 \leq \beta\gamma \leq 1000$):

$$ -\langle\frac{dE}{dx}\rangle = Kz^2 \frac{Z}{A} \frac{1}{\beta^2} \left[\frac{1}{2} ln \frac{2m_e c^2 \beta^2 \gamma^2 T_{max}}{I^2} - \beta^2 - \frac{\delta(\beta\gamma)}{2}\right] \qquad (7) $$

In the Bethe-Bloch equation above, <dE/dx> is the mean energy loss, z is the incident ion's charge, Z and A are the atomic number and atomic mass number of the target material, m_e is the mass of an electron, c is the speed of light, β and γ are the standard kinematic variables (velocity relative to speed of light and Lorentz factor, respectively). T_{max} is the maximum kinetic energy that can be transferred to a free electron after a single collision and I is the mean excitation potential. K is a constant (0.307 MeV cm^2 mol^{-1}) that is related to the classical electron radius, r_e, and Avogadro's Number, N_A. The mean energy loss is strongly governed by the incident particle's velocity ($\beta = v/c$) and charge, z. Fig. 13 shows the LET for a variety of ions incident on silicon as a function of particle energy. There are order of magnitude differences in the rate of energy loss as the ion energy, or velocity, changes. The peak rate of energy loss for an ion in a material is known as the Bragg Peak.

The Bethe-Bloch analytical formulation approximates a mean rate of continuous energy loss that represents many discrete probabilistic scattering events. Straggle is the statistical variation

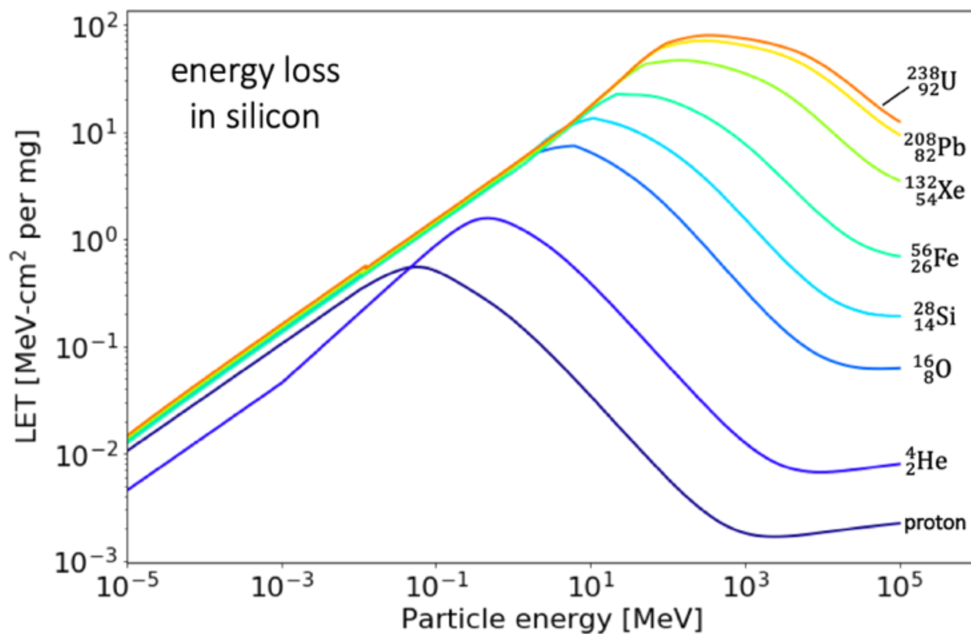

Fig. 13. LET vs. particle energy for different ions.

in energy loss. Straggle becomes important when a particle's energy is deposited across very short distances or the rate of energy loss changes rapidly (e.g., near the Bragg peak). To describe discrete probabilistic particle interactions, the BCA and Monte Carlo random sampling techniques have frequently been employed. Fig. 14 shows several probabilistic distributions of charge deposition generated using MRED to simulate silicon volumes of different thickness. More charge is deposited in thicker volumes, due to a longer path length across them and a broader statistical distribution is observable with smaller volumes due to ion straggling.

The rate of energy loss as a function of depth in a material is important to predicting SEE because sensitive volumes are frequently underneath many over-layers of material. Fig. 15 displays the LET of 35-MeV oxygen as a function of depth as it penetrates into silicon. The rate of energy loss increases as the ion loses energy until the Bragg Peak. The ion straggle that occurs when passing through 250 nm layers of silicon is visualized as shades of gray. With the assumption an electron-hole pair is created for every 3.6 eV deposited, the rate of charge deposition per µm is

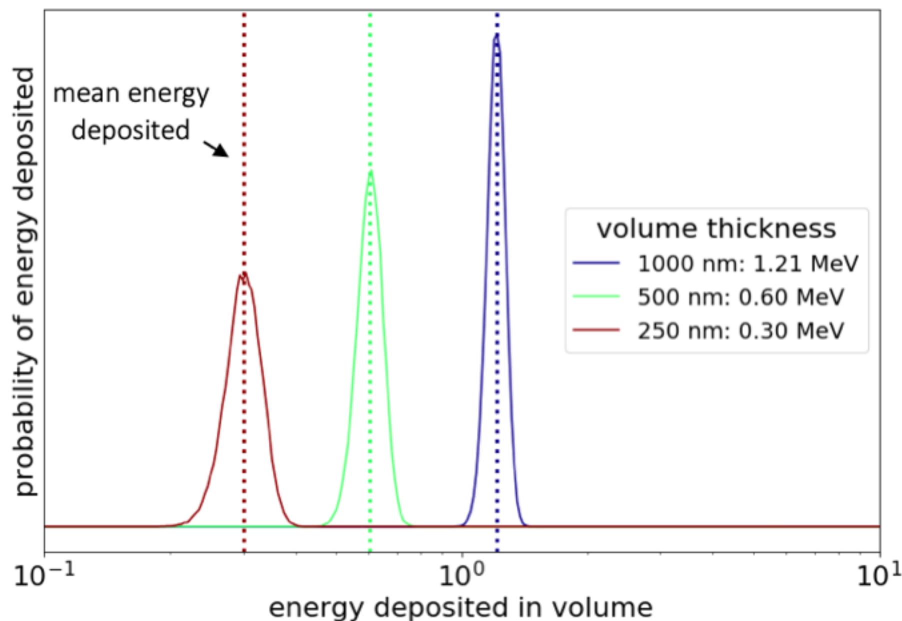

Fig. 14. Energy deposition distribution in sensitive volumes of different thickness. Statistical variability in energy deposition, straggle, is more evident across small volumes.

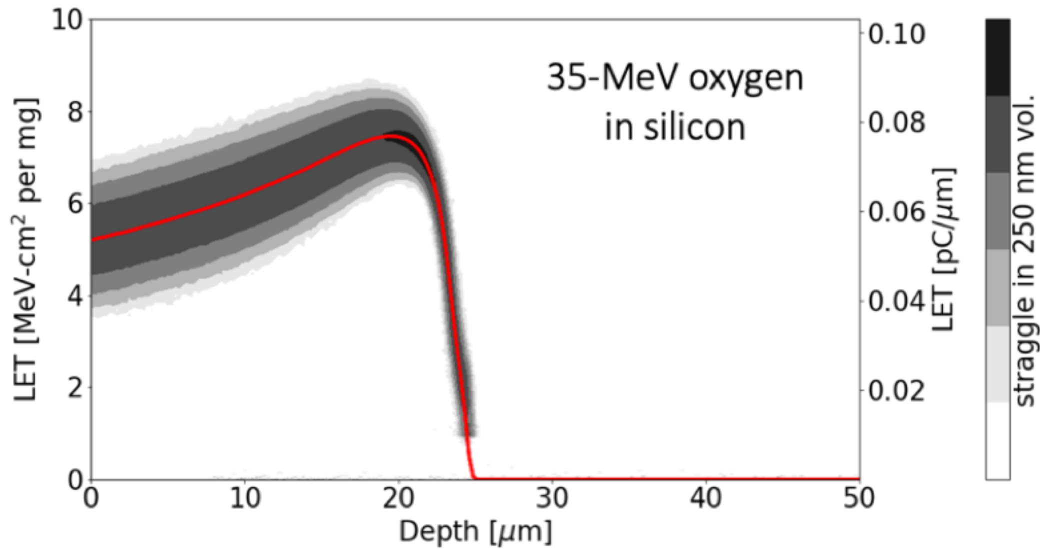

Fig. 15. LET as a function of depth as a 35-MeV oxygen ion penetrates into silicon. On the right axis is the LET converted to charge generated per µm. The shaded region illustrates the variation in LET that can occur across a 250 nm volume (e.g., ion straggle).

presented along the secondary y-axis. An LET of 10 MeV-cm^2 per mg is equal to approximately 0.1 pC/µm in silicon.

If the device in question is sensitive to ionization by secondaries, it becomes very important to consider the track structure of scattered electrons [31], [40], [53]. In Fig. 16, the density of carriers generated away from the central ion track is plotted for two different ions with the same LET, 5 MeV carbon and 5 GeV iron. The higher energy iron ion produces secondary electrons that scatter significantly further from the ion's path. This is visualized using MRED simulations in the bottom of Fig. 16. MRED is useful for calculating energy deposition produced in sensitive volumes by particles tracks, including those of secondary reaction products but cannot describe device physics (e.g., the collective motion of charges being acted upon by electric fields).

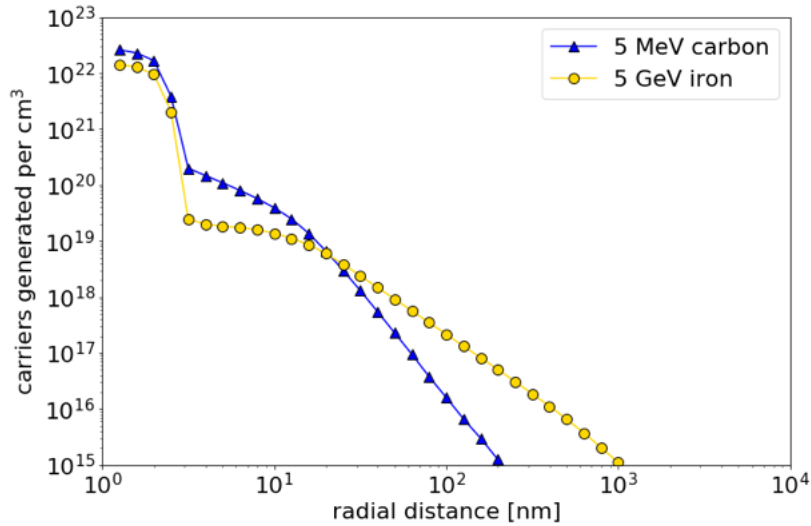

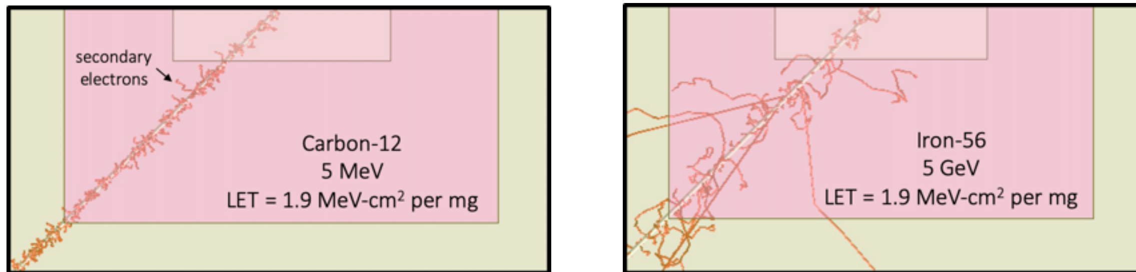

Fig. 16. The average energy, and range, of secondary electrons is proportional to the incident ion energy. Despite having the same LET, 5 GeV iron has a considerably larger track radius then 5 MeV carbon.

In Fig. 17 the location of ions impinging with normal incidence on a silicon sample with a central sensitive volume are plotted as simulated by MRED. MRED uses the BCA to generate and propagate secondary tracks accurately with energies as low as 100 eV. The amount of energy that is deposited by each ion in the sensitive volume is calculated and the ion's incident location is colored accordingly. For ion's that strike the sensitive volume directly, energy is deposited corresponding to direct ionization by the primary ion. Outside the volume, energy is deposited by secondary electrons that scatter away from the primary ion track into the sensitive volume. Considering track structure is especially important when using high energy ions (E > 100MeV).

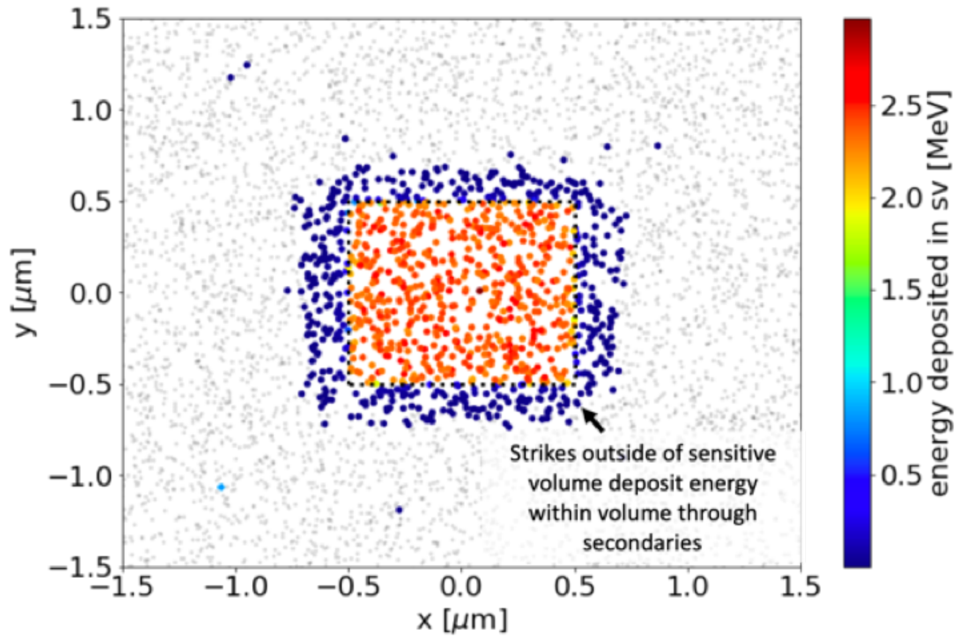

Fig. 17. Energy deposition events in a central 1 μm^3 sensitive volume plotted as function of the incident ion x and y location. Strike locations are colored according to the energy they deposit in the sensitive volume. Events that do not deposit energy in the sensitive volume are plotted as light gray dots.

For ions with 10s of MeV, the majority of energy deposited along secondary electron tracks remains localized within 10 nm of the primary ion.

While energy deposition is related to LET it is important to consider relaxation processes, beginning with scattered electrons. In the following section we will continue discussing the process of ionized carrier relaxation, or thermalization, to justify the use of a thermalized carrier distribution in quantitative modeling the role of surface recombination in single-event charge collection.

II.3 Mechanisms of single-event charge collection

After electron-hole carriers are generated by ionization in sensitive devices, they are acted upon by local forces. To model the collection of charge carriers at terminals in a device, drift and diffusion modeling governed by Poisson's equation solutions across a finite-element mesh grid has been employed [51]. To perform single-event simulations with finite-element methods (FEM), an excess carrier density distribution representative of an ion strike must be approximated. For the subsequent drift and diffusion calculations to be valid, the approximated carrier distribution should be thermalized (e.g., all relaxation processes, such as carrier-carrier and carrier-phonon scattering, should be in thermal equilibrium). In this section we discuss the thermalized carrier approximation and the physical mechanisms that are well-described by modeling single-events with FEM following this assumption.

II.3.1 Thermalized carrier assumption

As evidenced in the previous section, the electron-hole pairs that are produced by ionizing radiation can possess significant energy and range. Fig. 18 shows the different physical regimes a carrier traverses during relaxation from high energies. With carrier energy greater than 100 eV the binary collision approximation of individual, two-body scattering events is useful to describe the energy transfer in collisions. If carrier energy is 10 eV or less, transport can be described using the band structure description of infinite crystal lattices and associated scattering rates. In between the

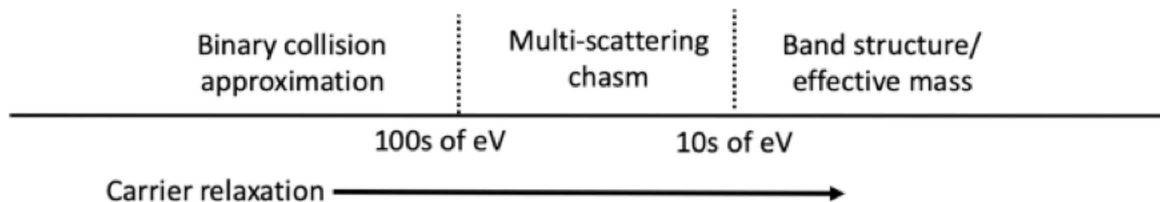

Fig. 18. Physical regimes traversed during carrier relaxation.

high energy and low energy range, carriers interact with the potential of more than one body simultaneously making the BCA inaccurate; however, high energy band structure and scattering rate calculations are not available/valid. This results in an energy region (a "multi-scattering chasm") where carrier transport modeling is difficult. In this work we assume that the excess carrier concentration does not change in an appreciable way while crossing the multi-scattering chasm during carrier relaxation (e.g., the range of electrons with 10eV $< E <$ 100 eV is negligible compared to device features).

Following this assumption, band-structure based methods can be used to approximate a thermalized carrier distribution. The plots in Fig. 19 visualize carrier relaxation through carrier-phonon and carrier-carrier scattering processes as simulated using a semi-classical carrier transport tool [54], [55] that implements electronic band structure up to 10 eV. A hot electron distribution (1-10 eV) is injected along a narrow Gaussian ion track radius (σ = 10 nm) and thermalizes within 2 picoseconds. The initially energetic carriers occupy energy-momentum states far from the conduction band minimum (bottom left of Fig. 19), leading their transport to be poorly described by the effective mass approximation necessary for drift and diffusion calculations. The effective mass approximation is only an accurate descriptor of carrier mobility when carriers are near the parabolic band minima/maxima. However, after 2 ps the majority of carriers return to the band minima (the conduction minima are the 6 ellipsoids while the valence minima is the central sphere in the bottom right of Fig. 19). The carrier distribution spreads radially away from the ion track with a 50 nm Gaussian distribution at 2 ps. Approximating that an ion track produces a thermalized carrier distribution over the course of 2 ps with a radius of 50 nm enables the use of drift and diffusion modeling of ion strikes. If device feature sizes are smaller than 50 nm or active processes are faster than 2 ps this assumption should be revisited. Following this same modeling technique

Fang *et. al* [56] recently confirmed the experimental measurement [57] that, following thermalization, a mean energy of 3.6 eV is deposited per electron-hole pair in silicon .

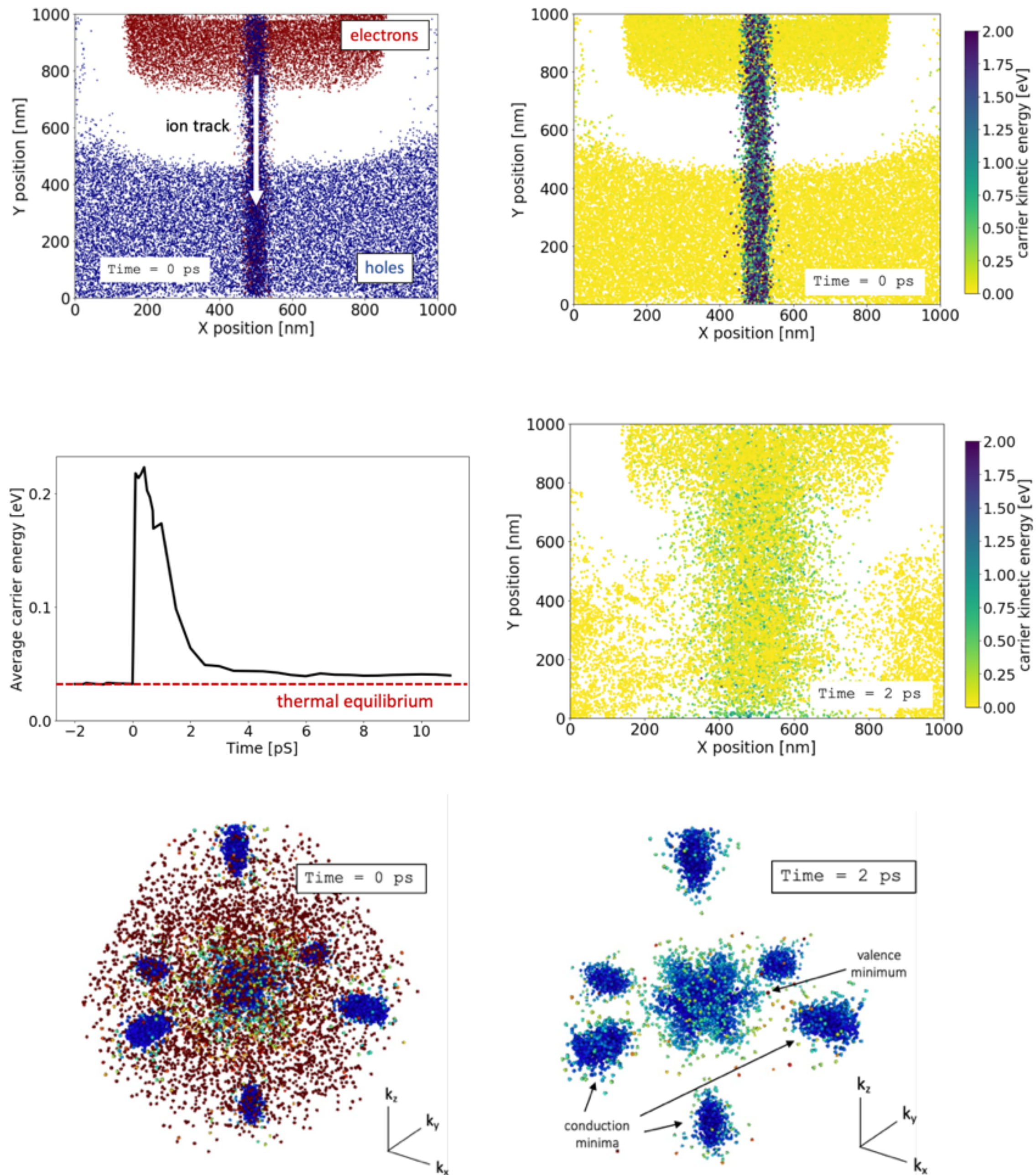

Fig. 19. Electron and hole thermalization after ion strike. In the top figures a dense column of energetic electron-hole pairs crosses an n^+p junction. The average energy of carriers in the device returns to equilibrium after 2 ps (middle). In k-space, the initial high energy carriers (0 ps) occupy positions in the band structure far from the conduction and valence band minima until they are thermalized (2 ps).

A Gaussian thermalized carrier distribution enables FEM of single event effects. In Fig. 20, this common approximation is compared to two different ion tracks on the left. On the right in Fig. 20, the spatial and temporal ion track carrier distributions used in this work are shown. Temporal ramping of the charge generated is used in FEM to prevent computational convergence issues. For moderate injection conditions, a 2 ps time constant is typically used and is short compared to charge collection processes but longer than carrier relaxation processes.

The Synopsis Sentaurus TCAD package is used to perform FEM of single-events and other device physics in this dissertation. The simulations are based on solving the device physics equations. Poisson's equation is used to determine the distribution of the electrostatic potential according to the net charge concentration of ionized impurities and free carriers across the finite-element mesh. Drift and diffusion of electrons and holes is calculated based on the electric field, carrier mobility (derived using the effective mass approximation) and carrier concentration gradients. A doping-dependent mobility model is required for the devices simulated in this work

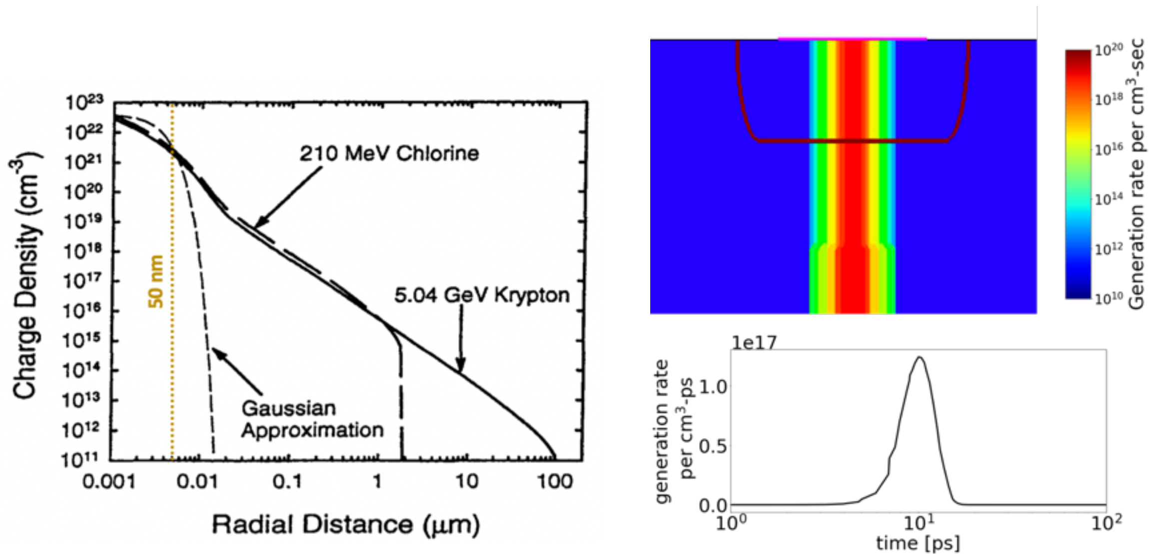

Fig. 20. Thermalized carrier assumption. A Gaussian distribution of electron-hole pairs with a radial standard deviation of 50 nm adequately captures track structure and carrier relaxation effects for modeling subsequent drift and diffusion processes. On the right, an example Gaussian temporal and spatial charge distribution is shown as commonly implemented in FEM of SEE.

due to heavily doped regions. Important generation and recombination processes, including surface recombination, are included in simulation via the continuity equations. The device physics equations are listed below:

Poisson equation

$$\nabla^2 \varphi = -\frac{\rho}{\varepsilon} \tag{8}$$

$$\frac{d\boldsymbol{E}}{dx} = -q(N_D - N_A + n - p) \tag{9}$$

Drift and diffusion

$$\boldsymbol{J_n} = q\mu_n n\boldsymbol{E} + qD_n n \tag{10}$$

$$\boldsymbol{J_p} = q\mu_p p\boldsymbol{E} - qD_p p \tag{11}$$

Continuity

$$\frac{dn}{dt} = \nabla\frac{\vec{\boldsymbol{J}}_{\boldsymbol{n}}}{q} + G_n - R_n \tag{12}$$

$$\frac{dp}{dt} = -\nabla\frac{\vec{\boldsymbol{J}}_{\boldsymbol{p}}}{q} + G_p - R_p \tag{13}$$

II.3.2 Junction charge collection

When a single ionizing particle crosses an electrical junction, the excess charge carriers generated lead to a redistribution of the potential as calculated with the Poisson's equation and are collected via drift and diffusion. In Fig. 21 this is illustrated for an n^+p diode. The carrier concentration along the length of the device is visualized along the energy bands as the distance

from the band edge. The rate of recombination occurring along the device is visualized at the bottom of the figure. Prior to the strike, a depletion region is formed between the n^+ and p-sides of the diode. Recombination/generation is negligible, although some generation occurs in the reverse

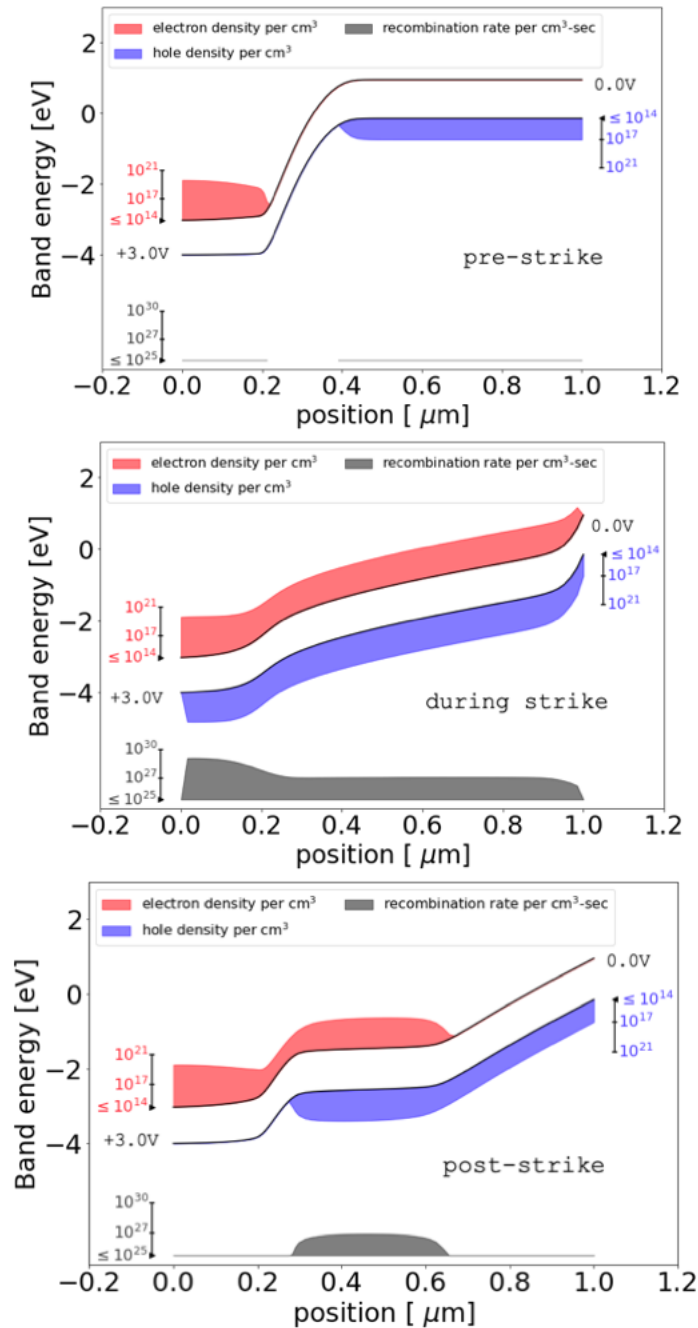

Fig. 21. Single-event charge collection in an n^+p junction. The electron and hole carrier concentrations are illustrated extending outward from the conduction and valence band, respectively. The rate of recombination as function of position is plotted below. During the ion strike, the energy band resembles that of a conductive wire with the electric field reaching into both end regions.

biased depletion region. During the strike the junction's electric field is redistributed into both end regions, especially the lightly-doped p-type region. Recombination occurs along the entire length of the device, especially in the highly-doped n-type region. After the strike (bottom), the junction electric field begins to re-establish while diffusing electrons and holes continue to recombine in the lightly doped p-region.

II.3.3 Voltage transients

The conductive ion track couples the potential on both sides of the struck junction. If the voltage at a contact is not maintained by a continuous current source (e.g., is hard-biased) the voltage at the contact may drop. In Fig. 22 the potential in the n^+p diode is visualized for two conditions: a hard-biased condition where the contact voltage is maintained by the simulation and a circuit-coupled condition where the current at the n^+ contact is limited by a resistor. In the circuit-

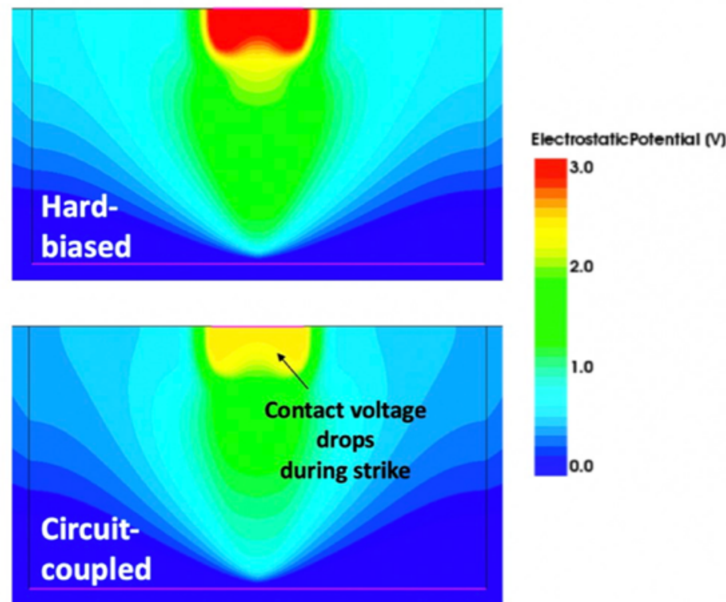

Fig. 22. Top: Potential distribution during strike of hard-biased diode. Bottom: a diode coupled into a circuit. The voltage at the n^+ contact drops in the circuit-coupled diode during the transient.

coupled condition, the voltage drops during the single event until it can be restored by current through the coupled resistor.

An important physical manifestation of single-event charge collection is a voltage transient at the output of an inverter. Inverters are used frequently in digital memory and logic circuits. For example, an SRAM cell that stores a single bit value (e.g., 0 or 1) is made using two cross-coupled inverters. In Fig. 23 a SET in an inverter is visualized. An ion strike in the drain of the off-state nmos device causes the output of the inverter (tied to both nmos and pmos drains) to drop as the transient current is collected. The current flowing at the output is limited by the current drive of the pmos device and exhibits a plateau during which the erroneous state is held [34], [35]. This

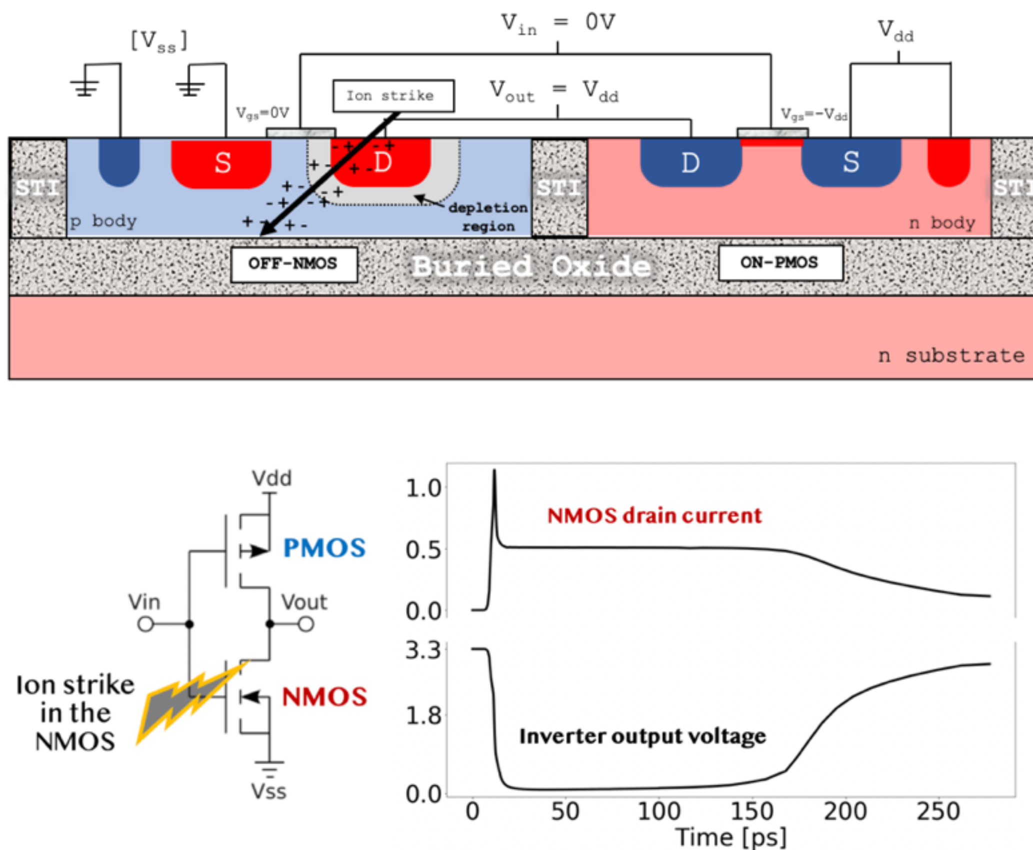

Fig. 23. Single-event transient in CMOS inverter. Top: Illustration of with the off-state nmos and on-state pmos. Bottom: Single-event charge collection can temporarily make the off-state nmos conductive and connects Vss (ground) to the inverter output.

erroneous state can become latched into memory or propagate through logic circuits, degrading system reliability if not appropriately mitigated.

II.4 Total ionizing dose mechanisms

Understanding TID mechanisms is necessary for the design of the *in-situ* surface recombination enhancement experiments in Chapter V. The study of TID effects in gate oxides, buried oxides, and shallow trench isolation oxides has a rich history that is covered thoroughly in [58]. Exposing the oxide regions in electronics to ionizing radiation can result in reliability concerns such as threshold voltage shifts, leakage current, and frequency-dependent noise [59]. TID effects typically result from the accumulation of defects and trapped charge in the oxides and along the semiconductor/insulator interfaces.

In Fig. 24, the process of interface and oxide trap formation from initial electron-hole pair generation is illustrated [60], [61]. Electrons are highly mobile and escape the oxide. Holes slowly transport towards the interface (moving up the sloped energy band with the electric field). A portion of the holes transfer their positive charge to contaminant hydrogen that also migrates to the interface. A subset of holes remain near the interface as oxide trapped charge and can influence the electrostatic potential and, depending on their distance from semiconductor regions, act as border traps. At the interface, a singly charged hydrogen may find another hydrogen atom loosely bound to an interfacial silicon atom and react to form gaseous hydrogen and leave a silicon dangling bond (bottom of Fig. 24) [62]. The introduction of hydrogen is a common defect passivating practice used in manufacturing and TID can act to reverse the passivation [63]. Silicon dangling bonds occur primarily as P_b centers [59], [64]. In addition to trapping charge, P_b centers have an energy level within the silicon bandgap which increases the interface's SRV. Poindexter

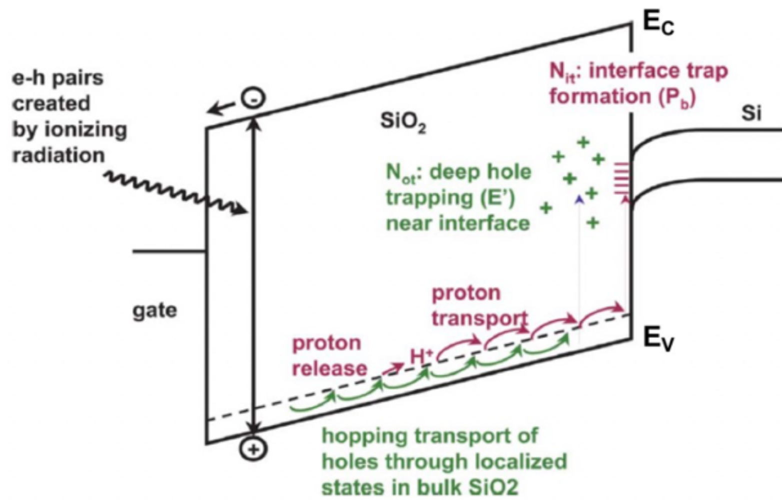

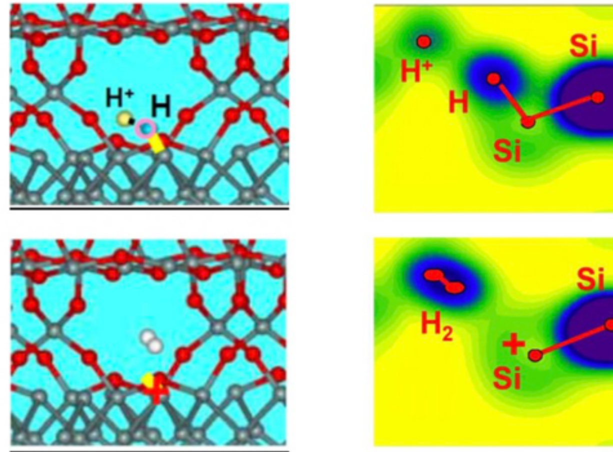

Fig. 24. Top: Energy band illustration of total ionizing dose effects [59]. Bottom: Formation dynamics of interface traps [61]. Positively charged proton transport to the semiconductor/insulator interface is crucial in the formation of interface traps.

et. al determined that P_b centers occur along silicon-silicon dioxide interfaces regardless of the crystalline orientation of the underlying silicon [64].

The charge state of interface and border traps depends on the local electrostatic potential. The relative position of the Fermi level results in different occupancy of the trap energy levels. In Fig. 25 the charge states of interface defects are illustrated for two different electrostatic

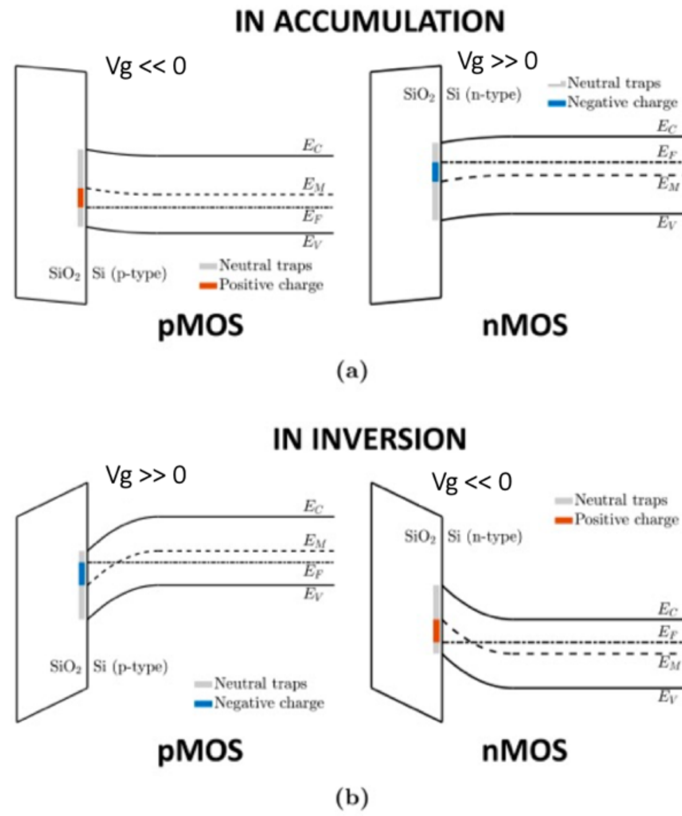

Fig. 25. MOS energy band diagram in accumulation (top) and inversion (bottom). The occupation, and charge state, of trap levels depend on the local electrostatic potential.

conditions, accumulation and inversion for both n-type and p-type silicon. For substrates of each polarity, the occupation of interface traps screens the applied bias with the opposite charge.

The most important findings for the present work are which irradiation conditions lead to significant interface trap formation corresponding to an increase in SRV. Measurements of SRV are presented in the following section.

II.4.1 TID conditions for increasing surface recombination

An important early finding in the research of TID effects was that if there is not a significant electric field across the oxide many of the electron-hole pairs that are created during irradiation

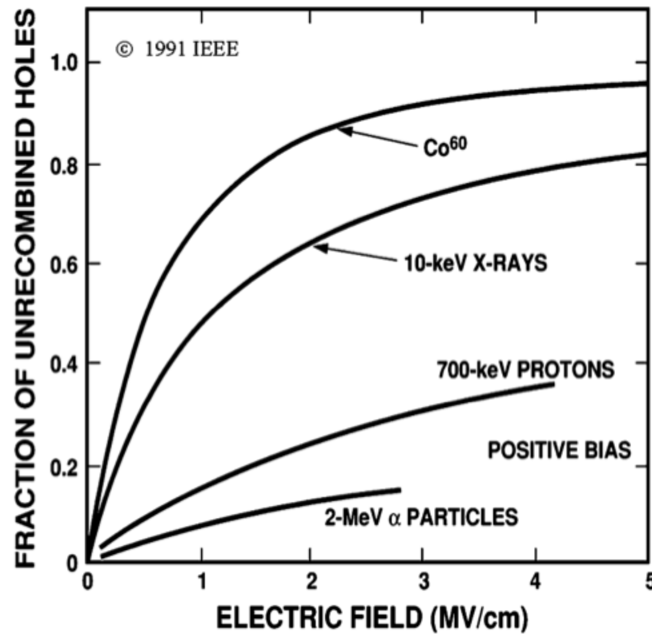

Fig. 26. The effect of electric field on recombining electron-hole pairs in SiO_2 from various ionizing radiation sources. At higher electric field strength, carriers separate more rapidly and will recombine less [58].

will recombine and will not participate in any TID effects [59], [65], [66]. This is illustrated in Fig. 26 where the fraction of unrecombined holes that can contribute to TID effects approaches a maximum with an electric field of 5 MV/cm across the oxide and rapidly diminishes at low electric fields (for perspective, the electric field at breakdown voltage is 3 MV/cm in Si and >60 MV/cm in SiO_2). Important considerations include the thickness of the oxide, the applied voltages, and any built-in voltages. As was seen in Fig. 24., the direction of the electric field is important. The electric field should be directed to push holes and positively charged protons towards the interface with the semiconductor in order to maximize the creation of interface traps. Holes can migrate to the interface from semiconductor regions as well, making any applied bias condition (+ or -) preferable to no bias.

In addition to there being an electric field present in oxides during irradiation, it is also important that the dose rate is sufficiently low [67], [68]. This is illustrated by Fig. 27 where a high

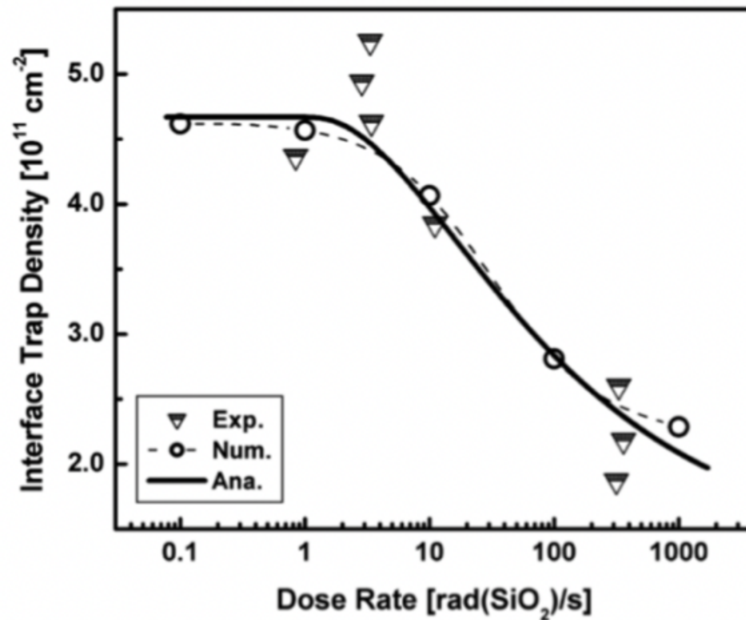

Fig. 27. The effect of dose rate on interface trap formation. At dose rates less than 10 rad(SiO_2)/s interface trap density is maximized [68].

dose rate increases the probability of carrier recombination and may lead to space charge effects [69]. Charged protons, whose transport to the interface is critical for interface trap formation, are less mobile than holes and during irradiation with a high dose rate these slower moving protons can be repelled by holes that become oxide trapped charge and border traps first. Also, the electrons moving towards the gate during irradiation can possess a sufficient quantity of negative charge that charged protons and holes become attracted away from the semiconductor interface during a high dose rate irradiation (i.e., space charge effects) complicating interface trap formation further.

Although dose rate and oxide electric field are arguably the most important irradiation conditions for TID effects, temperature during irradiation and annealing time after irradiation have also been demonstrated to be important considerations. Charged proton mobility increases with temperature. Therefore, irradiating devices at an elevated temperature can increase the density of interface traps. However, elevated temperatures also increase annealing of interface defects. A

sweet-spot between 100 - 150 °C maximizes interface traps [70]. Holes transport through the oxide by hopping through defect states near the valence band and charged protons have relatively low mobility; therefore, an annealing time after irradiation is beneficial to allow for transport of charged species [71]. Allowing for annealing after irradiation is also of practical benefit, because any unaccounted for and ongoing annealing may result in experimental measurements that are not repeatable.

In summary the following considerations can be made for performing TID irradiations with the intention of creating interface traps and manipulating SRV:

1. Apply a bias across the oxide that directs holes/protons towards the semiconductor/insulator interface;
2. Use a low dose rate;
3. Allow for time-dependent annealing and/or
4. Raise the temperature of the device during irradiation

II.5 Recombination physics

At thermal equilibrium in semiconducting materials, recombination and generation processes are balanced. Illustrated in Fig. 28 are the recombination mechanisms important for SEE: Auger and Shockley-Read-Hall (SRH) recombination. SRH recombination occurs in the presence of defects in bulk of a material or along a surface (i.e., surface recombination). Auger recombination occurs at high carrier concentrations when two electrons collide and one of them recombines with a nearby hole in the valence band. Auger recombination also occurs with hole collisions.

In Auger recombination, kinetic energy is lost by one carrier during a scattering event and it recombines across the bandgap while the other carrier gains kinetic energy and moves up to a higher energy state. Auger recombination is the inverse process of impact ionization, where a carrier scattering event generates an electron-hole pair. Auger recombination requires direct carrier-carrier collisions that occur in the presence of high carrier concentrations (e.g., along an ion track). The rate of Auger recombination is proportional to the square of the majority carrier concentration and electron and hole Auger recombination coefficients, c_n and c_p:

$$U_{Auger} = c_n n(pn - n_i^2) + c_p p(pn - n_i^2) \tag{14}$$

In SRH recombination [72], an electron in the conduction band and a hole in the valence band are both "captured" at a trap energy state within the semiconductor bandgap. The rate of recombination in the bulk of material can be derived by considering the rates of electron and hole capture and emission for specific trap energy levels and the carrier density. A total rate of

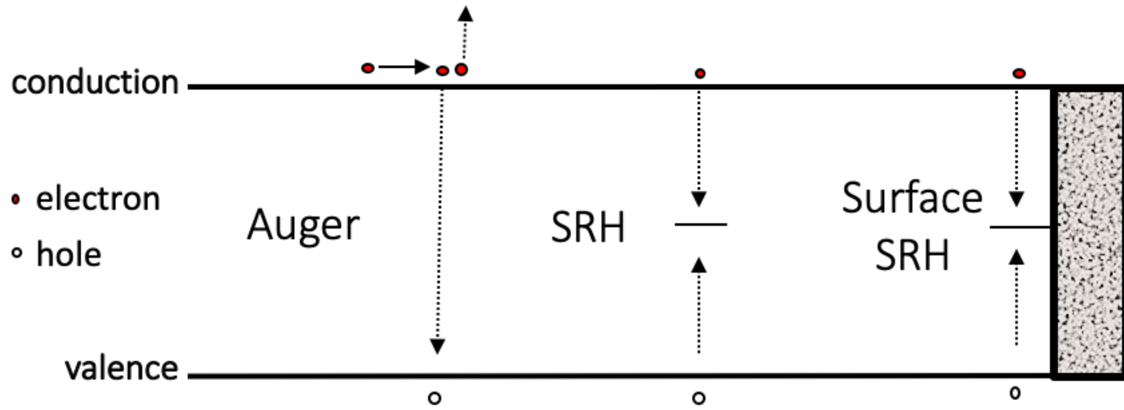

Fig. 28. Key carrier recombination processes for SEE.

recombination is found by integrating across all the trap energies levels present within the bandgap. Eq. 15 describes the bulk rate of SRH recombination due to a single trap level, U_{SRH}:

$$U_{SRH} = \frac{N_T v_{th} \sigma_n \sigma_p (np - n_i^2)}{\sigma_n \left(n + n_i \exp\left(\frac{E_t - E_i}{kT}\right)\right) + \sigma_p \left(p + n_i \exp\left(\frac{E_i - E_t}{kT}\right)\right)} \quad (15)$$

where n and p are the electron and hole concentrations, n_i is the intrinsic carrier concentration, σ_n and σ_p are the electron and hole capture cross-sections, N_T is the concentration of recombination centers with trap energy level E_t, v_{th} is the carrier thermal velocity, and kT is the thermal energy. Electron and hole capture cross-sections are commonly determined from experimental measurements. At equilibrium, $np = n_i^2$ and the generation and recombination processes are balanced. If there are excess carriers ($np > n_i^2$) net recombination will occur, while if there is a deficiency of carriers ($np < n_i^2$) net generation will occur. During a single-event, ionization creates excess electron and hole carriers. The mean amount of time an excess carrier will remain before recombining is the carrier lifetime, $\boldsymbol{\tau}$.

$$\tau = \frac{1}{N_T v_{th} \sigma} \tag{16}$$

Understanding SRH recombination is especially important for the operation of minority carrier devices, like bipolar junction transistors. Displacement damage can create additional defects in bipolar junction transistors (BJTs) that act as recombination centers and can reduce the carrier lifetime. In some BJTs, lifetime degradation is a linear process that it provides a reliable measurement of particle flux [18], [73]–[75].

Recombination along surfaces has been important since the invention of the MOSFET. Before the development of thermally grown oxides, high defect concentrations along oxide interfaces limited the performance of MOSFETs significantly due to scattering and surface recombination in the channel. Other oxides, such as the isolation along laterally conducting bipolar transistors have also been negatively impacted by surface recombination, including surface recombination increases due to TID [76]–[78]. Solar cell design relies on interface engineering to reduce surface recombination and maximize efficiency [79]–[81]. These previous circumstances where surface recombination has played an important role all occur with steady state conditions; this dissertation presents new fast transient effects of surface recombination.

The theory of surface recombination at semiconductor/insulator interfaces was established by Fitzgerald and Grove [82] based on Shockley-Read-Hall recombination. The detailed equation for determining the rate of generation or recombination along an interface based on the number of interface defects is:

$$U_s = \sigma_s v_{th} D_{st} \left[\int_{E_v}^{E_c} \frac{dE_{st}}{p_s + n_s + 2n_i \cosh\left(\frac{E_{st} - E_i}{kT}\right)} \right] [p_s n_s - n_i^2] \tag{17}$$

U_s is the rate of surface recombination or generation per unit area, σ_s is the carrier capture cross-section, v_{th} is the carrier thermal velocity, E_c is the conduction band energy, E_v is the valence band energy, E_{st} is the energy of the surface trap, p_s and n_s are the hole and electron concentrations at the interface. Analogous to carrier lifetime, SRV is directly related to the density of interface defects:

$$s = N_{st} v_{th} \sigma \tag{18}$$

here N_{st} is the areal density of interface traps, and $\boldsymbol{\sigma}$ is the trap capture cross-section. Trap states that participate in surface recombination can be distributed over a thickness of several atomic layers but for simplicity they are assumed to be located directly at the surface. The efficacy of any given recombination center depends on its energy level.

In Fig. 29, surface recombination as a function of interface trap energy level is shown. The rate of surface recombination is maximized when equal concentrations of electrons and holes are present and when defects possess energy levels near the middle of the band gap. P_b centers created during ionizing dose irradiation as discussed in Section II.4 have an energy level near the middle of the silicon band gap.

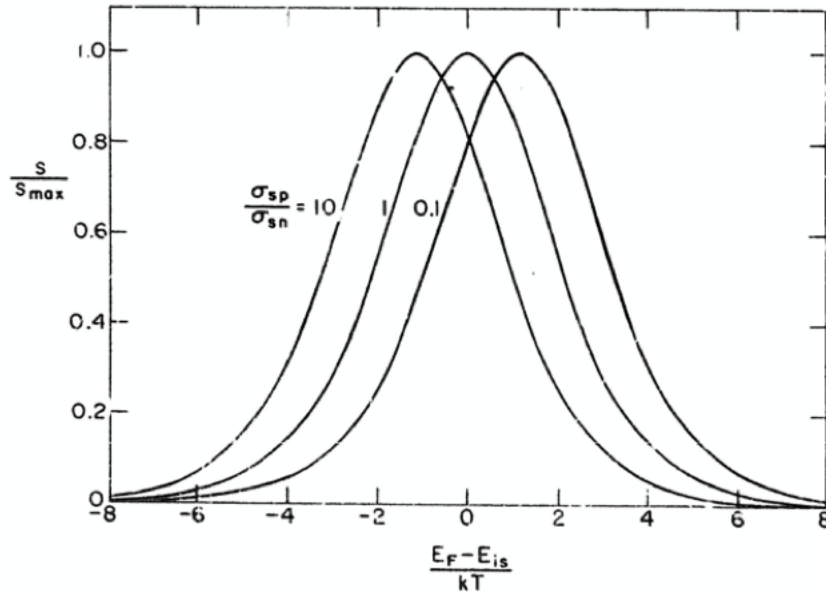

Fig. 29. Relative surface recombination velocity as a function of interface state energy for different hole/electron capture ratios. The most effective recombination level can shift toward the conduction band or valence band depending on whether the electron or hole capture cross-section is greater.

The compact version of Grove's surface recombination equation for a single defect energy level that is used in FEM simulations is:

$$U_s = \frac{n_s p_s - n_i^2}{(n_s + n_1) + (p_s + p_1)} s_0 \tag{19}$$

where,

$$n_1 = n_i \exp\left(\frac{E_{st}}{kT}\right) \; and \; p_1 = n_i \exp\left(\frac{-E_{st}}{kT}\right)$$

Ionizing dose experiments used in Chapter V experiments produce P_b interface defects with an energy level near the middle of band gap that increase surface recombination. Therefore, we can assume a trap energy level at midgap for radiation-induced defects. The quality of semiconductor/insulator interfaces, and the surface recombination that occurs along them, can vary

with device fabrication technique. Annealing and defect passivation procedures are commonly used to reduce surface recombination and improve interface quality. Understanding the conditions that lead to interfaces with different SRV is important to drawing conclusions later in this dissertation.

II.5.1 Surface recombination velocity measurements

Imangoli *et al.* published surface recombination velocities for a variety of semiconductor-insulator interfaces [83]. They measured the SRV of thermally-grown and chemically-etched Si/SiO_2 gate oxide interfaces using a large ac signal conductance technique, before and after annealing steps. Small signal conductance techniques have traditionally been used to interrogate individual interface defect energy levels.

The large signal technique used by Imangholi engages the ensemble behavior of all the defect energy levels across the bandgap for extracting a total SRV. It is important to consider the ensemble behavior because defect energy levels can be correlated. Correlations occur because the occupation of one trap energy level is influenced by others. Large and small signal techniques are shown in Fig. 30. Imangholi's measurements indicate values as low as 1 cm/s and as high as 10^3 cm/s for gate oxide interfaces. In Imangholi measurements, as well as early measurements by Snow, the SRV was observed increasing after exposure to ionizing radiation [21]. Gate oxide interfaces are accessible by direct electrical measurements while other interfaces, including isolation used in integrated circuits, require less direct measurement techniques.

Baek et. al measured the SRV of bare silicon wafers using photoluminescence and optical reflection measurements [84]. Their measurements yielded values as high as 5×10^4 cm/s for untreated silicon wafer surfaces. Cuevas measured surface recombination along silicon wafer

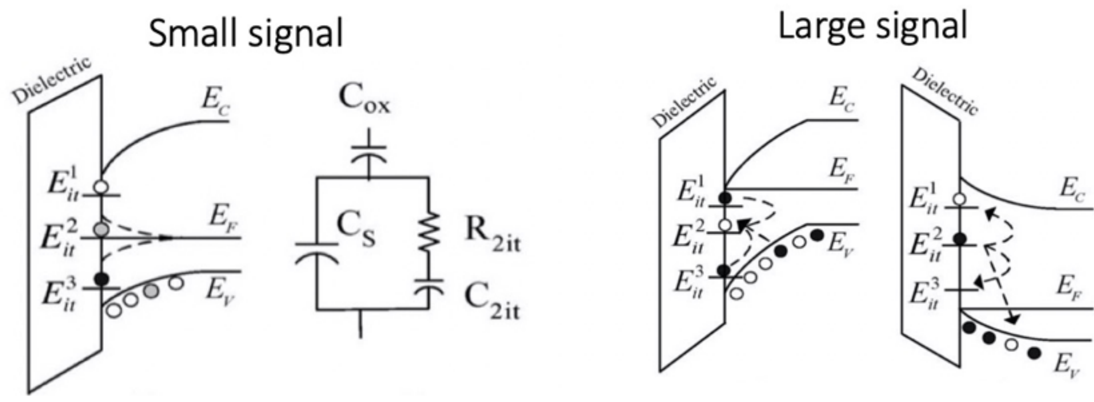

Fig. 30. Small and large signal AC conductance techniques for investigating interface defects [82]. In small signal measurements, individual defects can be probed; while in large signal measurements the effect of all defects is assessed simultaneously. The large signal technique is useful for measuring the total SRV.

surfaces using photoconductance measurements as a function of doping and passivation [85]. They found the SRV of passivated surfaces increased linearly with doping greater than 10^{18} per cm^3 from 10^2 to 5 x 10^4 cm/s. Cueva measured the un-passivated SRV to be independent of doping at a value of 2 x 10^5 cm/s. For a metal-coated silicon surface, Cueva measured a SRV of 3 x 10^6 cm/s. Nakamura *et al.* measured the SRV of a HF-treated silicon wafer and a Separation by Implantation of Oxygen (SIMOX) buried oxide interface using a Kelvin-Surface Photovoltage technique [86]. They measured 3×10^4 cm/s as the SRV for a buried oxide interface. Depending on manufacturing procedure buried oxides can have different surface recombination velocities. The Smart-Cut technique can produce high quality thermally-grown buried oxide interfaces [87], [88]. A hard limit for SRV along a silicon surface is the thermal velocity of carriers (~10^7 cm/s). The measured values presented in this section are compared with new measurements of an irradiated buried oxide interface in Chapter VI.

CHAPTER III

RADIATION EFFECTS IN SOI

SOI technology is utilized in this dissertation to study the role of surface recombination in SEE. SOI features a thin film of silicon on top of an insulating layer of silicon dioxide that electrically isolates devices from the wafer's substrate [89]. Depending on silicon film thickness, device geometry, and doping, SOI devices can have either partially-depleted (PDSOI) or fully-depleted (FDSOI) body regions as shown in Fig. 31. The active silicon and buried oxide thickness for ultra-thin body and BOX (UTBB) FDSOI devices can be 10 nm or less [88], [90] while the technology used in this dissertation is PDSOI with silicon thickness of 250 nm and a 200 nm thick buried oxide. In addition to the oxide layer below the active silicon, devices are isolated laterally using shallow trench isolation, STI. The electrical isolation acts to restrict the thickness of sensitive volumes that can collect charge during a single-event and can reduce the occurrence of soft errors; therefore, SOI has been a popular platform for radiation-hardened circuit applications [91].

The isolation used in SOI presents several radiation effects drawbacks. Isolation can trap charge, creating leakage paths and introduce front-channel/back-channel coupling effects

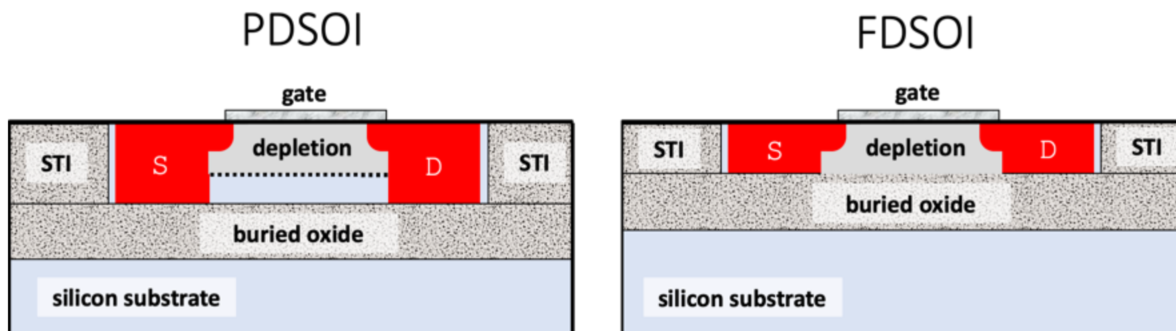

Fig. 31. Partially- and fully-depleted SOI technologies. The perimeter of the electrically sensitive semiconductor region is composed of a buried oxide layer and shallow trench isolation (STI). Red signifies n-type doping, while blue is p-type.

(especially in FDSOI). Also, the isolated device body can float, leading to parasitic bipolar effects

(especially in PDSOI). The following sections illustrate these drawbacks and mitigation techniques.

III.1 Leakage paths

In Fig. 32 is an SOI device with the three main leakage paths along isolation interfaces illustrated. Trapped charge in the oxides along these interfaces can create conductive channels and result in leakage currents that draw power when the device is off and can interfere with circuit functionality. Charge trapping is minimized in thin gate oxide layers, which limits the concern for front-channel leakage. However, some technologies use thick BOX and STI regions which can accumulate significant trapped charge.

In Fig. 33 back-channel leakage along the buried oxide in an SOI device is illustrated using 2D FEM. The amount of leakage current increases with trapped charge density until very little gate control remains. Back-channel and side-channel leakage are produced by trapped charge and Turowski [92] shows that gate bias conditions can influence where charge is trapped in isolation oxides. If a positive bias is applied to the gate during irradiation, trapped charges are repelled from forming near the channel and leakage currents are reduced.

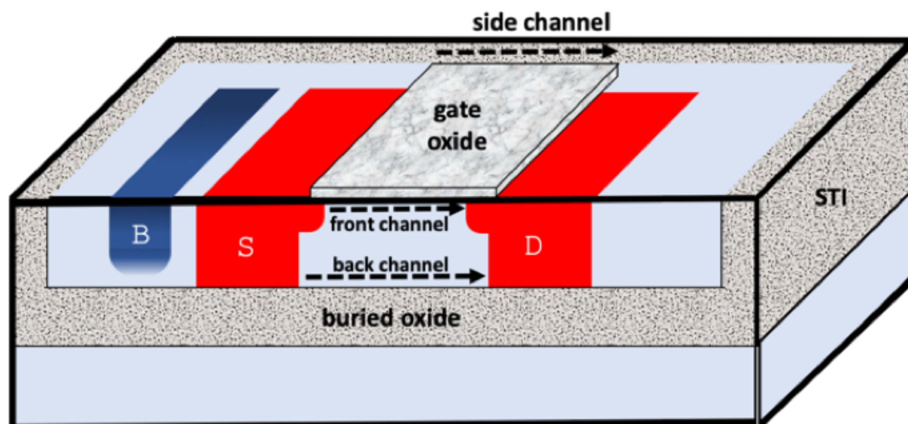

Fig. 32. Leakage paths in an SOI MOSFET.

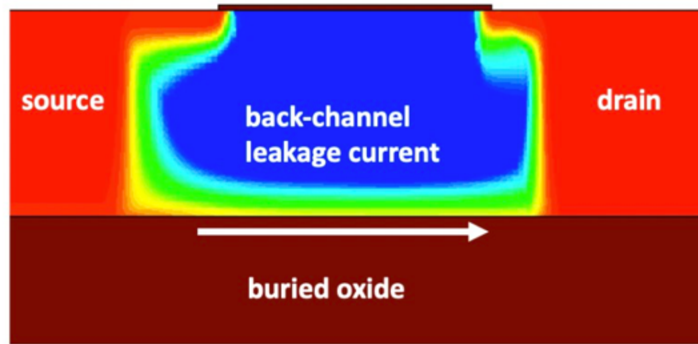

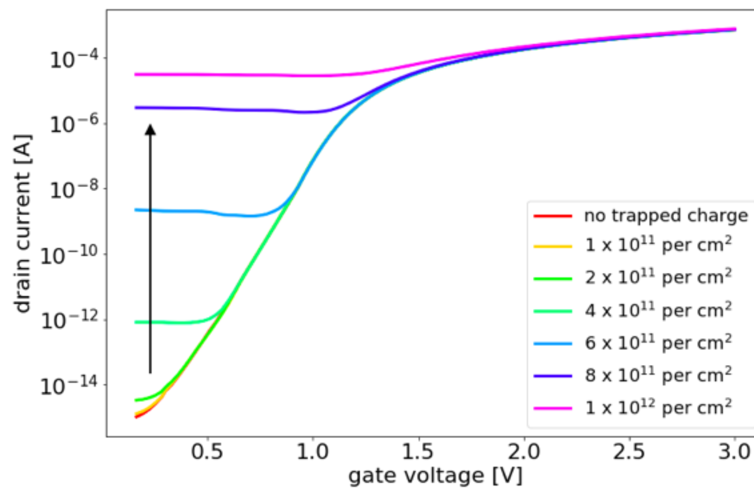

Fig. 33. Top: Trapped charge in the BOX creates a back channel for electrons between source and drain. Bottom: Off-state leakage current in an SOI device increases with trapped charge density.

III.2 Generation leakage current

SRH generation current in depleted regions is a known source of leakage in reverse biased junctions of SOI devices and can occur along depleted interfaces [93], [94]. The amount of leakage current produced is proportional to the carrier lifetime in bulk regions and the SRV along interfaces. Displacement damage in bulk regions can decrease the carrier lifetime and total ionizing dose can increase the SRV along interfaces, making this leakage current a function of radiation

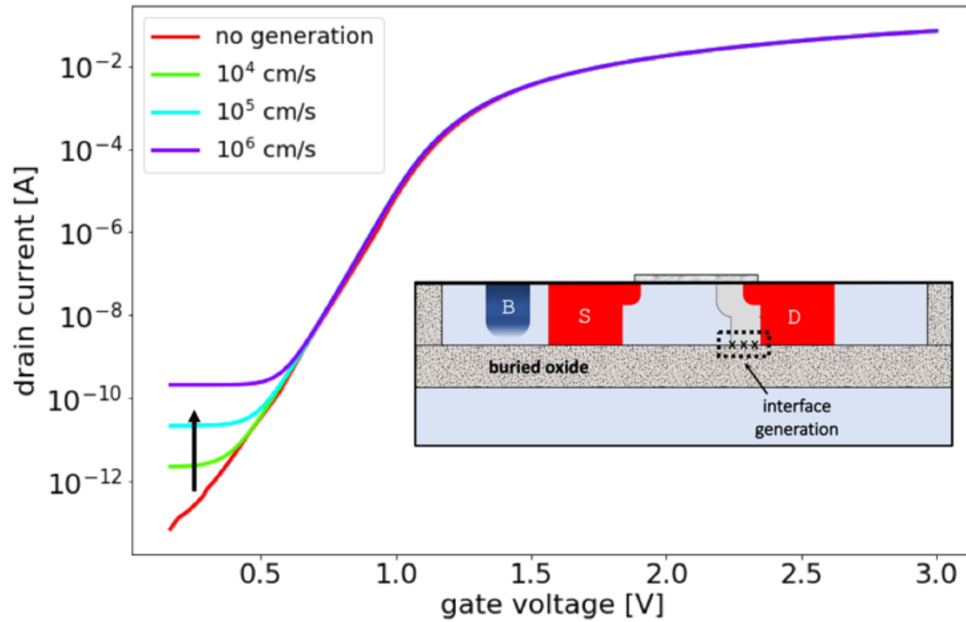

Fig. 34. Off-state generation leakage current in an SOI device. Interface generation current is produced along the buried oxide surface under the drain-body junction.

exposure. For surface generation, the generated current is proportional to the depleted surface area and therefore the drain voltage. In Fig. 34, the drain current is plotted as a function of gate voltage for different surface generation velocities. As the generation velocity increases more leakage is measured at the drain at low gate voltages. Back-channel and side-channel leakage typically produce more off-state leakage current than interface generation. Generation leakage currents are further modeled and experimentally measured in Chapters IV and V, respectively.

III.3 Floating body effects

Holes can accumulate in the body region of an SOI device after a single-event ion strike or during high frequency operation. As seen in Section II.3, the presence of an excess carrier concentration will influence the potential distribution. Floating body effects occur because accumulated holes cause the electrostatic potential in the body region of SOI devices to float

relative to ground. The elevated potential can forward bias nearby junctions and stimulate current flow. In SOI, this occurs much like in a bipolar transistor. The accumulated holes in the body mimic the positive voltage applied to the base of a bipolar transistor and current flows from source to drain (emitter to collector).

The parasitic bipolar structure in an SOI device is illustrated in the top of Fig. 35. In the bottom of Fig. 35 the potential distribution (left) and hole concentration (right) across the body of the SOI device are plotted at three times: in equilibrium before an ion strike, during an ion strike, and 85 ps after the ion strike. The holes introduced in the body region modulate the potential and forward-bias the source-body (emitter-base) junction during the ion strike, engaging the bipolar action of the structure. The charge generated during a single-event can be amplified by this bipolar

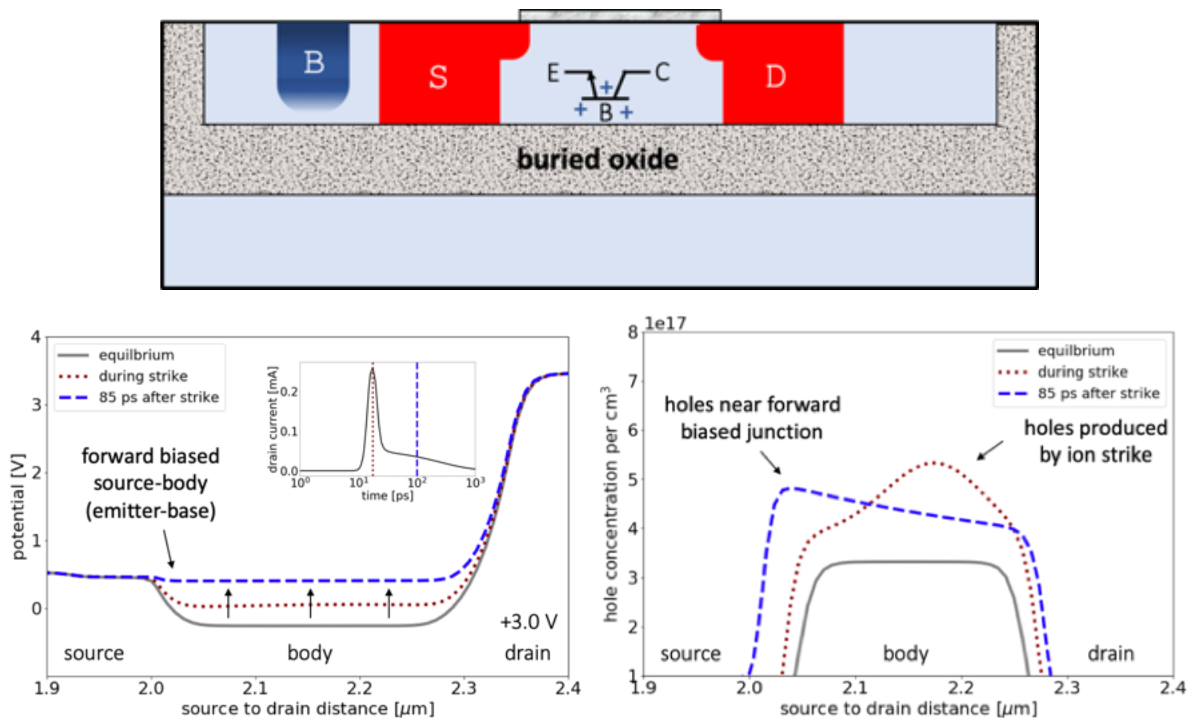

Fig. 35. Parasitic bipolar enhancement in SOI. Holes introduced in the body region forward-bias the source-body (emitter-base) junction turning on the bipolar element. The electrostatic potential (left) and hole concentration (right) are shown going from source to drain for different conditions: equilibrium, during ion strike, and 85 ps after the strike. The inset illustrates the corresponding drain transient.

structure (i.e., parasitic bipolar enhancement) [89], [95]. Capturing bipolar enhancement in SOI devices is important for quantitative modeling of SEE and is further illustrated in Section III.5.

III.4 Capacitive influence

When an ion strikes the depletion region in a capacitor, the electric field across the depletion region temporarily re-distributes according to Poisson's equation. This time-dependent variation in electric field produces displacement current that is measured at the capacitor contacts and can also contribute to charge collection in SOI MOSFETs [96], [97]. Vizkelethy performed ion beam experiments with capacitors that had different substrate doping types and concentrations [98]. Data presented in Fig. 36 show that the induced charge from an ion strike was proportional to the size of depletion region in the capacitor. The size of the depletion region was larger in more

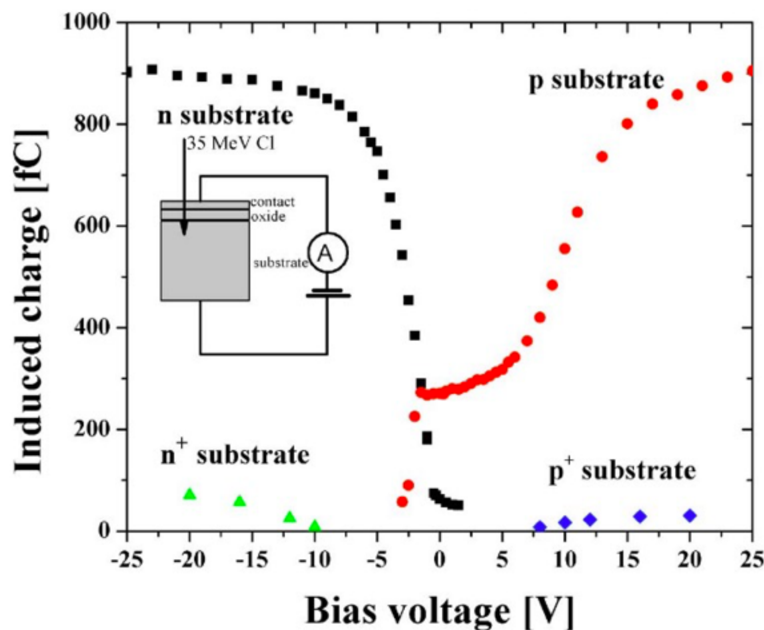

Fig. 36. Capacitor charge collection via displacement current (induced charge) during ion strikes [97]. The induced charge is a function of depletion region size (e.g., doping and applied bias).

lightly doped substrates and increases with negative applied voltage for n-type substrates and positive applied voltage for p-type substrates.

With microbeam analysis, Vizkelethy [99] made another important observation. The amount of charge collected by a capacitor was a function of strike location. In Fig. 37 the induced charge as a function of strike location is shown at the top. Near the edges of the capacitor more charge is collected. Upon further experimentation they found that the spatial difference in charge collection was due to non-uniform passivation of interface defects (Fig. 37 bottom). Near the

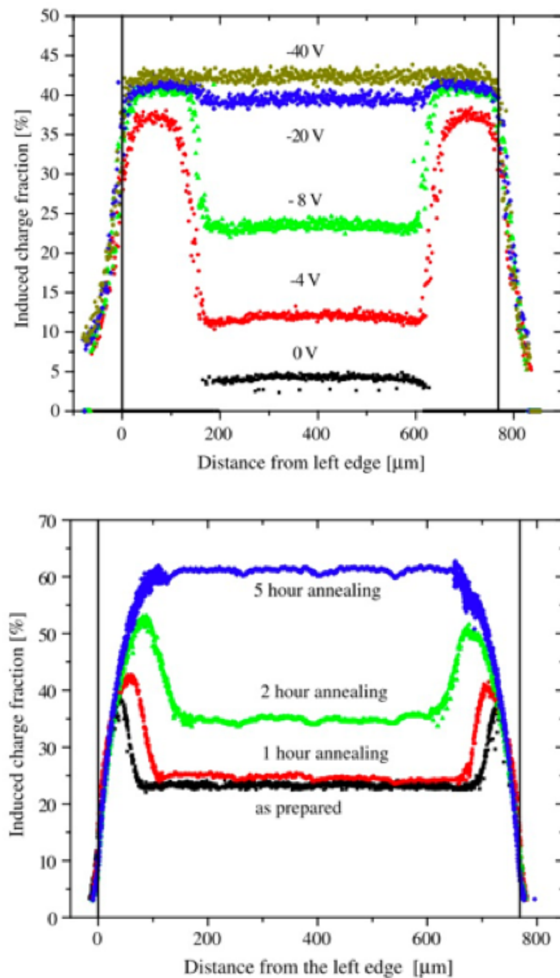

Fig. 37. Charge induced as a function of strike location across a capacitor during microbeam testing [98]. Top: The amount of charge increases with reverse bias/depletion region width. Bottom: Effective passivation near the edges results in a larger depletion region and higher charge collection. Further annealing is used to increase passivation and charge collection across device.

edges, passivated interface defects do not trap charge and the bias applied to the capacitor creates a depletion region. As discussed in Section II.4, un-passivated interface defects can be charged and their charge serves to screen the applied bias; therefore, un-passivated defects reduce the size of the depletion region and the amount of charge collected

III.5 Radiation-hardened SOI

Off-state leakage, parasitic bipolar enhancement and capacitive charge collection serve to counteract the radiation hardness benefits of SOI. However, intelligent engineering and design choices can be implemented to maintain the radiation hardness of SOI. Radiation hardening design features of the SOI technology used in the simulations and experiments of this dissertation are discussed below.

III.5.1 BUSFET features

SNL's CMOS7 3.3 V partially-depleted SOI technology is used to study surface recombination effects in this dissertation. SNL's Body-Under-Source FET, BUSFET, [100] device

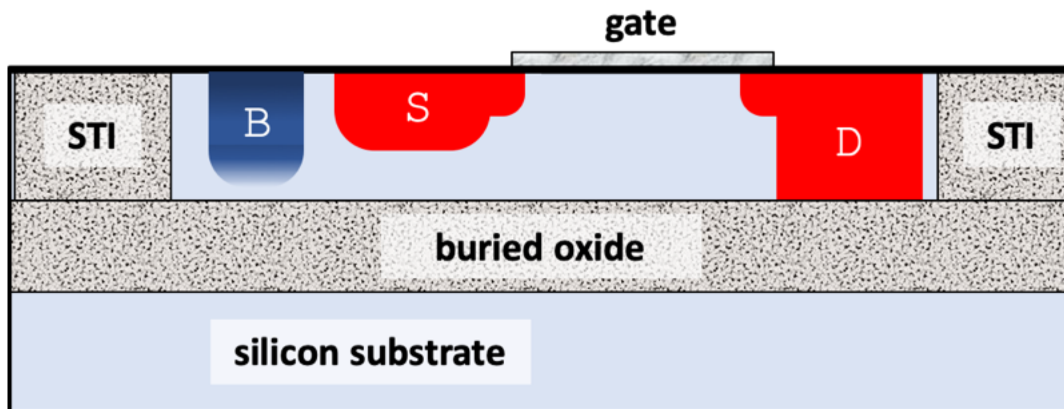

Fig. 38. BUSFET device structure with shallow source and body contact.

structure is shown in Fig. 38. It is specifically chosen for its total dose hardness, which allows for the manipulation of SRV along interfaces with high total dose irradiations without the concern of device failure. Additionally, its large feature sizes allow for meaningful spatial and temporal analysis using a targeted microbeam (e.g., more highly scaled SOI device structures produce hard to resolve charge-collection transients and sensitive volumes).

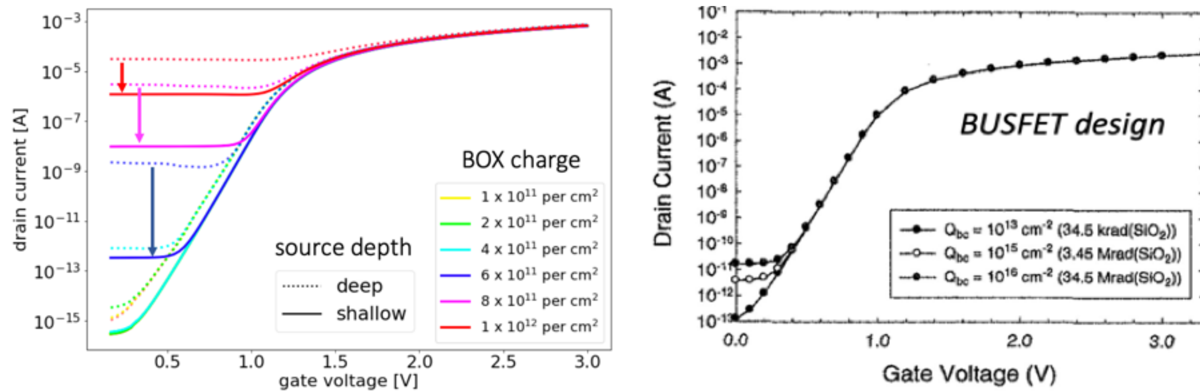

Fig. 39. Left: Back-channel leakage in SOI with a shallow or deep source. Right: Leakage in Sandia's BUSFET design [99].

The shallow source in the BUSFET serves two purposes. On the left in Fig. 39, the back-channel leakage for a deep source (shown previously in Fig. 33) is compared to the leakage with a shallow source using 2D FEM modeling. The shallow source reduces back-channel leakage by extending the length, and resistance, of the back-channel leakage path. In addition to using a shallow source, the BUSFET design, uses a retrograde body doping profile with a higher doping concentration near the back interface. The higher doping suppresses back-channel formation (Fig. 39 right).

In Fig. 40 the amount of charge collected as a function of time is compared in 2D FEM model for a shallow and deep source implant. The shallow source collects significantly less charge

by maintaining the body potential and reducing bipolar enhancement. With minority carrier lifetime decreased to 1 ns, the bipolar enhancement is reduced in the deep source structure.

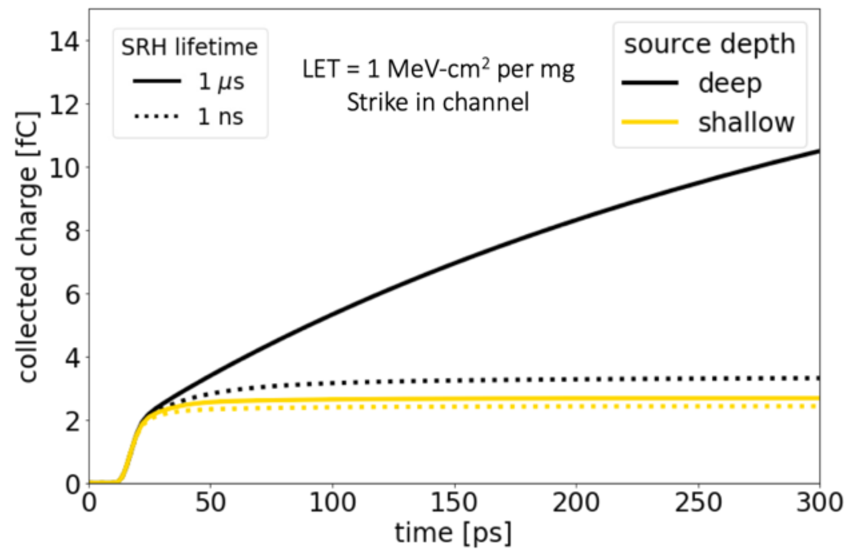

Fig. 40. Charge collection from a single event in a normal SOI MOSFET compared to the BUSFET structure. The BUSFET experiences significantly less parasitic bipolar enhancement.

The BUSFET design has a heavily doped body contact. The body contact is used to control the potential in the body region and prevent floating body effects. The body contact and shallow source allow holes to readily escape the body region and reduces parasitic bipolar enhancement. The placement of body ties directly impacts their efficacy, with closer body ties providing less resistance for maintaining the body potential [89] . To prevent capacitive charge collection, the Sandia technology uses a thick buried oxide and n-type substrate that will not form a depletion region with positive oxide trapped charge.

III.5.2 BUSFET optimization

Recent work by Black [101] has shown that charge collection modeling is useful for assessing design features that optimize SEE hardness. Model-based (top) and experimentally measured (bottom) LET vs. cross-section plots are shown in Fig. 41 for four different D-Flip Flop

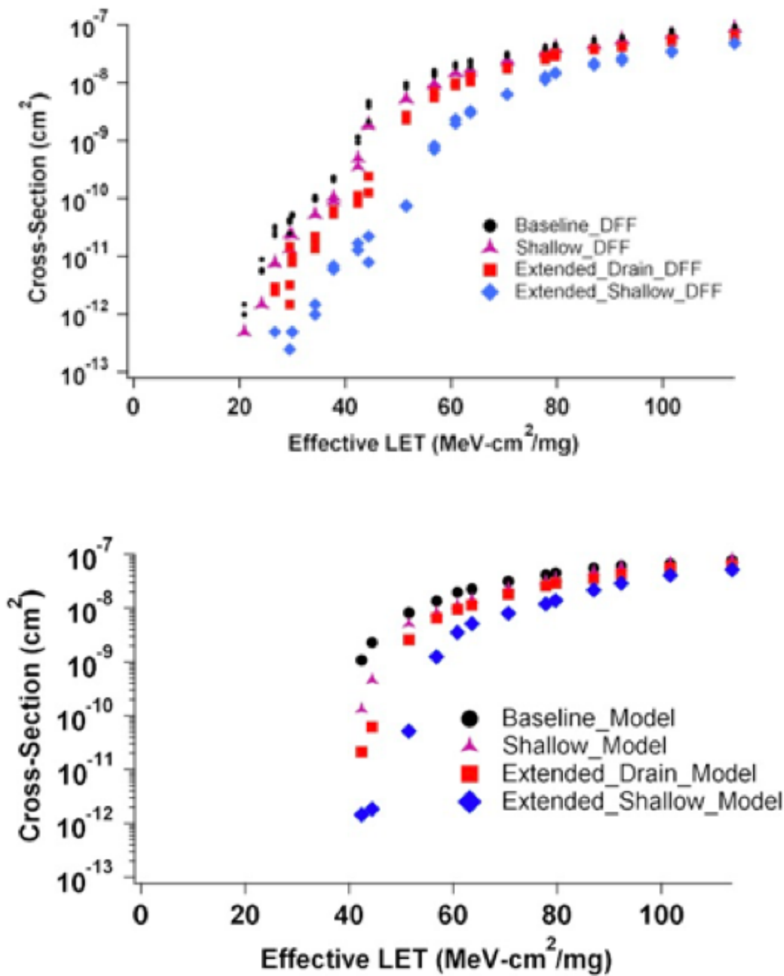

Fig. 41. Top: Experimental SEE cross-section measurements on Sandia's CMOS7 performed at the Texas A&M cyclotron. The extended body and shallow drain device design offers improved SEE tolerance. Bottom: Model predictions for error cross-section from direct ionization from high LET ions.

designs [101]. The modeled cross-sections are calculated using MRED with sensitive volumes derived from 3D TCAD charge collection modeling of the constituent transistors. The *baseline* model uses a shallow source implant and deep drain implant. The *shallow* model uses a shallow source and drain implant. The *extended* models feature a larger drain area. These design choices present a direct tradeoff. Using a shallow or extended drain implant increases the junction area and therefore the junction capacitance.

A higher capacitance junction will require a higher critical charge to induce an upset and should reduce the soft error rate [102]–[104]:

$$Q_{crit} \propto C_{node} V_{dd} \tag{20}$$

However, the shallow and extended drain designs increase the size of the sensitive volume, which potentially counteracts the increased charge necessary to create an upset. Physics-based modeling was used to show that increasing the critical charge with a shallow and extended drain optimizes the SEE hardness more than minimizing the sensitive volume for this technology. Experimental testing at the Texas A&M heavy-ion cyclotron confirmed the model predictions.

CHAPTER IV

MODELING SINGLE-EVENTS AND SURFACE RECOMBINATION

Quantitative single-event charge collection modeling requires an accurate physical description of device features and valid physics-based models. SNL provided physical specifications for SOI devices, including the BUSFET, as a part of a joint collaboration between Vanderbilt University, the Institute for Space and Defense Electronics (ISDE), and SNL. Device models were implemented using the Synopsis Sentaurus device physics suite. The finite-element models solve the device physics equations (presented in Section II.2) across a discrete mesh using averaged material properties and carrier concentrations. Doping-dependent mobility, Auger recombination, SRH recombination, and surface recombination calculations were performed using tuned Sentaurus physical models. Where high electric fields and/or carrier concentrations are present it is important to optimize the mesh to capture detailed behavior and enable calculation convergence. Therefore, mesh enhancements are introduced in the following active regions:

- At the ion strike location;
- At doping transitions;
- Along the front- and back-channel; and
- Along all oxide interfaces.

The next section discusses the Sandia device model and IV characteristics, including the impact of surface recombination. The following section discusses heavy ion charge collection simulations and the impact surface recombination has on charge collection.

IV.1 Generation leakage current in SNL SOI

As discussed in Section III.2, increasing the SRV along interfaces can lead to leakage current from generation along depleted interfaces (such as the under the drain-body junction). In Fig. 42 the generation leakage current as a function of SRV is shown for SNL's SOI BUSFET. The SNL device structure used in this simulation as well as the experimental results presented in Chapter V has a gate length of 350 nm and a gate width of 10 μm. The amount of drain leakage is

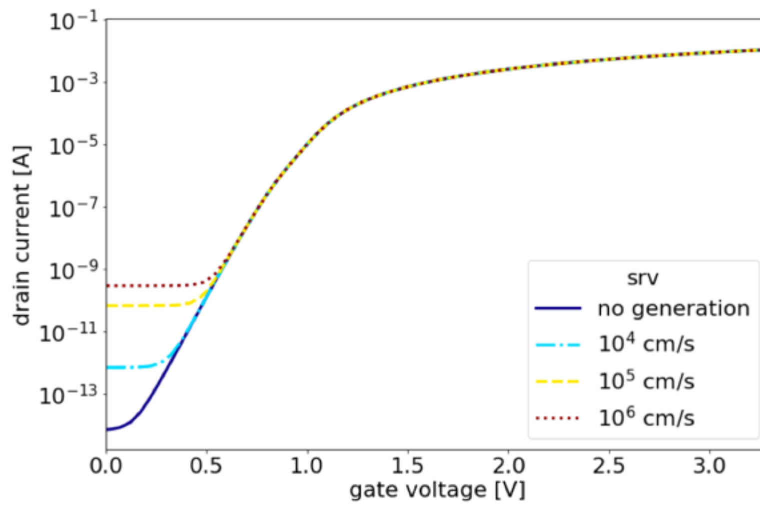

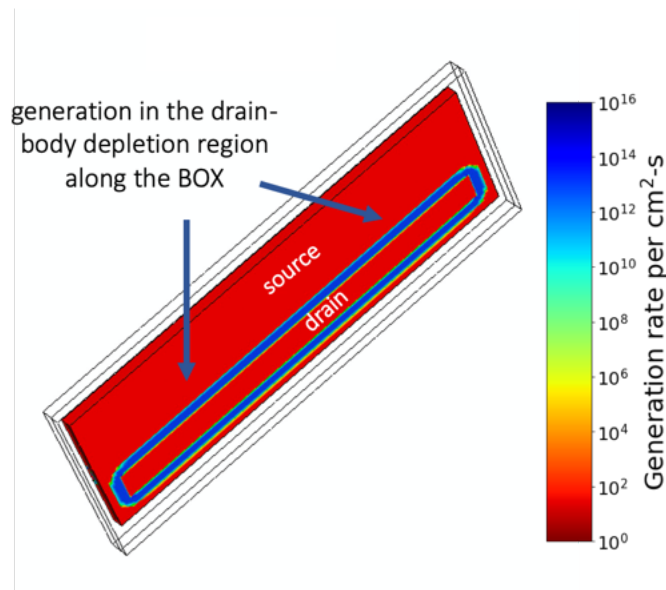

Fig. 42. Generation leakage current along buried oxide interface in Sandia SOI.

proportional to the depleted interface area (shown in the bottom of Fig. 42). Therefore, the amount of leakage current increases with gate width. The experimentally chosen device has a particularly long gate width to aid with microbeam analysis; however, this also enables measurement of generation leakage current to correlate with surface recombination.

In Fig. 43 off-state leakage current from interface generation is plotted with different drain voltages. A small increase in off-state leakage is observed with increasing drain voltage. The width of the depletion region, and therefore the surface area for generation, increases as the square root of drain voltage. This leads the increase in generation leakage current with drain voltage to be sub-linear. Based a SRV of 10^4 cm/s for buried oxide interfaces measured by Nakamura in Section II.5.1, the off-state leakage from generation along the buried oxide interface is approximately ~ 1 pA. With increasing SRV, it can approach ~1 nA. A comparison with experimental measurements is shown in Chapter V.

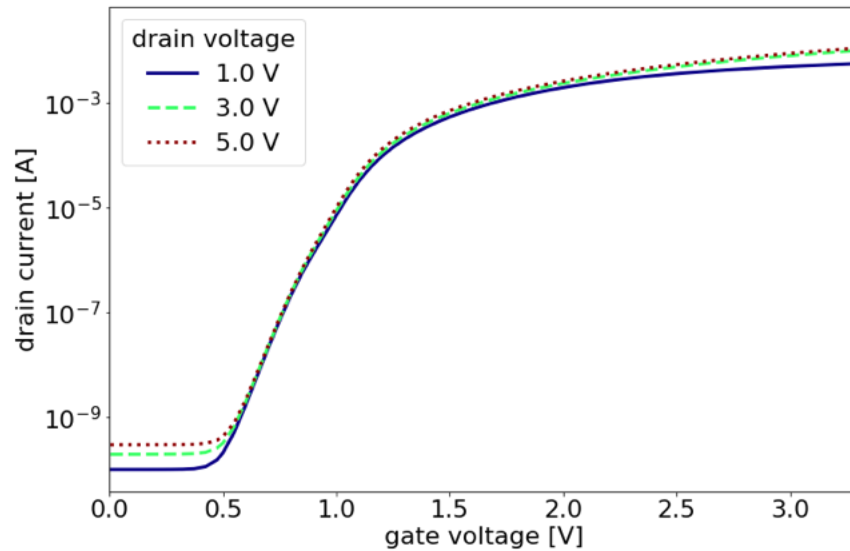

Fig. 43. Generation leakage current with different drain voltages and an SRV of 10^6 cm/s.

IV.2 Single-events in SNL SOI

Ion strikes are simulated as an excess electron and hole carrier concentration with a 50 nm Gaussian radius and with a 2 ps time constant, following the assumptions elaborated upon in Chapter II. Current is collected in the drain, source, and body contacts. Depending on strike location and ion LET, a different amount of charge is collected in each contact. In Fig. 44 the instantaneous drain current, integral charge collected in the drain, and the integral charge deposited in the device is plotted against time during an ion strike on the drain side of the channel (visualized below). Approximately 18 fC are deposited by the ion strike in the active silicon layer and 42 fC

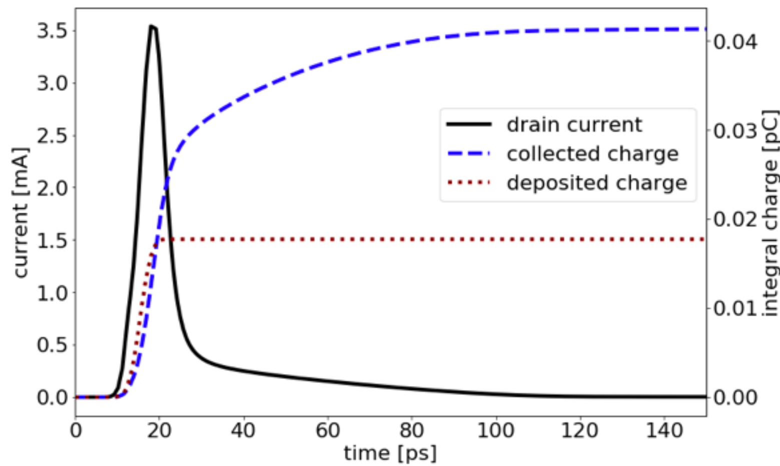

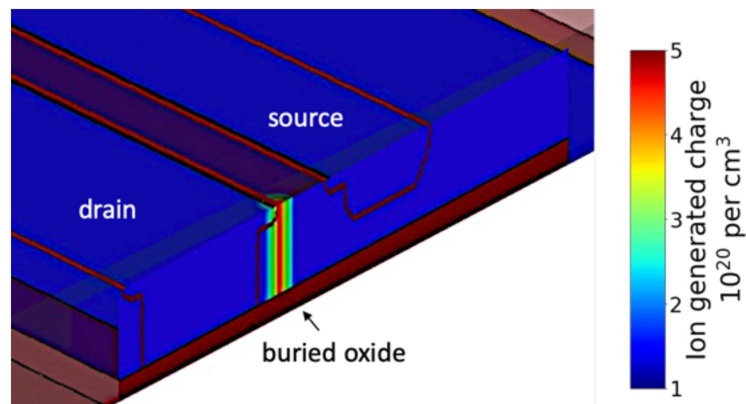

Fig. 44. Single-event ion strike in SNL SOI device channel.

are collected. More charge is collected than was deposited due to parasitic bipolar enhancement (discussed in Section III.3).

In Fig. 45 the transients and collected charge are plotted for the drain, source, and body contact for the same strike location as shown in Fig. 44. It is convention in the Synopsis tools for electron current to be positive. Current is collected semi-symmetrically between the source and drain, with a small amount of hole current (negative) being collected in the body over a longer

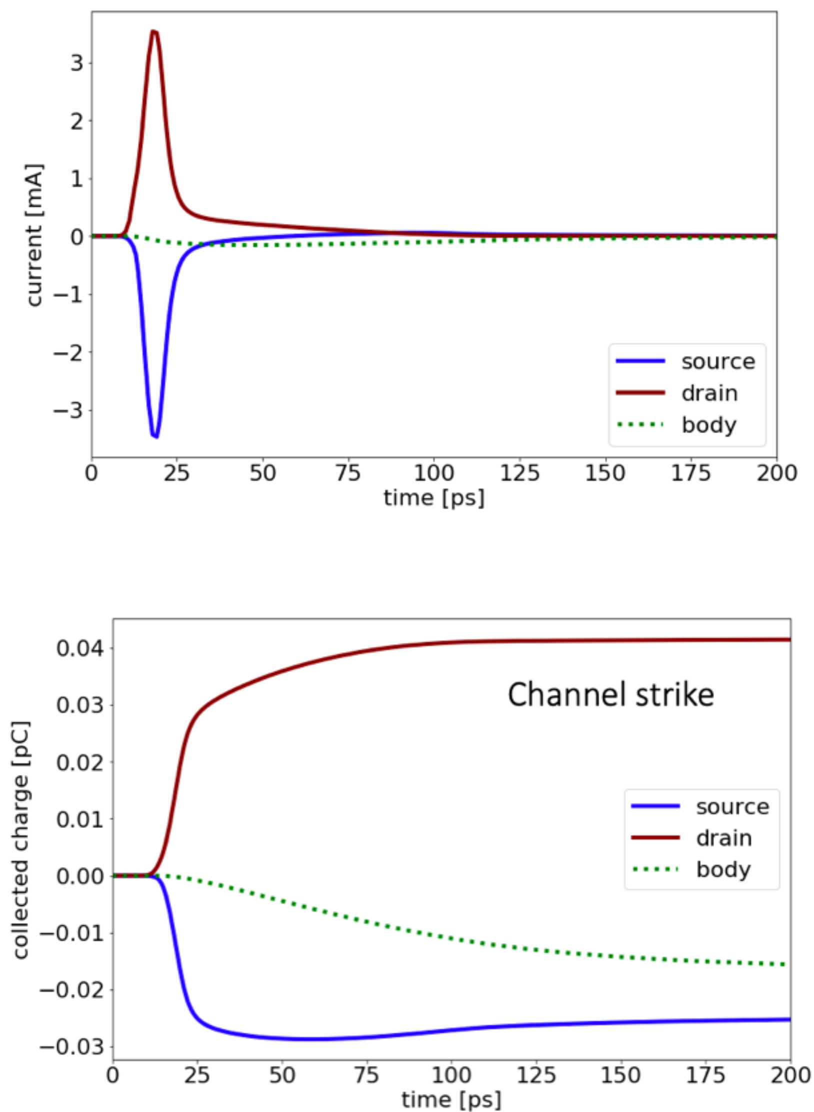

Fig. 45. Single-event transient current (top) and collected charge (bottom) in source, drain, and body contacts for a strike location in the channel.

duration. As the hole current is collected in the body, the charge collection tail in the drain falls off. This is reflective of holes creating a floating body and the drain current tail being a result of bipolar action.

The peak current in the drain as a function of strike location is shown in Fig. 46. A high peak current is measured whenever ion strikes occur within the channel, especially in the drain-body depletion region. This is consistent with charge collection via drift in the electric field of that junction.

The spatial distribution of charge collection for the drain, source, and body is shown in Fig. 47. Consistent with previous studies of SOI technology, ion strikes in the channel region collect the most charge in the drain. When charge is deposited directly in the heavily doped deep drain much less charge is collected. This is due to two main reasons: charge recombines readily in heavily doped regions and it is more difficult to modulate the potential of the nearby junction to collect charge via drift. The active body surrounds the drain and source implants in these device

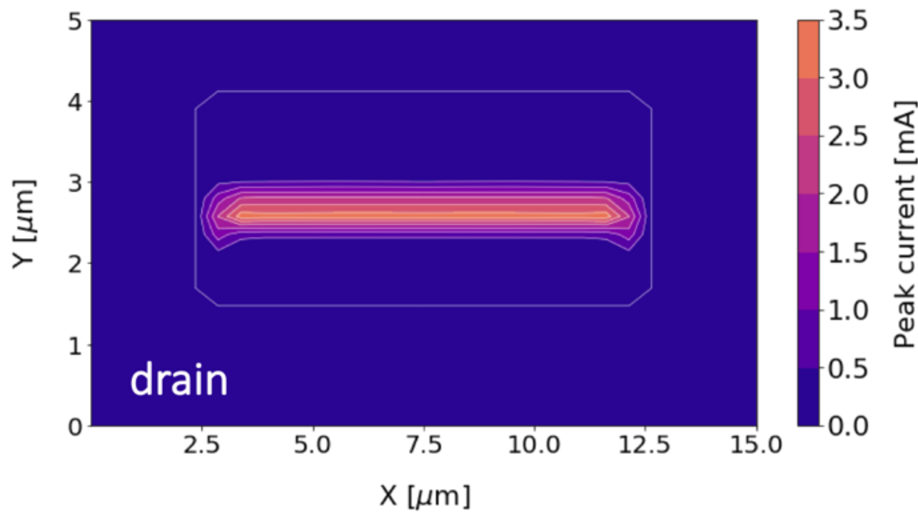

Fig. 46. Peak drain current as a function of ion strike location for an LET of 7 MeV-cm^2 per mg with +3.0 V applied to the drain. Peak current is greatest when the ion strikes the drain side of the channel.

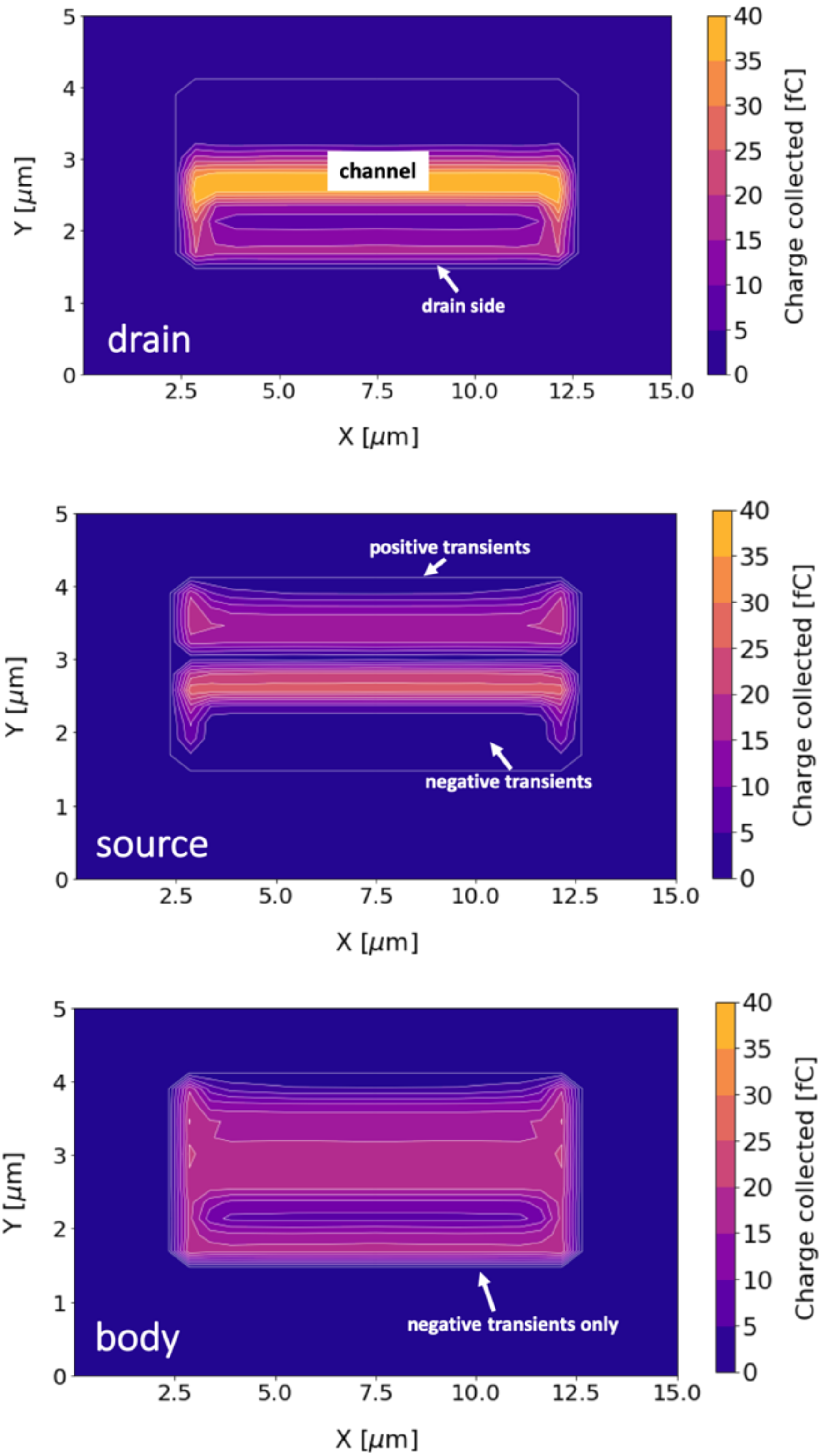

Fig. 47. Single-event charge collection in source, drain, and body contacts as a function of ion strike location for an ion with LET = 7 MeV-cm^2 per mg with +3.0 V applied to the drain.

structures and charge is collected on the left and right sides of the heavily doped drain. Transient charge collection in the source is negative for strikes in the channel and positive for strikes near the body contact. The body collects negative (hole) current across the active device with less charge being collected for strikes in the heavily doped drain or body contacts.

IV.3 Impact of surface recombination on charge collection

In Fig. 48, the excess electron distribution introduced and the corresponding rate of surface recombination is shown during an ion strike and 35 ps after the strike. It can be seen that where an

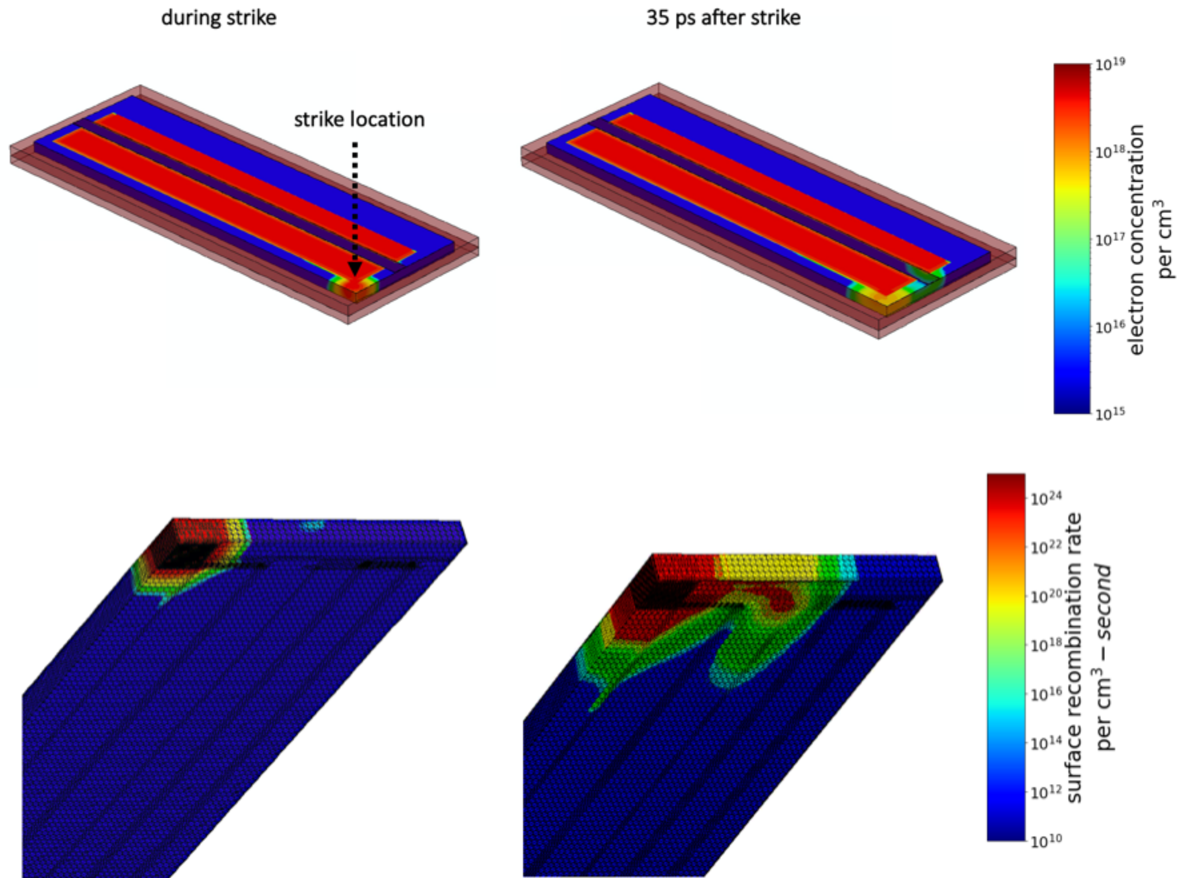

Fig. 48. Finite-element modeling of interface effects. Top: a simulated ion strike generates excess carriers (electron concentration visualized). Bottom: a bottom view shows the rate of surface recombination occurring along the STI and BOX.

excess carrier concentration is introduced to the oxide interfaces, the surface recombination rate increases. The rate of surface recombination evolves temporally and spatially as the excess carriers transport and are collected. The surface area exposed to an excess carrier concentration clearly depends on strike location. For normally incident ion strikes, surface recombination will occur along the buried oxide. Surface recombination will only occur along the STI for strike locations within 1-2 μm of the STI interface. After the ion strike, surface recombination occurs within the channel as excess minority carrier electrons are injected from the source via bipolar action.

In Fig. 49 and Fig. 50 the charge collection profile for a strike location in the channel is shown as a function of SRV. Significant reduction in charge collection occurs beginning at a SRV of 10^5 cm/s for this strike location. In Fig. 49, an ion LET of 50 MeV-cm^2 per mg is simulated while a 7 MeV-cm^2 per mg ion is simulated in Fig. 50. With higher LET ions, a greater impact of surface recombination is observed. High LET ion strikes create a strong driving force for surface recombination.

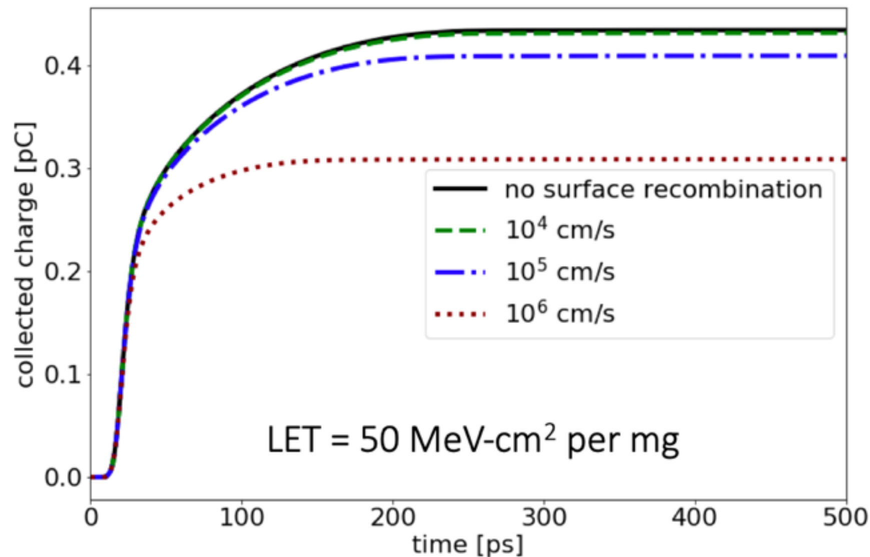

Fig. 49. Impact of surface recombination on drain charge collection for a high LET ion strike in the channel. As SRV increases (corresponding to a more defect-laden interface) the charge collected during a single event in this SOI technology decreases.

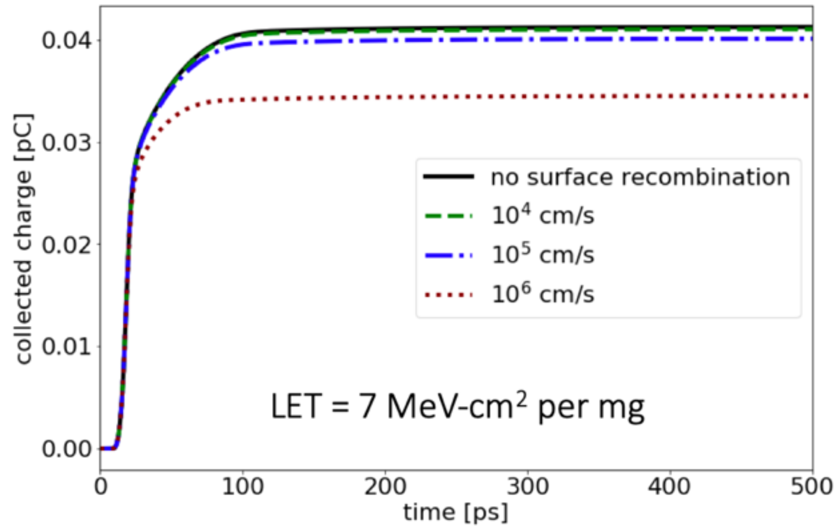

Fig. 50. Impact of surface recombination on drain charge collection for a moderate LET ion strike in the channel.

In Fig. 51 the amount of charge that recombines along the surface as a function of time is plotted. At higher LET, charge recombines along the surface for a longer period of time and a larger amount of charge is lost to recombination. Agreement can be found between the decrease

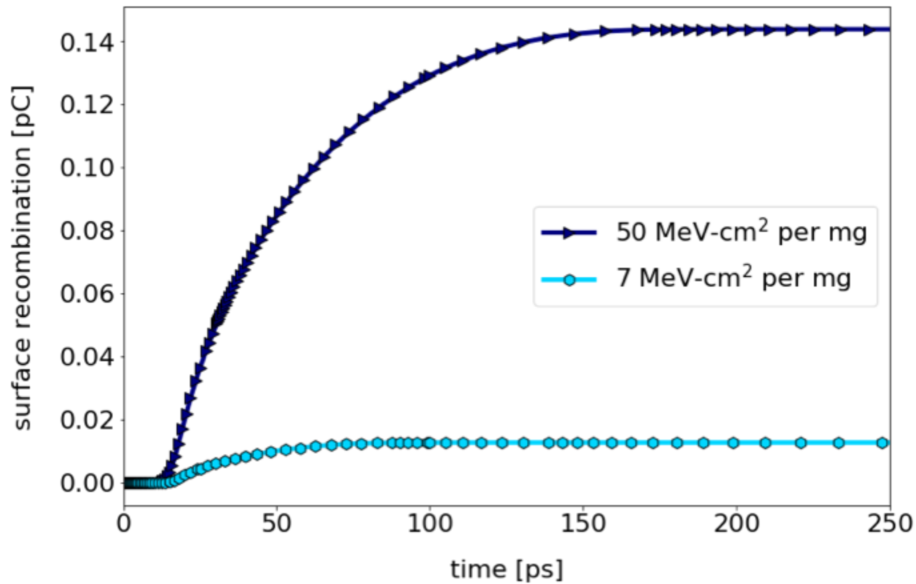

Fig. 51. Recombined charge along oxide surfaces as a function of time and ion LET. The amount of charge lost to surface recombination increases with ion LET.

in charge collection in Fig. 50 and the amount of surface recombination for 7 MeV-cm^2 per mg in Fig. 51 (~0.01 pC). Auger, bulk and surface SRH recombination are compared for a high LET ion strike in the channel in Fig. 52. Bulk SRH and Auger recombination are simulated with typical coefficients for silicon. Surface recombination has a comparable impact to bulk and Auger with SRV = 10^4 cm/s. When SRV is increased beyond 10^4 cm/s it becomes the dominant mechanism.

In Fig. 53, the amount of charge collected in the drain from an ion with LET = 7 MeV-cm^2 per mg as a function of position is plotted without surface recombination (e.g., SRV = 0 cm/s) and with SRV = 10^6 cm/s. With both interface conditions, most of the charge is collected for ion strikes within the channel. Without surface recombination, approximately 0.04 – 0.05 pC (40-50 fC) is collected when ions strike the channel. With a high SRV, the amount of charge collected when an ion strikes the channel or around the perimeter of the drain is reduced to less than 30 fC.

In Fig. 54 the amount of charge lost due to increasing surface recombination is plotted as a function of strike location. Charge lost to surface recombination is calculated as the difference

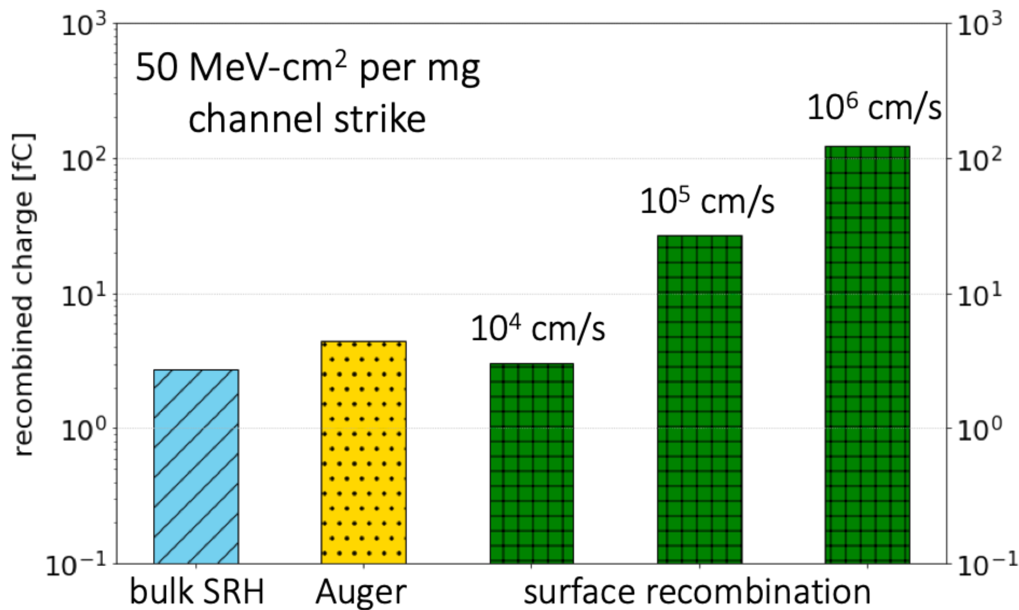

Fig. 52. Recombined charge during single-event as a function of recombination mechanism.

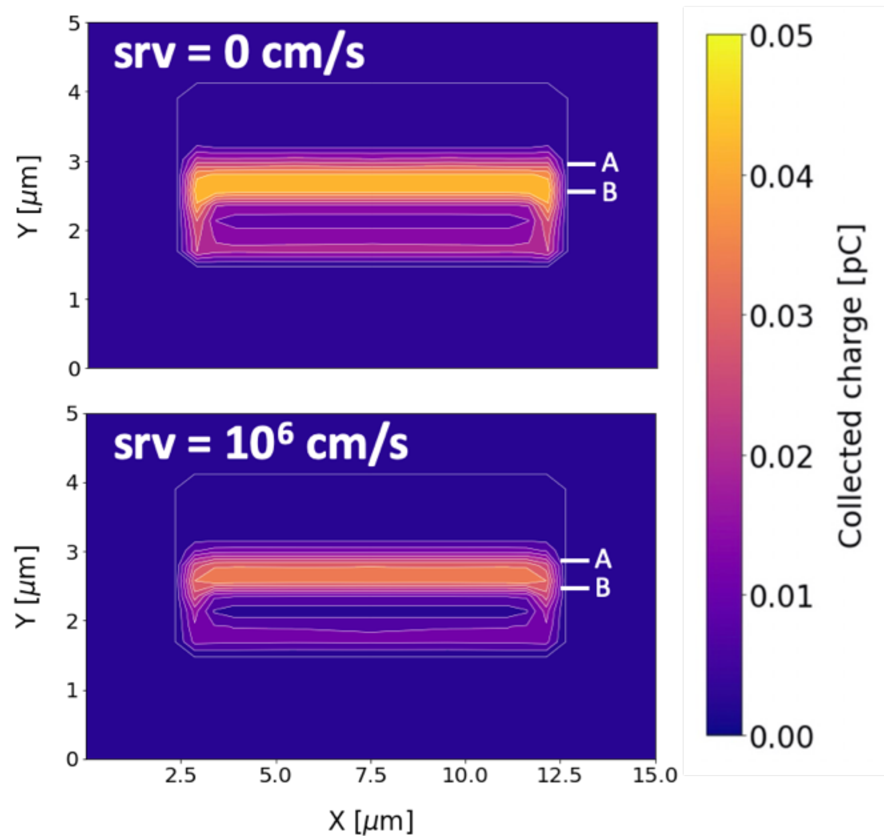

Fig. 53. Spatial charge collection distributions from finite-element simulations with no surface recombination and a high SRV.

between the charge collected without surface recombination and with a SRV of 10^6 cm/s. In the top figure, surface recombination is simulated along the buried oxide and shallow trench isolation. In the bottom, only surface recombination along the STI is included. By comparing these two charge collection maps we can deduce that the majority of charge is lost due to surface recombination along the buried oxide. Recall that in order for surface recombination to occur along the STI interface, the ion-induced excess carrier concentration must be within 1-2 μm of the interface to interact.

In Fig. 55 the amount of charge lost to surface recombination along all isolation interfaces is shown for a higher ion LET (LET = 50 MeV-cm^2 per mg). At higher LET, the spatial distribution is similar, however a greater amount of charge is lost in the corners of the drain. A higher LET

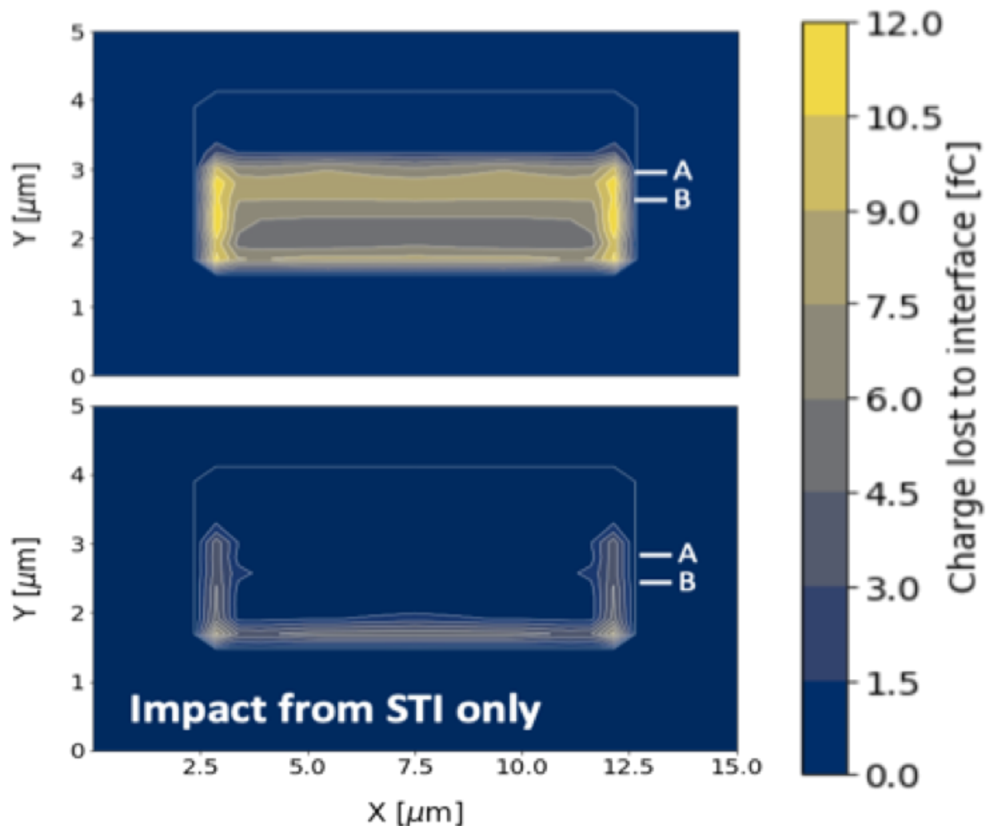

Fig. 54. Spatial distribution of charge lost to surface recombination along all isolation interfaces (top) and just along the STI (bottom).

corresponds to a higher level of carrier injection and a higher rate of surface recombination as discussed in Section II.5.

The modeling results presented in this chapter indicate that surface recombination can make an observable impact on single-event charge collection if the SRV is 10^5 cm/s or greater. Following the measurements presented in Section II.V.1, this indicates the need for experimentally increasing the SRV along the buried oxide above a starting value of <10^4 cm/s. Gamma-irradiation is used to enhance surface recombination *in-situ* in the following chapter. Modeling results are compared with the Chapter V experimental measurements to describe the role of surface recombination in SEE and infer the SRV along a degraded buried oxide interface.

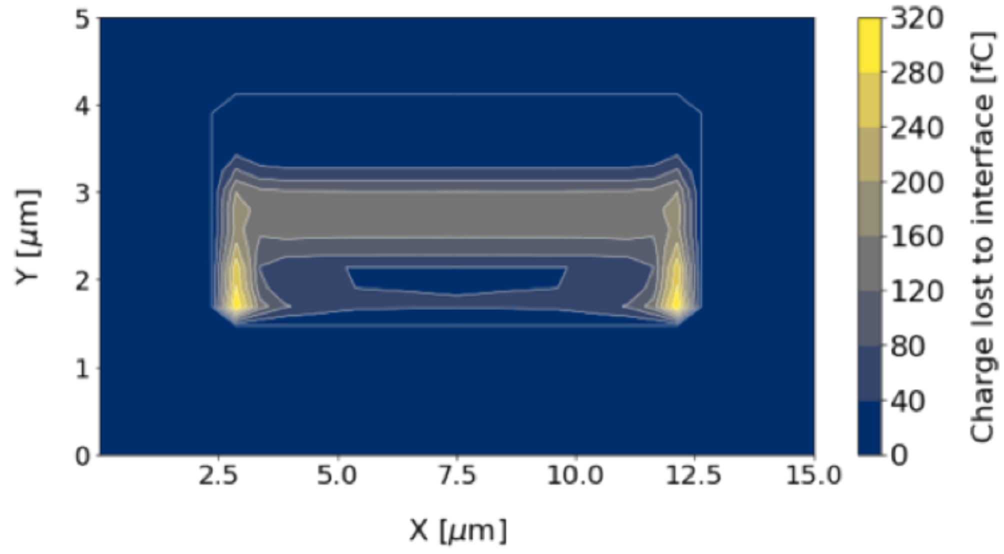

Fig. 55. Spatial distribution of charge lost to surface recombination along all isolation interfaces for an ion LET of 50 MeV-cm^2 per mg.

CHAPTER V

MICROBEAM ANALYSIS OF SURFACE RECOMBINATION

Focused ion beams ("microbeams") are a useful tool for probing sensitive electrical volumes and studying SEE [105]. Charge collected from ion strikes in individual SOI transistors are measured as function of ion strike location with 1 µm resolution. For analyzing surface recombination effects, SNL's 6 MV High Voltage Engineering (HVE) tandem accelerator microbeam is used on SNL's SOI transistors. Ion beam-induced charge collection (IBICC) and time-resolved ion beam-induced charge collection (TRIBICC) [106] experiments were performed. Fig. 56 contains a picture of a device-under-test (DUT) as mounted in the end station (on the left). On the right is a magnified view of the chip with two devices wire bonded.

A 35 MeV oxygen ion beam is used that can penetrate the overlayers (~10 µm thick SiO_2) during frontside irradiation with a range of ~23 µm in silicon. The beam has an oblong spot size

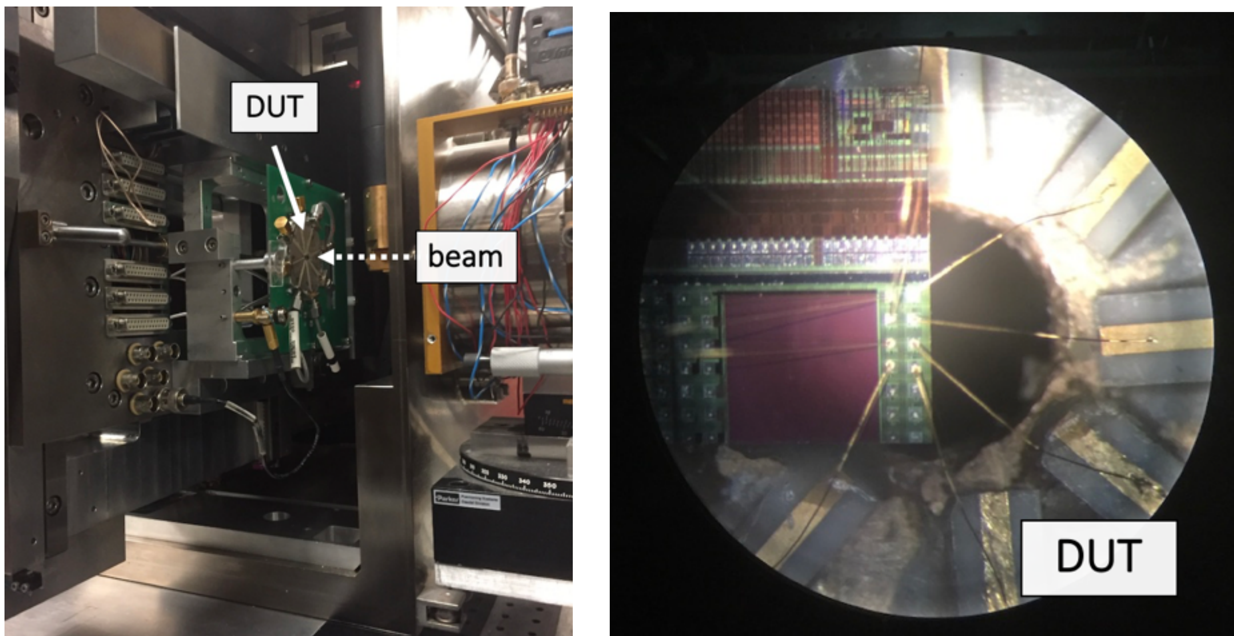

Fig. 56. Microbeam test setup. DUT is mounted in endstation (left), chip is wire bonded in package (right).

of 0.7 µm in the *x*-dimension and 1.4 µm in the *y*-dimension. The beam is electrostatically rastered

across the actively measured device to generate IBICC and TRIBICC datasets. During IBICC and TRIBICC +3 V was applied to the drain with all other terminals grounded. Collected charge was measured during IBICC by a preamplifier-spectroscopy amplifier-Analog to Digital Converter (ADC) chain. During TRIBICC, the active device terminals were monitored through 40 GHz cables on a 20 GHz Tektronics oscilloscope. Bias is supplied through a 40 GHz Picosecond Labs bias tee.

In Fig. 57, the LET vs. depth curve is shown for 35-MeV oxygen in a representative material stack, with 10 μm of SiO_2 on top of silicon. The LET across the sensitive silicon volume is between 5-7 MeV-cm^2/mg when considering straggle across a 250 nm volume (as discussed in Section II.2). The overlayers are approximated as Si but contain SiO_2 and aluminum as well. This is a reasonable approximation because the rate of energy loss in aluminum (Z_{Al}=13), SiO_2 (Z_{Si} = 14, Z_O = 8) and Si are similar.

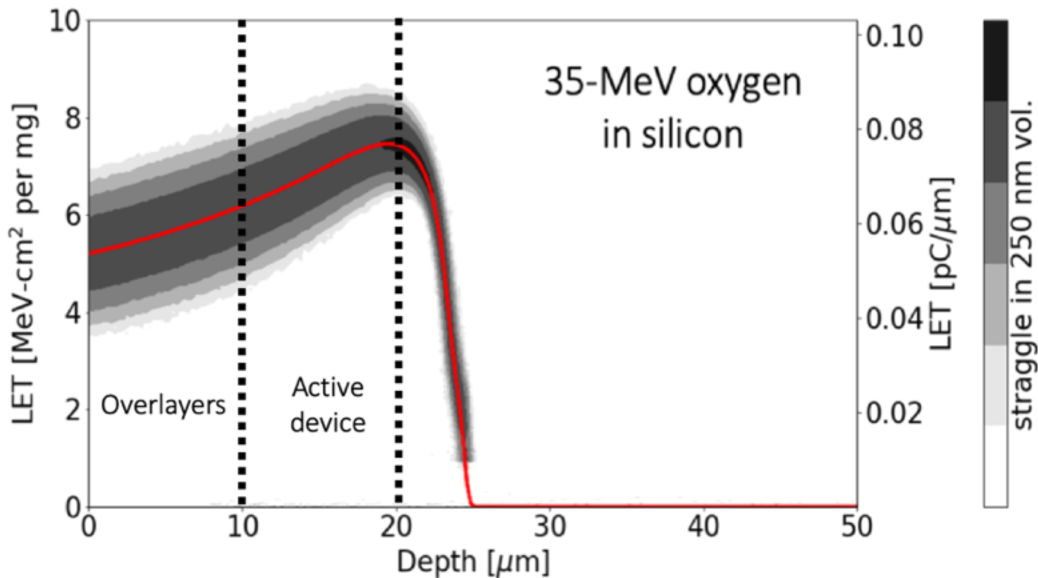

Fig. 57. LET as a function of depth for microbeam ion, 35-MeV oxygen. The beam penetrates through 10 μm of overlayer material before reaching the active device. The Z of the overlayer material is similar to that of silicon.

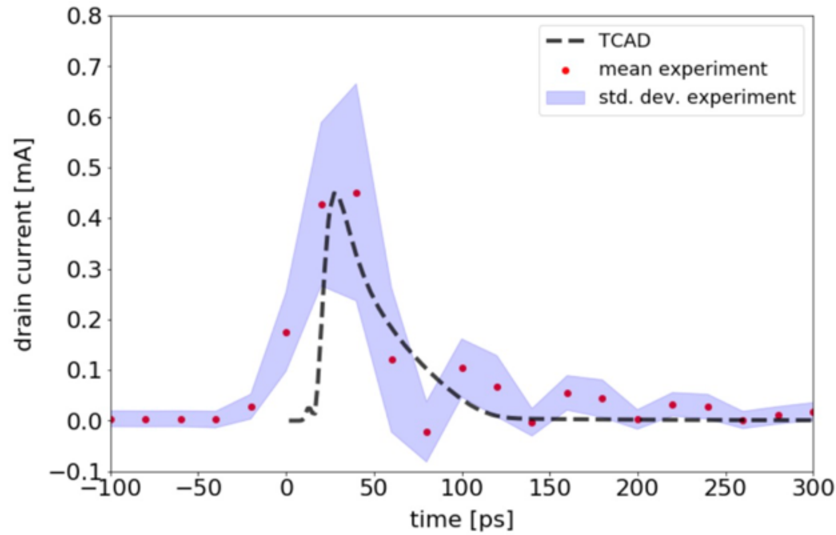

Fig. 58. Comparison of measured drain current transient with modeled transient for a strike location in the channel.

Fig. 58 shows that the charge collection profile produced by the modeling in Chapter IV agrees with the experimentally measured transients (TRIBICC) when using an ion LET of 7 MeV-cm^2 per mg. The mean drain current peak and the falling edge of the transient show excellent agreement, while the rising edge produced by the simulation is significantly faster. The slower rising edge in experiment is due to scope trigger jitter in the experimental data; the entirety of the drain transient is recorded in less than 10 samples at 25 ps each. The experimental data shown represent the mean of 1000 transients recorded for a single strike location in the channel of the active device and the shaded regions represent one standard deviation. The noise floor for the TRIBICC measurements is ~ 0.1 mA.

In Fig. 59 transients measured simultaneously in drain and body are integrated to analyze charge collection. Transient measurements are baselined to correct for any noise offset when calculating the collected charge. The drain rapidly collects ~ 30 fC of charge during this ion strike. The body collects charge slowly after the drain transient has completed. This behavior is in good

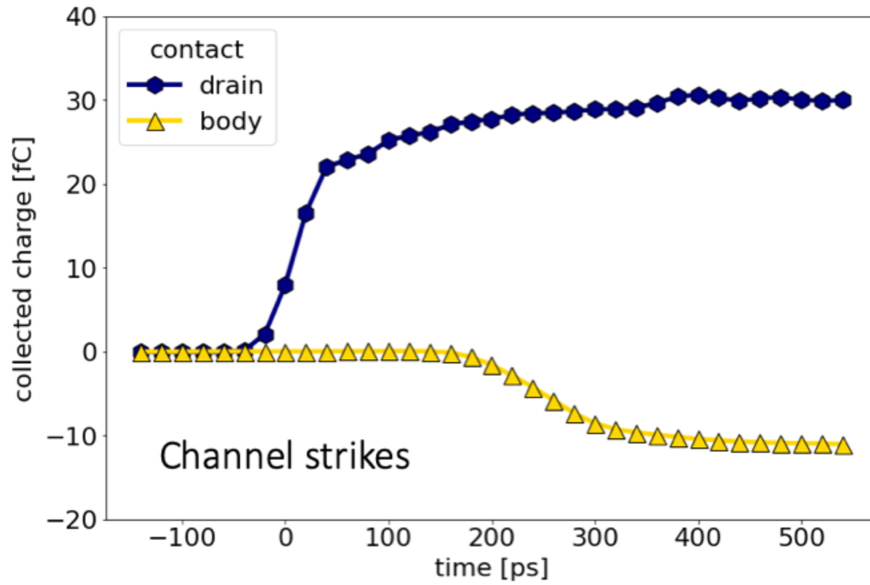

Fig. 59. Charge collection in drain and body contacts.

agreement with that observed in the modelling results in Fig. 45 although the body responds more slowly in the experiment.

In Fig. 60 IBICC maps are presented for charge collection in the drain and body. Charge collected in the drain is shown with the drain biased to +3.0 V, reflective of a normal operating condition. Recall the device used in testing has a channel width of 10 µm and a channel length of 350 nm. The highest values of charge collection are recorded for ion strikes in the channel region. The silicon body wraps around the drain and charge collection from some ion strikes in this region are observable in IBICC measurements. The drain charge collection map is in good agreement with the modeling results presented in Fig. 47.

The orientation of the device can be confirmed by measuring charge collection in the body contact with the body p^+p junction reverse-biased (-3.0 V on the body contact). The body is opposite the channel from the drain and measured high values of charge collection only for strikes

near the body contact. The agreement between the TRIBICC transient and IBICC maps provide confidence in the quantitative accuracy of the modeling results in Chapter IV.

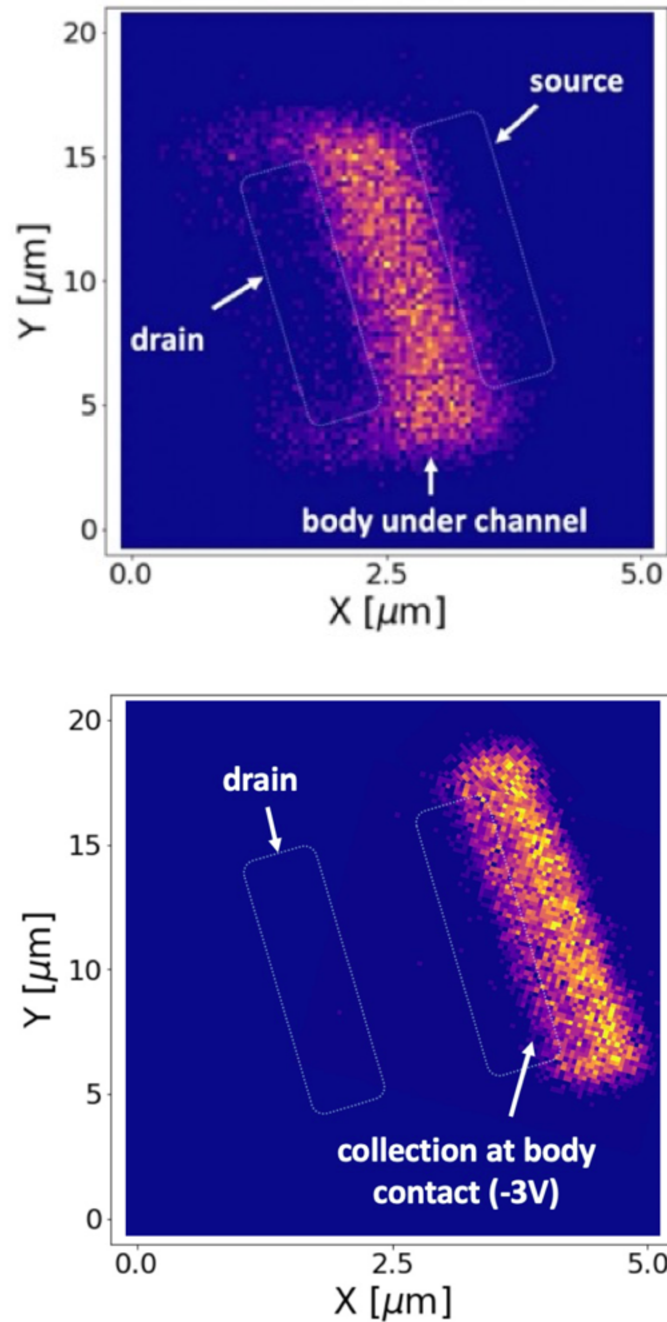

Fig. 60. Ion beam induced charge collection map of PDSOI device. On the top, charge collection is measured at the drain with a +3 V bias. In the bottom, charge collection is measured in body with a –3 V bias.

V.1 Enhanced surface recombination velocity

TID irradiations were performed after the initial microbeam measurements to increase the SRV along the buried oxide and shallow trench isolation of those devices before repeating microbeam measurements. Irradiation of the devices was performed a SNL's Gamma Irradiation Facility (GIF) in a cobalt-60 cell. Cobalt-60 is radioactive and decays via gamma emission with prominent peaks at 1.17 MeV and 1.3 MeV. During irradiation the DUT was placed at a calibrated position that receives a dose rate of 10 rad(SiO_2) per second. In Fig. 61 the cobalt cell is shown during the irradiation, with the DUT on the left side and the cobalt-60 array on the right.

To maximize charge yield and encourage the creation of interface traps along the active silicon side of the oxide, a positive bias was applied to the substrate during irradiation with all other terminals grounded. In Fig. 62 the experimental package is shown with the backside substrate contact on the left and on the right is a device illustration with the terminal biases shown. The bias of +1 V on the substrate corresponds to an electric field in the oxide of approximately 0.05 MV/cm

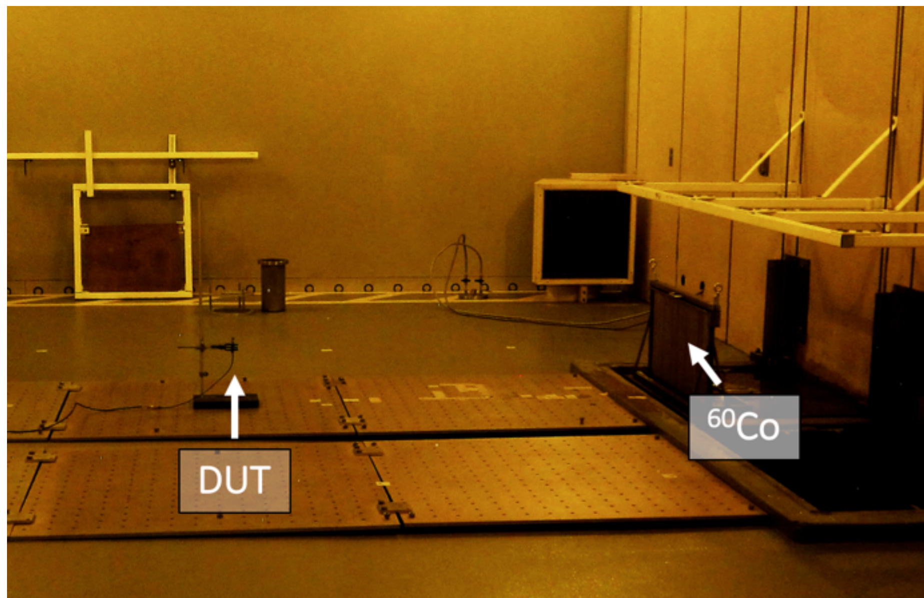

Fig. 61. Gamma-irradiation experimental setup at the SNL GIF.

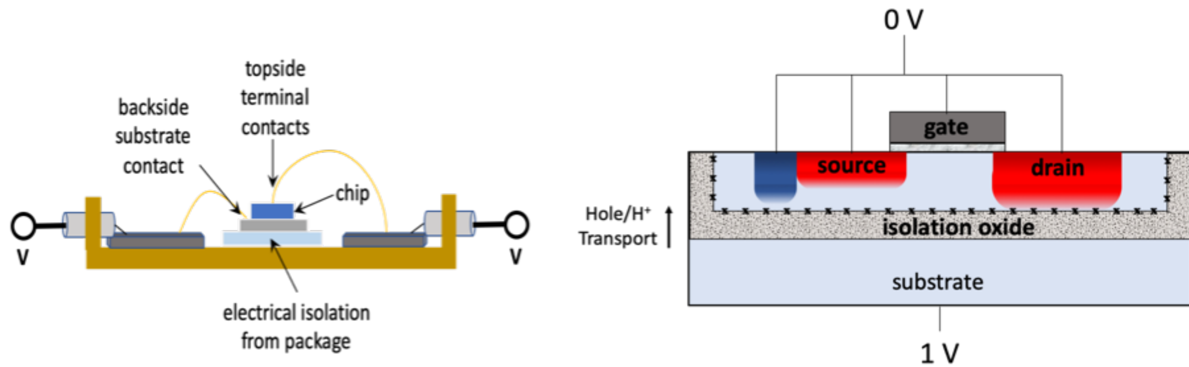

Fig. 62. Experimental high-speed device packaging with substrate contact. An electric field is created across the isolation oxide during irradiation with an applied substrate bias.

during irradiation. The devices were annealed at room temperature for 48 hours after irradiation [107].

The devices were irradiated to 1 Mrad(SiO_2). At this dose level 1 nA of off-state leakage current was produced. TID irradiation creates interface defects as well as oxide trapped charge [60], [108]–[110]. Interface defects increase the surface recombination/generation velocity, while oxide trapped charge can increase the conductivity of leakage paths. As discussed in Chapter II and III, off-state leakage can be attributed to either interface generation in junction depletion regions or back-channel/side-channel leakage paths. In Fig. 63 the transfer characteristic of the device before and after irradiation is compared with modeling results with and without surface generation. The amount of leakage measured after irradiation is consistent with a surface generation velocity of 10^6 cm/s. Leakage from trapped charge is not expected in the BUSFET structure because it is specifically designed to suppress leakage paths (Section III.5). To confirm the electrostatic influence of oxide trapped charge does not create significant off-state leakage, a substrate bias sweep up to +10 V was performed (bottom inset of Fig. 63) and did not result in any

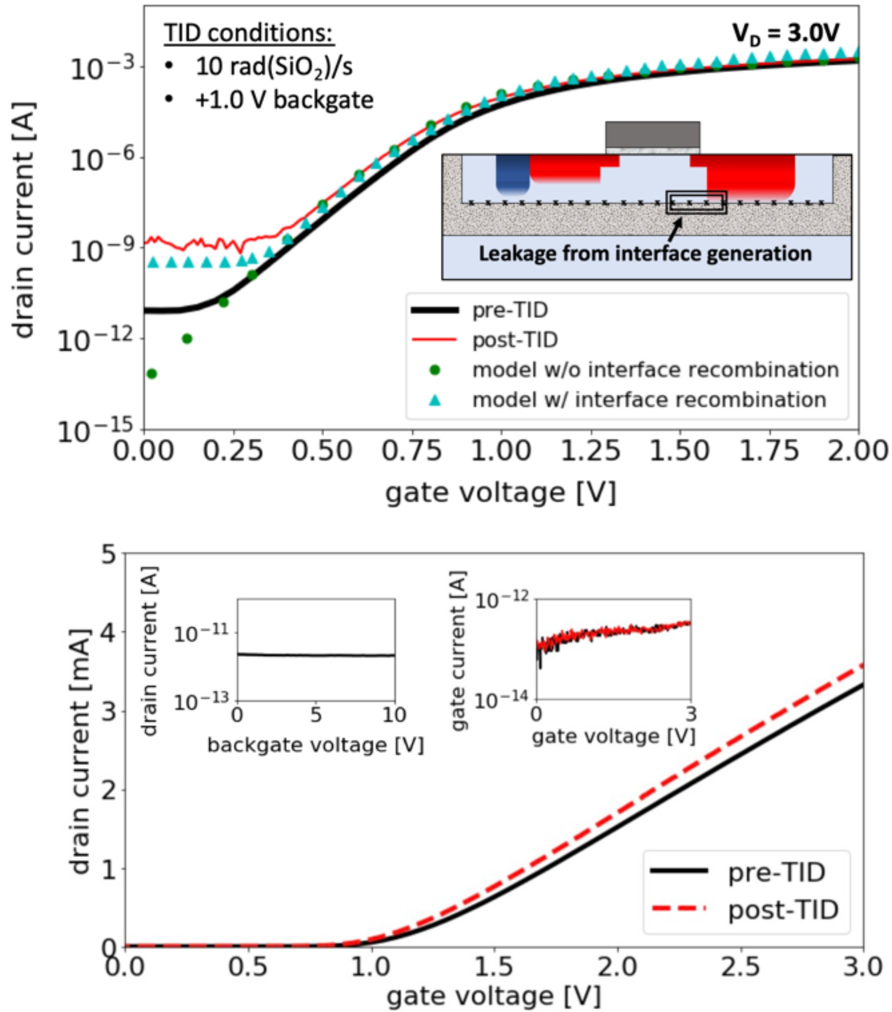

Fig. 63. Top: Transfer characteristics pre- and post gamma-irradiation (TID). Top: Increased OFF-state leakage current occurs following TID and corresponds to interface generation from isolation interfaces observed in modeling results. Bottom: Linear I(V) and gate current do not exhibit prominent TID effects or back-channel conduction.

noticeable back-channel conduction (I_D < 10 pA). Also, the linear I(V) does not display prominent TID effects (e.g., threshold voltage shift) nor is gate leakage measured after the irradiation. Therefore, we conclude the gamma-irradiation increases the quantity of interface defects and the SRV along the buried oxide interface.

V.2 Impact of surface recombination on charge collection measurements

Microbeam analysis is repeated following gamma-irradiation. In Fig. 64 the IBICC drain charge collection map before and after irradiation is compared. Before and after irradiation ion strikes in the channel collect the most charge (0.03-0.05 pC before irradiation and 0.01-0.03 pC following irradiation). Charge collection at the end regions and wrapping around the highly doped drain decreases dramatically following irradiation.

TRIBICC charge collection measurements are presented in Fig. 65 before and after irradiation for transients recorded across the actively measured device. Prior to irradiation 0.03 pC, 30 fC, is collected by the drain on average, while after irradiation the mean charge collection value

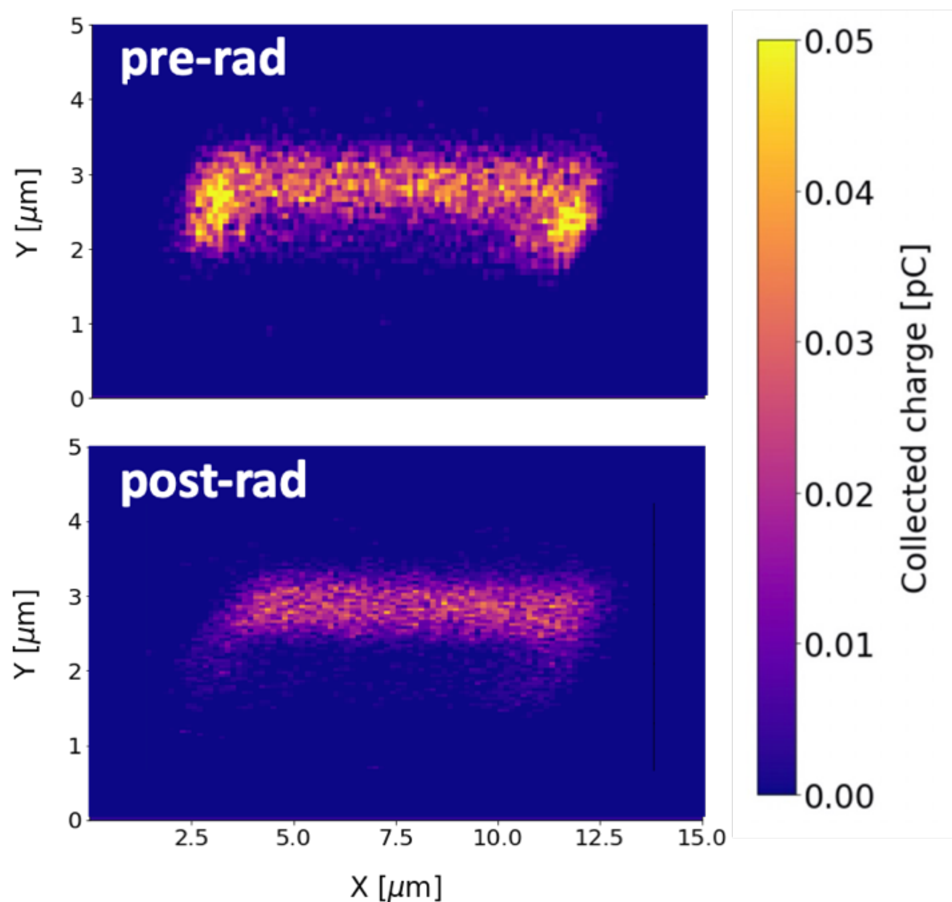

Fig. 64. Spatial charge collection distributions for IBICC measurements with the drain biased to +3.0V before and after gamma-irradiation.

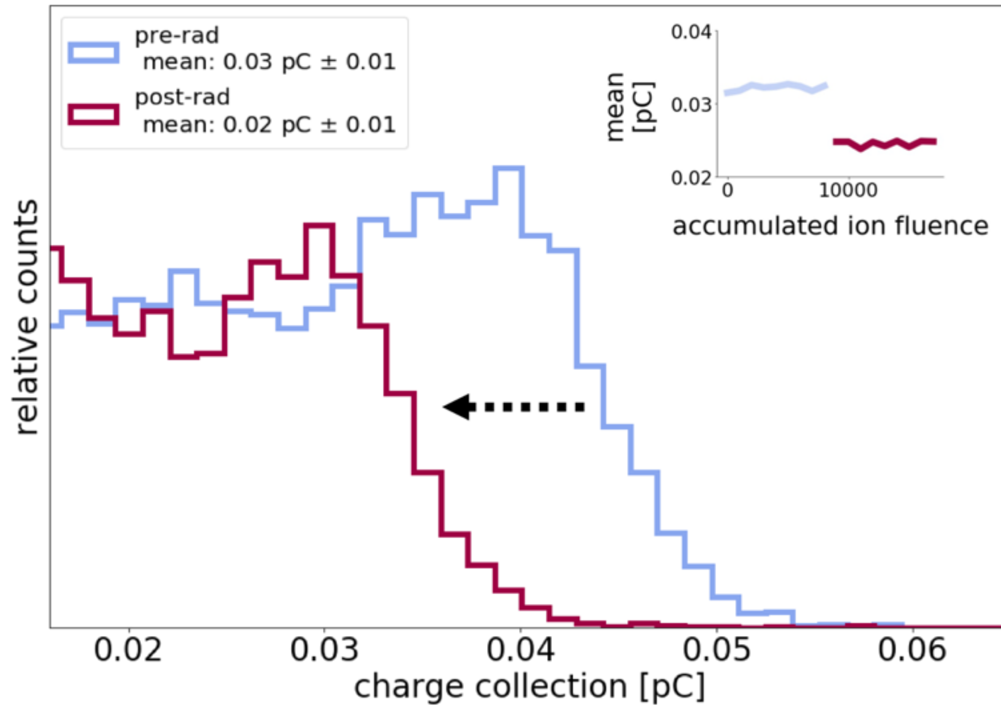

Fig. 65. TRIBICC charge collection distribution for PDSOI device pre- and post-rad. (Inset) The mean of the charge collection distribution exhibits an abrupt drop after TID but is stable with accumulated ion fluence.

drops to 20 fC. The distribution is multimodal with features corresponding to three primary factors: ion strike location, measurement noise, and variability in the ion-generated charge (i.e., straggle as discussed in Section II.2). The Gaussian-like peaks correspond to charge collection in the channel.

Plotted in the inset of Fig. 65 is the mean value during the accumulation of 10000 transients. The mean value remains constant during each microbeam test but shows an abrupt drop after gamma-irradiation. Microbeam testing can create displacement damage that reduces the carrier lifetime and can reduce charge collection; therefore, it is important to ensure charge collection is invariant during the microbeam measurements. If charge collection were to decrease during the accumulation ion fluence during microbeam analysis, the reduction in charge collection might be attributable to bulk recombination.

In Fig. 66 the mean collected charge as function of time for strike locations in the channel is shown. Channel strikes are defined as collecting 5 fC or greater based on the simulated charge collection and the IBICC charge collection measurements. Consistent with surface recombination modeling results, the difference between pre- and post-irradiation profiles increases after the initial prompt rise. The observed decrease in charge collection observed during IBICC and TRIBICC measurements, as well as the measured generation current, is consistent with an SRV along the isolation interfaces greater than 10^5 cm/s. Furthermore, transient simulations with fixed trapped charge introduced in the isolation oxides led to an *increase* in charge collection, making these experimental observations inconsistent with an increase in trapped charge from the gamma-irradiation. These results are the first reported evidence that surface recombination can impact the single-event response of an integrated circuit device.

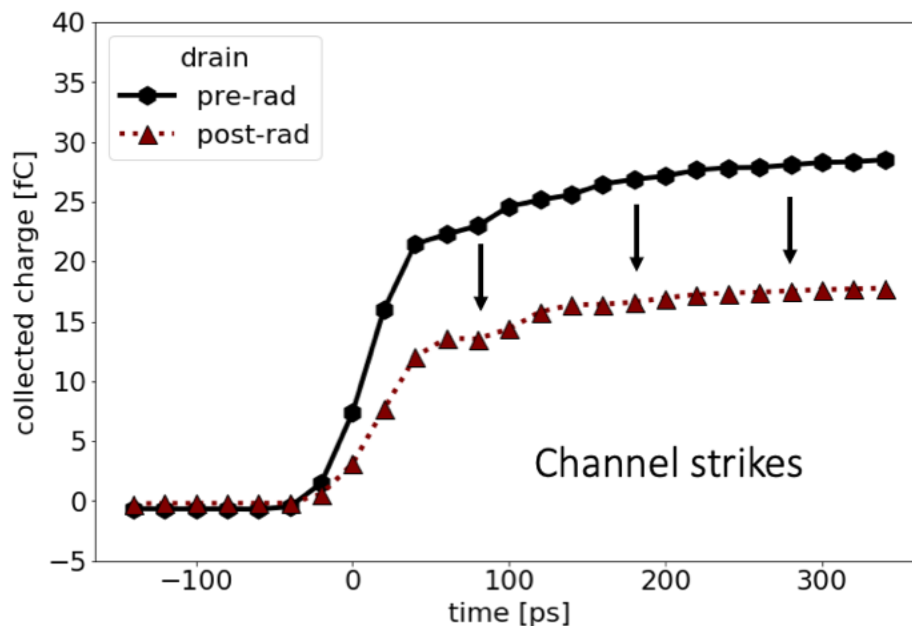

Fig. 66. The mean charge collection vs. time before and after irradiation.

CHAPTER VI

THE SURFACE RECOMBINATION EFFECT

The modeling and experimental results presented in the previous two chapters provide evidence that surface recombination can impact single event effects by reducing the amount of charge collected. Correlating the reduction in charge collection after gamma-irradiation during the experiments with the simulated results for charge collection as a function of SRV provides an estimate of degraded interface quality. In Fig. 67 measured charge collection before and after irradiation is compared to surface recombination simulations. The shaded region represented 1$\boldsymbol{\sigma}$**.** The simulated strike location is chosen with the same charge collection as the pre-rad experimental average. The amount of charge collected post-rad is in between simulation results for a surface recombination velocity of 10^5 cm/s and 10^6 cm/s; therefore, we can estimate that the SRV after irradiation is between 10^5 and 10^6 cm/s. A more specific estimate cannot be made using the microbeam technique because the ion strike location is not known as precisely as in simulation.

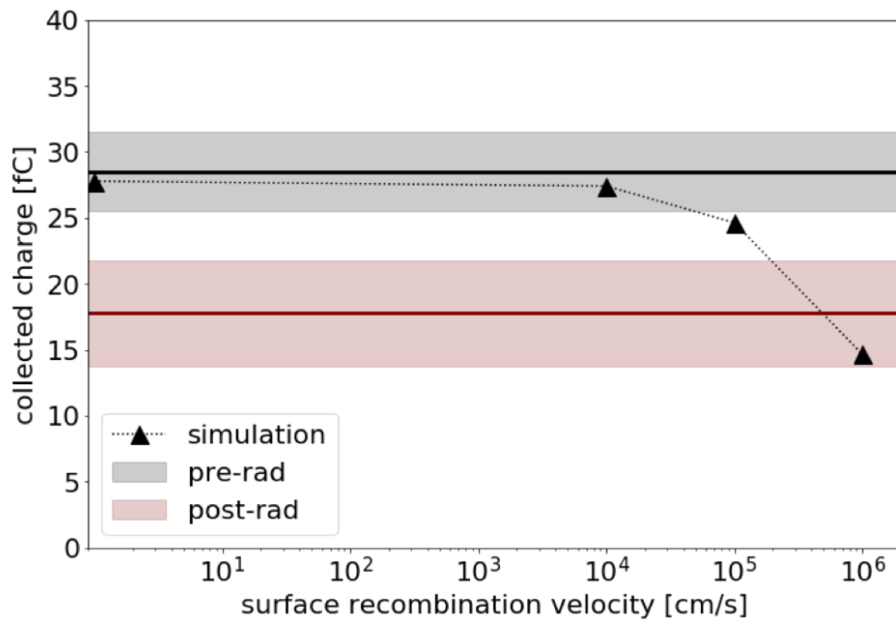

Fig. 67. Measured vs. simulated charge collection as a function of surface recombination.

In Fig. 68 the IBICC experimental results are compared to the model with an SRV = 10^6 cm/s. The quantity of charge collected for pre-rad and no surface recombination strongly

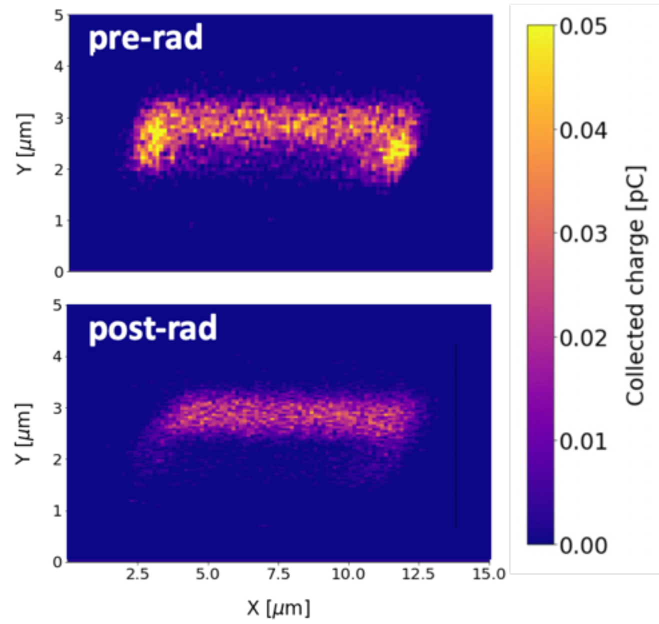

(a)

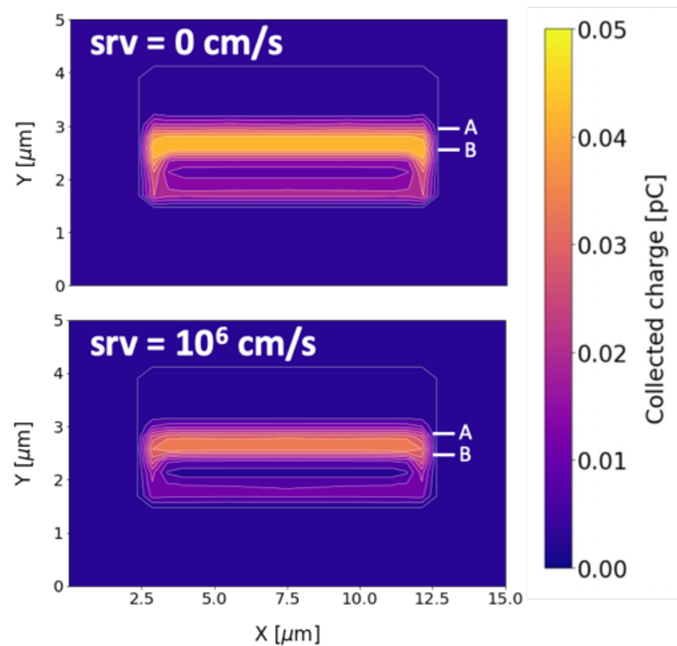

(b)

Fig. 68. Spatial charge collection distributions for a.) IBICC measurements before and after gamma-irradiation b.) finite-element simulations with low surface recombination, corresponding to pre-rad, and high surface recombination (10^6 cm/s) corresponding to post-rad interface conditions.

agrees; as does the post-rad and 10^6 cm/s results. This SRV exceeds published values for the Si/SiO_2 interface and demonstrates that irradiated isolation oxides can have lower quality interfaces with very high surface recombination velocities compared to other semiconductor surfaces.

Fig. 69 compares the SRV along different silicon interfaces and surfaces, including the results of this dissertation for degraded isolation. Low recombination velocities were obtained by Imangholi [83] for thermally-grown and chemically-etched Si/SiO_2 gate oxide interfaces as discussed in Section II.5. FGA and VA indicate a measurement after Forming Gas Anneal and Vacuum Anneal, respectively. These annealing steps improve the interface quality and reduce the SRV. Baek [84] and Nakamura [86] measurements are provided for bare silicon wafers and a buried oxide interface. Our results indicate that the SRV of TID-degraded isolation oxides can be 2 to 20 times greater, in the 10^5 – 10^6 cm/s range, and can significantly impact single-event charge collection.

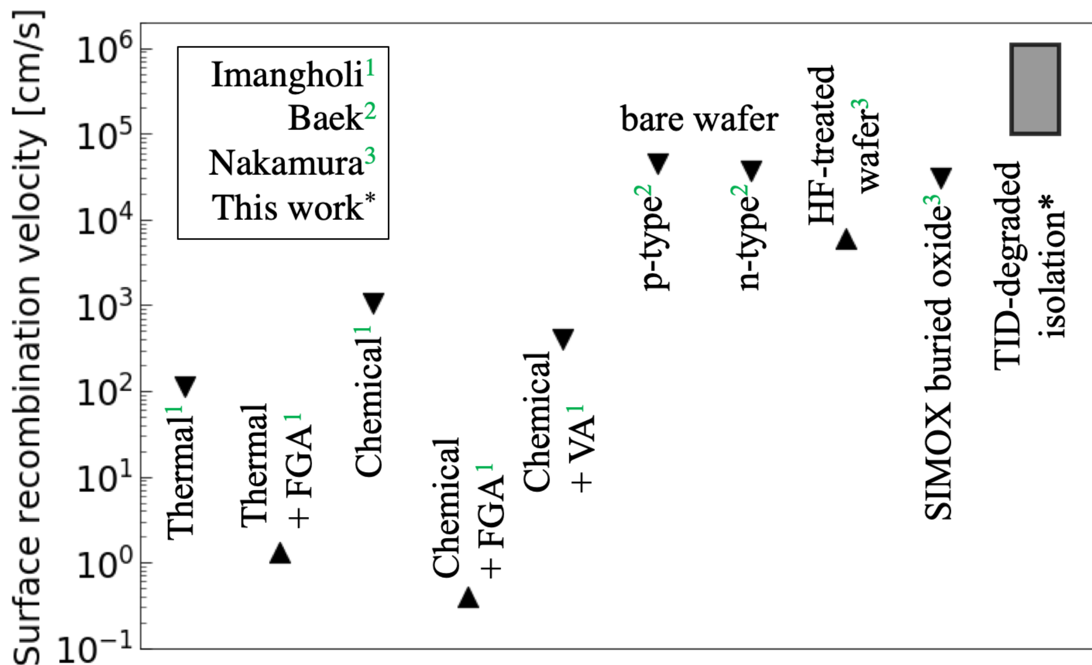

Fig. 69. Surface recombination velocities measured for Si/SiO_2 interfaces and bare silicon surfaces.

VI.1 Technology trends

One of the key manifestations of single event effects is a voltage transient at the output of an inverter. To illustrate the practical impact surface recombination can have when designing electronics for SEE hardness, voltage transient simulations were performed on 3D FEM models of CMOS inverters with a range of SRV. As discussed in Section II.3, voltage transients can result in soft errors and logic faults that reduce the reliability of electronic systems. In Fig. 70 and 71 the impact of surface recombination on a 90 nm and 45 nm PDSOI technologies is analyzed using the

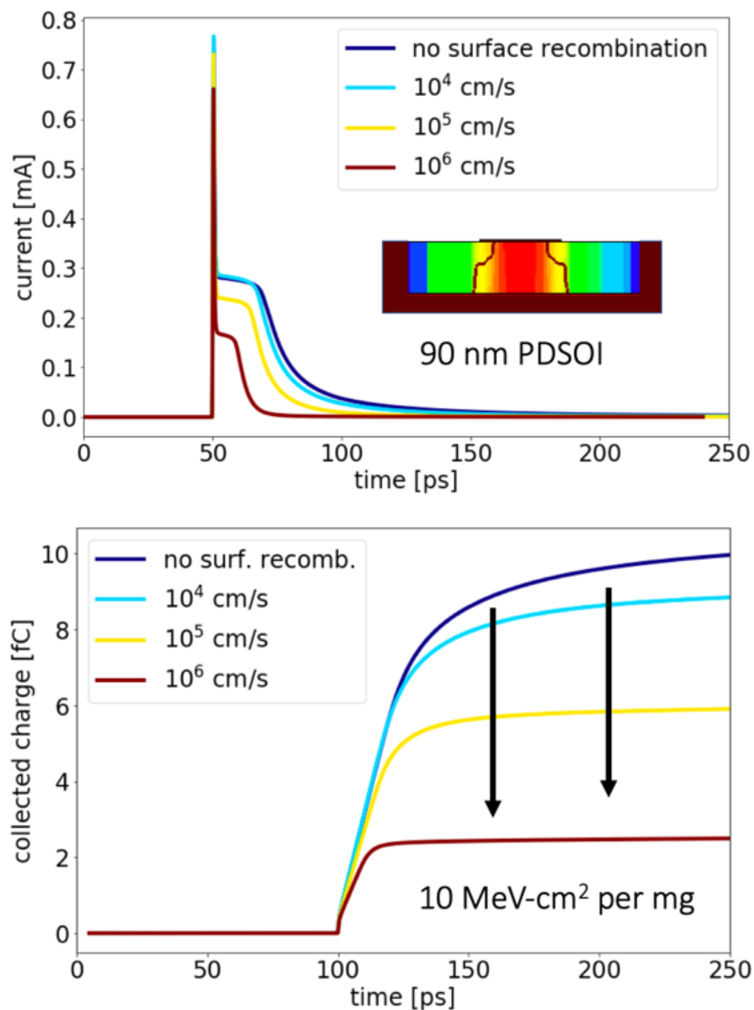

Fig. 70. The impact of surface recombination on drain transients and charge collection for a 10 MeV-cm^2 per mg channel strike in a 90 nm PDSOI device.

simulation techniques established in this dissertation. The 90 nm model was developed during a theoretical technology assessment while the 45nm models are based on IBM's 0.9V PDSOI technology and have been validated with on-chip measurements in previous ISDE studies [111]–[113]. An ion strike with an LET of 10 MeV-cm^2 per mg is simulated in the center channel of the off-state nmosfet. The excess charge distribution fills the device channel in each device. A plateau is observed during charge collection as the complementary pmos device provides limited restoring current during which time the erroneous output state is held.

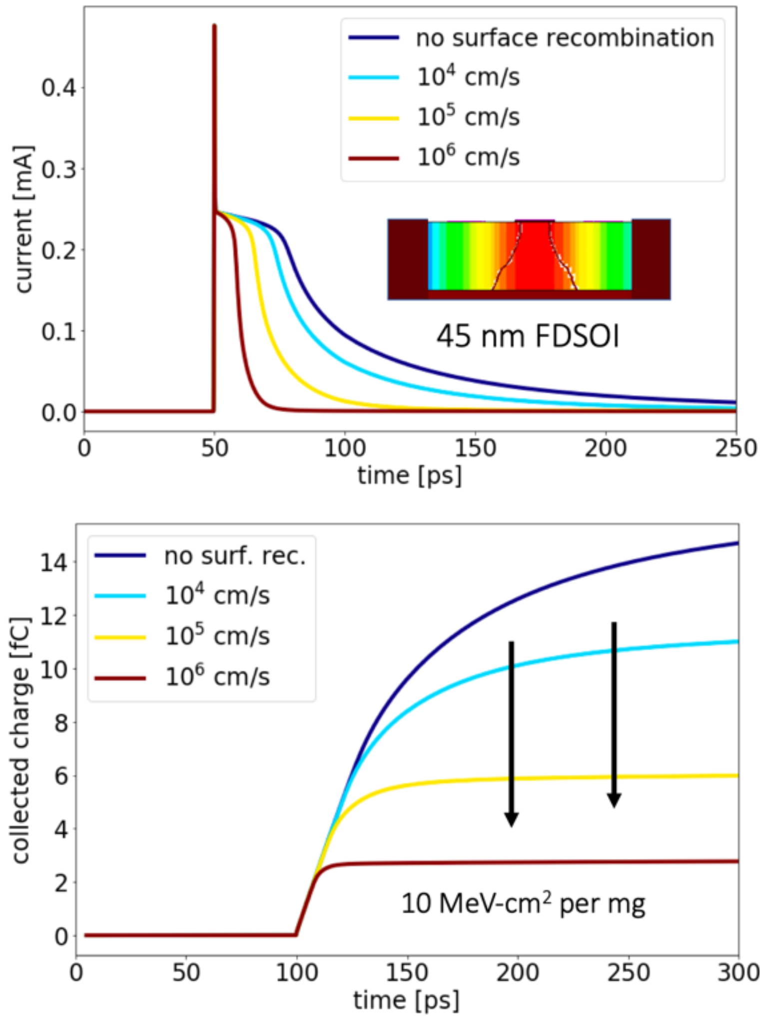

Fig. 71. The impact of surface recombination on drain transients and charge collection for a 10 MeV-cm^2 per mg channel strike in a 45 nm PDSOI device.

Two competing trends make the role of surface recombination with technology scaling dynamic:

- the ratio of isolation surface area to active silicon volume tends to increase with scaling and
- the duration of transients tends to decrease.

Therefore, with increasingly scaled technologies surface recombination is likely to occur on a greater percentage of the isolation surface area during a single-event but for a shorter period of time. In these two device models, increasing SRV decreases the amount of charge collected during the transient. Both scaled technologies experience a greater decrease in charge collection at 10^4 cm/s than the Sandia SOI technology. Further work is needed to experimentally examine the sensitivity of charge collection to surface recombination in scaled devices.

The pulse width of inverter transients in each technology scale is presented in Fig. 72 as a function of SRV. The operating voltage of each technology is different (350 nm: 3.3 V, 90 nm: 1.2 V, 45 nm: 0.9 V). The 350 nm Sandia technology has the longest duration voltage transients while the 90 nm and 45 nm devices have similar pulse widths. The pulse width of the 45 nm devices is more significantly reduced by surface recombination than that of the 90 nm devices. Excess carriers interact with a larger surface area in the 45 nm device for a similar transient duration as the 90 nm device. The limited duration of transients in small feature size devices may limit the amount of charge that can be lost to recombination; however, devices with very constrained active volumes (such as those in the thin films of FDSOI, FinFETs or gate-all-around devices) will exhibit substantial interface effects.

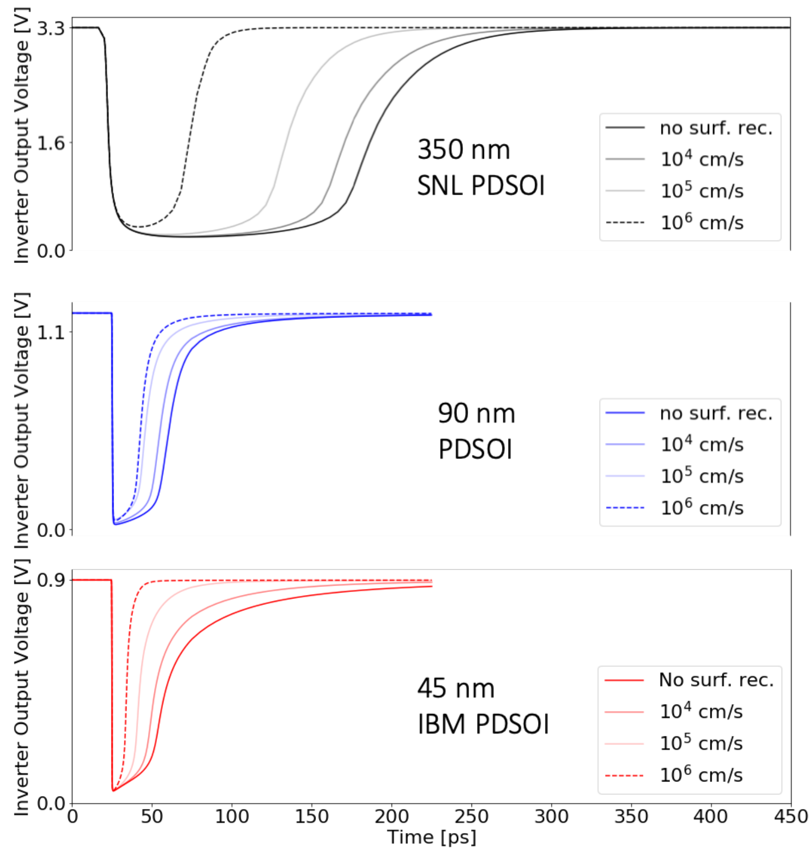

Fig. 72. The impact of surface recombination on inverter output voltage transients with technology scaling.

These results demonstrate that single-event charge collection in SOI devices with high quality oxides (SRV < 10^3 cm/s) is unlikely to be affected by surface recombination under normal operating conditions (e.g., a grounded substrate). Circumstances where interface effects are of concern and must be included in physics-based modeling include:

- Devices that are exposed to ionizing radiation with atypical bias conditions (such as those used in back-gating FDSOI technologies [114]),
- emerging systems/fabrication techniques with variable quality interfaces [115], and
- ultimately scaled technologies [116] with high surface area to volume ratios and/or complicated charge collection paths.

CHAPTER VII

CONCLUSIONS

Physics-based modeling is crucial for the continued success of high-reliability electronics. Developing accurate models of single event phenomena requires accurately capturing physical mechanisms. This dissertation demonstrates that surface recombination is an important physical mechanism to consider when evaluating the radiation-reliability of integrated devices if the isolation interfaces have an SRV of 10^3 cm/s or higher. If the SRV along isolation interfaces exceeds 10^5 cm/s, including surface recombination is essential to making quantitative predictions.

Low-dose rate irradiation with gamma-rays is capable of degrading thick buried oxide interfaces to surface recombination velocities that exceed 10^5 cm/s. Surface recombination at this level will reduce the amount of charge collected during a single-event and shorten single event transients, leading to over-predictions by models that do not include surface recombination. Modeling results indicate that surface recombination will continue to be an active mechanism at these interface conditions in modern highly-scaled device structures. The interplay between transient duration and the exposed surface area make the role of surface recombination with technology scaling dynamic and requires 3D modeling. Advancements in high-speed measurement, microbeam analysis, and carrier transport modeling should be applied as they become available to extend our understanding of surface recombination effects during fast transients.

REFERENCES

[1] R. D. Schrimpf *et al.*, “Multi-scale simulation of radiation effects in electronic devices,” *IEEE Trans. Nucl. Sci.*, vol. 55, no. 4, pp. 1891–1902, Aug. 2008.

[2] V. F. Hess, “Evidence for a stellar origin of the cosmic ultra-penetrating radiation,” *Nature*, no. 1, pp. 10–11, 1931.

[3] T. K. Gaisser, T. Stanev, and S. Tilav, “Cosmic ray energy spectrum from measurements of air showers,” *Front. Phys.*, vol. 8, no. 6, pp. 748–758, 2013.

[4] A. C. Cummings *et al.*, “Galactic cosmic rays in the local interstellar medium: Voyager 1 observations and model results,” *Astrophys. J.*, vol. 831, no. 1, p. 18, 2016.

[5] S. E. Forbush, “Three unusual cosmic-ray increases possibly due to charged particles from the Sun,” *Phys. Rev.*, vol. 70, no. 9–10, pp. 771–772, Nov. 1946.

[6] D. V. Reames, “The two sources of solar energetic particles,” *Space Sci. Rev.*, vol. 175, no. 1–4, pp. 53–92, 2013.

[7] D. J. McComas *et al.*, “Probing the energetic particle environment near the Sun,” *Nature*, vol. 576, no. 7786, pp. 223–227, Dec. 2019.

[8] J. L. Barth, C. S. Dyer, and E. G. Stassinopoulos, “Space, atmospheric, and terrestrial radiation environments,” *IEEE Trans. Nucl. Sci.*, vol. 50 III, no. 3, pp. 466–482, 2003.

[9] J. H. Adams, “The natural radiation environment inside spacecraft,” *IEEE Trans. Nucl. Sci.*, vol. 29, no. 6, pp. 2095–2100, 1982.

[10] L. Adams, “Cosmic ray effects in microelectronics,” *Microelectronics J.*, vol. 16, no. 2, pp. 17–29, 1985.

[11] J. H. Adams *et al.*, “CRÈME: The 2011 revision of the cosmic ray effects on micro-electronics code,” *IEEE Trans. Nucl. Sci.*, vol. 59, no. 6, pp. 3141–3147, 2012.

[12] E. Regener and G. Pfotzer, “Vertical intensity of cosmic rays by threefold coincidences in the stratosphere,” *Nature*, vol. 136, no. 3444, pp. 718–719, Nov. 1935.

[13] K. G. McCracken, H. Moraal, and P. H. Stoker, “Investigation of the multiple-component structure of the 20 January 2005 cosmic ray ground level enhancement,” *J. Geophys. Res. Sp. Phys.*, vol. 113, no. 12, pp. 1–18, 2008.

[14] H. Garrett, I. Jun, R. Evans, W. Kim, and D. Brinza, “The latest Jovian-trapped proton and heavy ion models,” *IEEE Trans. Nucl. Sci.*, vol. 64, no. 11, pp. 2802–2813, 2017.

[15] Xapsos, O’Neill, and T. P. O’Brien, “Near-Earth space radiation models,” *IEEE Trans. Nucl. Sci.*, vol. 60, no. 3, pp. 1691–1705, 2013.

[16] R. Baumann, T. Hossain, S. Murata, and I. Kitagawa, “Boron compounds as a dominant source of alpha particles in semiconductor devices,” *Reliab. Phys. Symp. 1995. 33rd Annu. Proceedings., IEEE Int.*, no. September, pp. 297–302, 1995.

[17] E. P. Wigner, “Theoretical physics in the metallurgical laboratory of Chicago,” *J. Appl. Phys.*, vol. 17, no. 11, pp. 857–863, 1946.

[18] G. C. Messenger and J. P. Spratt, “The effects of neutron irradiation on germanium and silicon,” *Proc. IRE*, vol. 99, pp. 1038–1044, 1956.

[19] S. R. Hofstein and F. P. Heiman, “The silicon insulated-gate field-effect transistor,” *Proc. IEEE*, vol. 51, no. 9, pp. 1190–1202, 1963.

[20] J. Raymond, E. Steele, and W. Chang, “Radiation effects in metal-oxide-semiconductor transistors,” *IEEE Trans. Nucl. Sci.*, vol. 12, no. 1, pp. 457–463, 1965.

[21] E. H. Snow, A. S. Grove, and D. J. Fitzgerald, “Effects of ionizing radiation on oxidized silicon surfaces and planar devices,” *Proc. IEEE*, vol. 14, no. June 1965, 1967.

[22] J. T. Wallmark and S. M. Marcus, “Maximum packing density and minimum size of

semiconductor devices," *IRE Trans. Electron Devices*, vol. 9, no. 1, pp. 111–112, 1962.

[23] D. Binder, E. C. Smith, and A. B. Holman, "Satellite anomalies from galactic cosmic rays," *IEEE Trans. Nucl. Sci.*, vol. 22, no. 6, pp. 2675–2680, 1975.

[24] T. C. May and M. H. Woods, "A new physical mechanism for soft errors in dynamic memories," in *16th International Reliability Physics Symposium*, 1978, pp. 33–40.

[25] R. A. Reed *et al.*, "Single-event effects ground testing and on-orbit rate prediction methods: The past, present, and future," *IEEE Trans. Nucl. Sci.*, vol. 50 III, no. 3, pp. 622–634, 2003.

[26] R. A. Weller *et al.*, "General framework for single event effects rate prediction in microelectronics," *IEEE Trans. Nucl. Sci.*, vol. 56, no. 6, pp. 3098–3108, 2009.

[27] R. A. Weller *et al.*, "Monte Carlo simulation of single event effects," *IEEE Trans. Nucl. Sci.*, vol. 57, no. 4, pp. 1726–1746, 2010.

[28] R. C. Baumann, "Radiation Induced Soft Errors in Advanced Semiconductor Technologies," *IEEE Trans. Device Mater. Reliab.*, vol. 5, no. 3, pp. 305–316, 2005.

[29] C. M. Hsieh, P. C. Murley, and R. R. O'Brien, "Dynamics of charge collection from alpha-particle tracks in integrated circuits," *19th Int. Reliab. Phys. Symp.*, pp. 38–42, 1981.

[30] K. M. Warren *et al.*, "Monte-Carlo based on-orbit single event upset rate prediction for a radiation hardened by design latch," *IEEE Trans. Nucl. Sci.*, vol. 54, no. 6, pp. 2419–2425, 2007.

[31] B. D. Sierawski *et al.*, "Impact of low-energy proton induced upsets on test methods and rate predictions," *IEEE Trans. Nucl. Sci.*, vol. 56, no. 6, pp. 3085–3092, 2009.

[32] J. S. Kauppila *et al.*, "Circuit-level layout-aware single-event sensitive-area analysis of 40-nm bulk CMOS flip-flops using compact modeling," *IEEE Trans. Nucl. Sci.*, vol. 58, no. 6 PART 1, pp. 2680–2686, 2011.

[33] K. M. Warren *et al.*, "Integrating circuit level simulation and Monte-Carlo radiation transport code for single event upset analysis in SEU hardened circuitry," *IEEE Trans. Nucl. Sci.*, vol. 55, no. 6, pp. 2886–2894, 2008.

[34] D. A. Black, W. H. Robinson, I. Z. Wilcox, D. B. Limbrick, and J. D. Black, "Modeling of single event transients with dual double-exponential current sources: implications for logic cell characterization," *IEEE Trans. Nucl. Sci.*, vol. 62, no. 4, pp. 1540–1549, 2015.

[35] J. S. Kauppila *et al.*, "A bias-dependent single-event compact model implemented into BSIM4 and a 90 nm CMOS process design kit," *IEEE Trans. Nucl. Sci.*, vol. 56, no. 6, pp. 3152–3157, 2009.

[36] S. DasGupta *et al.*, "Effect of well and substrate potential modulation on single event pulse shape in deep submicron CMOS," *IEEE Trans. Nucl. Sci.*, vol. 54, no. 6, pp. 2407–2412, 2007.

[37] L. W. Massengill, B. L. Bhuva, W. T. Holman, M. L. Alles, and T. D. Loveless, "Technology scaling and soft error reliability," *IEEE Int. Reliab. Phys. Symp. Proc.*, 2012.

[38] B. D. Sierawski *et al.*, "Effects of scaling on muon-induced soft errors," *IEEE Int. Reliab. Phys. Symp. Proc.*, pp. 247–252, 2011.

[39] M. P. King *et al.*, "Electron-induced single-event upsets in static random access memory," *IEEE Trans. Nucl. Sci.*, vol. 60, no. 6, pp. 4122–4129, 2013.

[40] M. P. King *et al.*, "The impact of delta-rays on single-event upsets in highly scaled SOI SRAMs," *IEEE Trans. Nucl. Sci.*, vol. 57, no. 6 PART 1, pp. 3169–3175, 2010.

[41] J. M. Trippe *et al.*, "Predicting the vulnerability of memories to muon-induced SEUs with low-energy proton tests informed by Monte Carlo simulations," *IEEE Int. Reliab. Phys. Symp. Proc.*, vol. 2016-Septe, pp. SE61–SE66, 2016.

[42] J. M. Trippe *et al.*, "Predicting muon-induced SEU rates for a 28-nm SRAM using protons and heavy ions to calibrate the sensitive volume model," *IEEE Trans. Nucl. Sci.*, vol. 65, no. 2, pp. 712–718, 2018.

[43] S. P. Buchner, F. Miller, V. Pouget, and D. P. McMorrow, "Pulsed-Laser Testing for Single Event Effects Investigations," *IEEE Trans. Nucl. Sci.*, vol. 60, no. 3, pp. 1852–1875, 2013.

[44] L. D. Ryder *et al.*, "Polarization Dependence of Pulsed Laser-Induced SEEs in SOI FinFETs," *IEEE Trans. Nucl. Sci.*, vol. 67, no. 1, pp. 38–43, 2020.

[45] A. Ildefonso *et al.*, "Optimizing optical parameters to facilitate correlation of laser-and heavy-ion-induced single-event transients in SiGe HBTs," *IEEE Trans. Nucl. Sci.*, vol. 66, no. 1, pp. 359–367, 2019.

[46] R. A. Reed *et al.*, "Physical processes and applications of the Monte Carlo Radiative Energy Deposition (MRED) code," *IEEE Trans. Nucl. Sci.*, vol. 62, no. 4, pp. 1441–1461, 2015.

[47] S. Agostinelli *et al.*, "Geant4 -- a simulation toolkit," *Nucl. Instruments Methods Phys. Res. Sect. A Accel. Spectrometers, Detect. Assoc. Equip.*, vol. 506, no. 3, pp. 250–303, 2003.

[48] R. A. Reed, R. A. Weller, R. D. Schrimpf, M. H. Mendenhall, K. M. Warren, and L. W. Massengill, "Implications of nuclear reactions for single event effects test methods and analysis," *IEEE Trans. Nucl. Sci.*, vol. 53, no. 6, pp. 3356–3362, 2006.

[49] D. R. Ball *et al.*, "Simulating nuclear events in a TCAD model of a high-density SEU hardened SRAM technology," *IEEE Trans. Nucl. Sci.*, vol. 53, no. 4, pp. 1794–1798, 2006.

[50] H. Bethe, "Zur Theorie des Durchgangs schneller Korpuskularstrahlen durch Materie," *Ann. Phys.*, vol. 397, no. 3, pp. 325–400, 1930.

[51] F. Bloch, "Zur Bremsung rasch bewegter Teilchen beim Durchgang durch Materie," *Ann. Phys.*, vol. 408, no. 3, pp. 285–320, 1933.

[52] C. Amsler *et al.*, “Review of particle physics,” *Phys. Lett. B*, vol. 667, no. 1–5, pp. 1–6, Sep. 2008.

[53] M. P. King *et al.*, “Radial characteristics of heavy-ion track structure and implications of delta-ray events for microelectronics,” *Appl. Phys. Lett.*, vol. 101, no. 5, pp. 1–4, 2012.

[54] M. V. Fischetti and S. E. Laux, “Band structure, deformation potentials, and carrier mobility in strained Si Ge, and SiGe alloys,” *J. Appl. Phys.*, vol. 80, no. 4, pp. 2234–2252, 1996.

[55] M. V. Fischetti, N. Sano, S. E. Laux, and K. Natori, “Full-band-structure theory of high-field transport and impact ionization of electrons and holes in Ge, Si, and GaAs,” *J. Technol. Comput. Aided Des. TCAD*, pp. 1–50, 1996.

[56] J. Fang *et al.*, “Understanding the average electron-hole pair-creation energy in silicon and germanium based on full-band Monte Carlo simulations,” *IEEE Trans. Nucl. Sci.*, vol. 66, no. 1, pp. 444–451, 2019.

[57] W. Shockley, “Problems related to p-n junctions in silicon,” *Solid. State. Electron.*, vol. 2, no. 1, pp. 35–67, Jan. 1961.

[58] D. M. Fleetwood, “Evolution of total ionizing dose effects in MOS devices with Moore’s Law scaling,” *IEEE Trans. Nucl. Sci.*, pp. 1–17, 2017.

[59] H. J. Barnaby, “Total-ionizing-dose effects in modern CMOS technologies,” *IEEE Trans. Nucl. Sci.*, vol. 53, no. 6, pp. 3103–3121, 2006.

[60] J. R. Schwank *et al.*, “Radiation effects in MOS oxides,” *IEEE Trans. Nucl. Sci.*, vol. 55, no. 4, pp. 1833–1853, 2008.

[61] D. M. Fleetwood, “Evolution of total ionizing dose effects in MOS devices with moore’s law scaling,” *IEEE Trans. Nucl. Sci.*, vol. 65, no. 8, pp. 1465–1481, 2018.

[62] X. Shen, Y. S. Puzyrev, D. M. Fleetwood, R. D. Schrimpf, and S. T. Pantelides, “Quantum

mechanical modeling of radiation-induced defect dynamics in electronic devices," *IEEE Trans. Nucl. Sci.*, vol. 62, no. 5, pp. 2169–2180, 2015.

[63] E. Cartier, J. H. Stathis, and D. A. Buchanan, "Passivation and depassivation of silicon dangling bonds at the Si/SiO2 interface by atomic hydrogen," *Appl. Phys. Lett.*, vol. 63, no. 11, pp. 1510–1512, 1993.

[64] E. H. Poindexter, P. J. Caplan, B. E. Deal, and R. R. Razouk, "Interface states and electron spin resonance centers in thermally oxidized (111) and (100) silicon wafers," *J. Appl. Phys.*, vol. 52, no. 2, pp. 879–884, 1981.

[65] F. B. McLean and T. R. Oldham, "Basic mechanisms of radiation effects in electronic materials and devices," *Harry Diam. Labs Tech. Rep.*, vol. HDL-TR, p. 2129, 1987.

[66] M. R. Shaneyfelt, D. M. Fleetwood, J. R. Schwank, and K. L. Hughes, "Charge yield for cobalt-60 and 10-keV x-ray irradiations of MOS devices," *IEEE Trans. Nucl. Sci.*, vol. 38, no. 6, pp. 1187–1194, 1991.

[67] D. M. Fleetwood, L. C. Riewe, J. R. Schwank, S. C. Witczak, and R. D. Schrimpf, "Radiation effects at low electric fields in thermal, SIMOX, and bipolar-base oxides," *IEEE Trans. Nucl. Sci.*, vol. 43, no. 6, pp. 2537–2546, 1996.

[68] S. N. Rashkeev *et al.*, "Physical model for enhanced interface-trap formation at low dose rates," *IEEE Trans. Nucl. Sci.*, vol. 49 I, no. 6, pp. 2650–2655, 2002.

[69] S. C. Witczak, "Space charge limited degradation of bipolar oxides at low electric fields," *IEEE Trans. Nucl. Sci.*, vol. 45, no. 6 PART 1, pp. 2339–2351, 1998.

[70] D. R. Hughart *et al.*, "The effects of proton-defect interactions on radiation-induced interface-trap formation and annealing," *IEEE Trans. Nucl. Sci.*, vol. 59, no. 6, pp. 3087–3092, 2012.

[71] N. S. Saks, C. M. Dozier, and D. B. Brown, "Time dependence of interface trap formation in mosfets following pulsed irradiation," *IEEE Trans. Nucl. Sci.*, vol. 35, no. 6, pp. 1168–1177, 1988.

[72] W. Shockley and W. T. Read, "Statistics of the recombinations of holes and electrons," *Phys. Rev.*, vol. 87, no. 5, pp. 835–842, 1952.

[73] A. M. Tonigan, C. N. Arutt, E. J. Parma, P. J. Griffin, D. M. Fleetwood, and R. D. Schrimpf, "Correlation of a bipolar-transistor-based neutron displacement damage sensor methodology with proton irradiations," *IEEE Trans. Nucl. Sci.*, vol. 65, no. 1, pp. 495–501, Jan. 2018.

[74] S. C. Witczak *et al.*, "Damage separation in a bipolar junction transistor following irradiation with 250-MeV protons," *IEEE Trans. Nucl. Sci.*, vol. 66, no. 5, pp. 795–800, May 2019.

[75] "Standard test method for use of 2N2222A silicon bipolar transistors as neutron spectrum sensors and displacement damage monitors," *ASTM Int.*, vol. 1855–20, pp. 1–10, 2020.

[76] D. M. Schmidt *et al.*, "Comparison of ionizing-radiation-induced gain degradation in lateral, substrate, and vertical PNP BJTs," *IEEE Trans. Nucl. Sci.*, vol. 42, no. 6, pp. 1541–1549, 1995.

[77] H. J. Barnaby, S. K. Smith, R. D. Schrimpf, D. M. Fleetwood, and R. L. Pease, "Analytical model for proton radiation effects in bipolar devices," *IEEE Trans. Nucl. Sci.*, vol. 49 I, no. 6, pp. 2643–2649, 2002.

[78] H. J. Barnaby, B. Vermeire, and M. J. Campola, "Improved model for increased surface recombination current in irradiated bipolar junction transistors," *IEEE Trans. Nucl. Sci.*, vol. 62, no. 4, pp. 1658–1664, 2015.

[79] R. S. Bonilla, B. Hoex, P. Hamer, and P. R. Wilshaw, “Dielectric surface passivation for silicon solar cells: A review,” *Phys. Status Solidi Appl. Mater. Sci.*, vol. 214, no. 7, 2017.

[80] Y. Da and Y. Xuan, “Role of surface recombination in affecting the efficiency of nanostructured thin-film solar cells,” *Opt. Express*, vol. 21, no. S6, p. A1065, 2013.

[81] J. P. Correa-Baena *et al.*, “Changes from bulk to surface recombination mechanisms between pristine and cycled perovskite solar cells,” *ACS Energy Lett.*, vol. 2, no. 3, pp. 681–688, 2017.

[82] D. J. Fitzgerald and A. S. Grove, “Surface recombination in semiconductors,” *Surf. Sci.*, vol. 9, no. July, pp. 347–369, 1968.

[83] B. Imangholi, F. L. Lie, H. G. Parks, and A. J. Muscat, “Effect of deep-level defects on surface recombination velocity at the interface between silicon and dielectric films,” *IEEE Trans. Electron Devices*, vol. 57, no. 4, pp. 877–889, 2010.

[84] D. Baek, S. Rouvimov, B. Kim, T. C. Jo, and D. K. Schroder, “Surface recombination velocity of silicon wafers by photoluminescence,” *Appl. Phys. Lett.*, vol. 86, no. 11, pp. 1–3, 2005.

[85] A. Cuevas, P. A. Basore, G. Giroult-Matlakowski, and C. Dubois, “Surface recombination velocity of highly doped n-type silicon,” *J. Appl. Phys.*, vol. 80, no. 6, pp. 3370–3375, 1996.

[86] S. Nakamura, D. Watanabe, A. En, M. Suhara, and T. Okumura, “Contactless electrical characterization of surface and interface of SOI materials,” *Appl. Surf. Sci.*, vol. 216, no. 1-4 SPEC., pp. 113–118, 2003.

[87] M. Bruel, B. Aspar, and A.-J. Auberton-Herve, “Smart-cut: A new silicon-on-insulator material technology based on hydrogen implantation and wafer bonding,” *Jpn. J. Appl. Phys.*, vol. 36, no. 3B, pp. 1636–1641, 1997.

[88] W. Schwarzenbach, B. Y. Nguyen, F. Allibert, C. Girard, and C. Maleville, “Ultra-thin body & buried oxide SOI substrate development and qualification for Fully Depleted SOI device with back bias capability,” *Solid. State. Electron.*, vol. 117, pp. 2–9, 2016.

[89] J. R. Schwank, V. Ferlet-Cavrois, M. R. Shaneyfelt, P. Paillet, and P. E. Dodd, “Radiation effects in SOI technologies,” *IEEE Trans. Nucl. Sci.*, vol. 50, no. 3, pp. 522–538, 2003.

[90] W. T. Chang, C. M. Lai, and W. K. Yeh, “Reliability of the doping concentration in an ultra-thin body and buried oxide silicon on insulator (SOI) and comparison with a partially depleted SOI,” *Microelectron. Reliab.*, vol. 54, no. 2, pp. 485–489, 2014.

[91] L. Palkuti, M. Alles, H. Hughes, D. Threat, R. Agency, and F. Belvior, “The role of radiation effects in SOI technology development,” *IEEE*, pp. 31–32, 2014.

[92] M. Turowski, A. Raman, and R. D. Schrimpf, “Nonuniform total-dose-induced charge distribution in shallow-trench isolation oxides,” in *IEEE Transactions on Nuclear Science*, 2004, vol. 51, no. 6 II, pp. 3166–3171.

[93] L. J. Mcdaid, S. Hall, W. Eccleston, and J. C. Alderman, “The origin of the anomalous off-current in SOI-transistors,” *Eur. Solid-State Device Res. Conf.*, pp. 759–762, 1989.

[94] L. J. McDaid, S. Hall, W. Eccleston, and J. C. Alderman, “On the application of capacitance-time and charge-time measurements to determine the generation lifetime and surface generation velocity in silicon-on-insulator (SOI) substrates,” *Semicond. Sci. Technol.*, vol. 7, no. 7, pp. 940–952, 1992.

[95] L. W. Massengill, D. V. Kerns, S. E. Kerns, and M. L. Alles, “Single-event charge enhancement in SOI devices,” *IEEE Electron Device Lett.*, vol. 11, no. 2, pp. 98–99, 1990.

[96] J. R. Schwank *et al.*, “Charge collection in SOI capacitors and circuits and its effect on SEU hardness,” *IEEE Trans. Nucl. Sci.*, vol. 49 I, no. 6, pp. 2937–2947, 2002.

[97] V. Ferlet-Cavrois *et al.*, “Charge collection by capacitive influence through isolation oxides,” *IEEE Trans. Nucl. Sci.*, vol. 50, no. 6 I, pp. 2208–2218, 2003.

[98] G. Vizkelethy *et al.*, “Anomalous charge collection from silicon-on-insulator structures,” *Nucl. Instruments Methods Phys. Res. Sect. B Beam Interact. with Mater. Atoms*, vol. 210, pp. 211–215, 2003.

[99] G. Vizkelethy, D. K. Brice, and B. L. Doyle, “Heavy ion beam induced current/charge (IBIC) through insulating oxides,” *Nucl. Inst. Methods Phys. Res. B*, vol. 249, pp. 204–208, 2006.

[100] J. R. Schwank, M. R. Shaneyfelt, B. L. Draper, and P. E. Dodd, “BUSFET-A radiation-hardened SOI transistor,” *IEEE Trans. Nucl. Sci.*, vol. 46, no. 6, pp. 1809–1816, 1999.

[101] J. D. Black *et al.*, “DFF Layout Variations in CMOS SOI—Analysis of Hardening by Design Options,” *IEEE Trans. Nucl. Sci.*, vol. 67, no. 6, pp. 1125–1132, Jun. 2020.

[102] P. E. Dodd and F. W. Sexton, “Critical charge concepts for CMOS SRAMs,” *IEEE Trans. Nucl. Sci.*, vol. 42, no. 6 pt 1, pp. 1764–1771, 1995.

[103] C. Detcheverry *et al.*, “SEU critical charge and sensitive area in a submicron CMOS technology,” *IEEE Trans. Nucl. Sci.*, vol. 44, no. 6, pp. 2266–2273, 1997.

[104] R. Naseer, Y. Boulghassoul, J. Draper, S. DasGupta, and A. Witulski, “Critical charge characterization for soft error rate modeling in 90nm SRAM,” in *2007 IEEE International Symposium on Circuits and Systems*, 2007, pp. 1879–1882.

[105] F. W. Sexton, “Microbeam studies of single-event effects,” *IEEE Trans. Nucl. Sci.*, vol. 43, no. 2, pp. 687–695, Apr. 1996.

[106] G. Vizkelethy, D. K. Brice, and B. L. Doyle, “The theory of ion beam induced charge in metal-oxide-semiconductor structures,” *J. Appl. Phys.*, vol. 101, no. 7, pp. 074506/1–

074506/6, 2007.

[107] P. Paillet *et al.*, “Comparison of charge yield in MOS devices for different radiation sources,” *IEEE Trans. Nucl. Sci.*, vol. 49 I, no. 6, pp. 2656–2661, 2002.

[108] H. L. Hughes and J. M. Benedetto, “Radiation effects and hardening of MOS technology: Devices and circuits,” *IEEE Trans. Nucl. Sci.*, vol. 50 III, no. 3, pp. 500–521, 2003.

[109] H. J. Barnaby, M. Mclain, and I. S. Esqueda, “Total-ionizing-dose effects on isolation oxides in modern CMOS technologies,” *Nucl. Instruments Methods Phys. Res. Sect. B Beam Interact. with Mater. Atoms*, vol. 261, no. 1-2 SPEC. ISS., pp. 1142–1145, 2007.

[110] D. M. Fleetwood, “Total ionizing dose effects in MOS and low-dose-rate-sensitive linear-bipolar devices,” *IEEE Trans. Nucl. Sci.*, vol. 60, no. 3, pp. 1706–1730, 2013.

[111] T. D. Loveless *et al.*, “On-chip measurement of single-event transients in a 45 nm silicon-on-insulator technology,” *IEEE Trans. Nucl. Sci.*, vol. 59, no. 6, pp. 2748–2755, 2012.

[112] J. A. Maharrey *et al.*, “Effect of device variants in 32 nm and 45 nm SOI on SET pulse distributions,” *IEEE Trans. Nucl. Sci.*, vol. 60, no. 6, pp. 4399–4404, 2013.

[113] J. S. Kauppila *et al.*, “Geometry-aware single-event enabled compact models for sub-50 nm partially depleted silicon-on-insulator technologies,” *IEEE Trans. Nucl. Sci.*, vol. 62, no. 4, pp. 1589–1598, 2015.

[114] R. Carter *et al.*, “22nm FDSOI technology for emerging mobile, Internet-of-Things, and RF applications,” *Tech. Dig. - Int. Electron Devices Meet. IEDM*, pp. 2.2.1-2.2.4, 2017.

[115] M. Lorenz *et al.*, “The 2016 oxide electronic materials and oxide interfaces roadmap,” *J. Phys. D. Appl. Phys.*, vol. 49, no. 43, 2016.

[116] P. Ye, T. Ernst, and M. V. Khare, “The nanosheet transistor is the next (and maybe last) step in Moore’s Law,” *IEEE Spectrum*, 2019.